INAUGURAL-DISSERTATION

zur Erlangung der Doktorwürde der

Naturwissenschaftlich-Mathematischen Gesamtfakultät der

Ruprecht-Karls-Universität Heidelberg

vorgelegt von

Wenwen Chen

aus Wenzhou, China

Tag der mündlichen Prüfung: 01. 03. 2016

Anti-Reflective and Anti-Bacterial Properties of Biomimetic Nanostructures

Gutachter

Prof. Dr. Joachim P. Spatz

Physikalisch-Chemisches Institut
Ruprecht-Karls-Universität Heidelberg
Max-Planck-Institut für Intelligente Systeme

Prof. Dr. Reiner Dahint

Physikalisch-Chemisches Institut
Ruprecht-Karls-Universität Heidelberg

for my parents

Table of contents

Abstract

In this thesis artificial nanostructured surfaces inspired by the moth eye were developed on both inorganic and organic substrates. Two properties, *i.e.* anti-reflective (AR) and anti-bacterial (AB) were studied in detail.

On inorganic fused silica (Suprasil®) substrates, nanopillar arrays were fabricated by combining block copolymer micellar lithography (BCML) and reactive ion etching (RIE) techniques. The nanopillar arrays were fabricated on a large area and the parameters of the pillars were controlled. The substrates were used as molds to create nanostructures in organic substrates using two methods: replica molding and nanoimprinting. The first method transferred the pillar structure into a polyurethane substrate creating nanoholes. However, it was shown that this method was limited due to the low aspect ratio and difficulties in mold removal. Using nanoimprinting methods instead solved these problems. Both nanohole and nanopillar structures were homogeneously imprinted in a large area of the intermediate polymer stamp (IPS®) and polymethylmethacrylate (PMMA) materials.

The AR properties of both organic and inorganic substrates were characterized using optical spectrometry. On Suprasil® surfaces, the transmittance was increased over a wide wavelength range of 200-1000 nm, with a maximum of 99.5% transmission per interface. Nanoimprinted IPS® and PMMA also depicted highly improved transmittance, with an increase from 91.5% to 95% with a single-sided nanohole array on IPS® and from 91.5% to 97.5% with a double-sided nanopillar array on PMMA. Excellent AR performance was achieved to a high incident angle of 60°, which significantly outperformed traditional thin-film AR coatings. A theoretical model was also set up matching the experimental results very well.

The AB properties of the moth eye inspired structures were investigated on the nanostructured Suprasil®. The surface coverage of *Staphylococcus sciuri* (*S. sciuri*) bacteria was statistically analyzed by optical microscopy and the attachment sites between the bacteria and the nanostructures were observed by scanning electron microscopy (SEM). Although the surface coverage showed no significant difference between the nanostructured and planar surfaces, SEM images clearly revealed a different interaction of the bacteria and the nanostructures compared to plain surfaces. Nano-fibers most likely fimbriae connecting the bacteria and the nanopillar tips were observed. Therefore, it was shown that the bacterium is able to sense the nano-scale features and respond with cell morphological alterations.

Zusammenfassung

In dieser Arbeit wurden nanostrukturierte Oberflächen auf anorganischen und organischen Substraten hergestellt. Als natürliches Vorbild diente das Mottenaugen, das auf der Oberfläche eine antireflexive Nanostruktur besitzt. Die künstlich hergestellten Nanostrukturen wurden hinsichtlich ihrer antireflexiven (AR) als auch antibakterielle (AB) Eigenschaften untersucht.

Auf anorganischem Quarzglas (Suprasil®) wurden „Nanopillar"-Strukturen durch die Kombination von Block-Copolymer Nanolithographie (BCML) und reaktivem Ionenätzen (RIE) hergestellt. Die „Nanopillar"-Strukturen konnten damit großflächig und mit steuerbaren Parametern auf dem Substrat realisiert werden. Die „Nanopillar"-Strukturen wurden als Negativform für anschließende Replikationsverfahren verwendet. Hierbei konnte die Nanostrukturierung eines organischen Substrates (Poylmere) durch die Anwendung zweier unterschiedlicher Replikationsmethoden, Abformung und Nanoimprint, realisiert werden. Durch Abformung gelang die Replikation eines „Nanohole"-Musters in Polyurethan. Allerdings gestaltete sich diese Methode aufgrund des geringen Seitenverhältnisses der Nanostrukturen und des Entformungsvorgangs als problematisch. Durch die Anwendung des Nanoimprint-Verfahrens konnten jedoch „Nanohole"- sowie „Nanopillar"-Strukturen homogen auf einem Zwischenpolymer Stempel (IPS®) und Polymethylmethacrylat (PMMA) Materialien erzeugt werden.

Die AR-Eigenschaften anorganischer als auch organischer Substrate wurden durch optische Spektrometrie charakterisiert. Bei den Suprasil® Oberflächen wurde die Transmission über einen großen Wellenlängenbereich von 200-1000 nm, mit einem Maximum von 99,5% pro Mediengrenze verbessert. "Nanoimprinted" IPS® und PMMA zeigen ebenfalls eine verbesserte Transmission mit einer Erhöhung auf 91,5% bis 95% bei einseitiger „Nanohole"- Strukturierung auf IPS® und auf 91,5% bis 97,5% bei doppelseitigen „Nanopillar"-Strukturierung auf PMMA. Darüberhinaus wurden ausgezeichnete AR-Eigenschaften unter einem hohen Einfallswinkel von 60° erreicht, was die Eigenschaften traditioneller AR-Beschichtung deutlich übertrifft. Zusätzlich wurde ein theoretisches Modell erstellt, das hervorragend mit den Versuchsergebnissen übereinstimmte.

Die AB-Eigenschaften von nanostrukturiertem Suprasil® wurden ebenfalls untersucht. Mittels Lichtmikrsokopie wurde der Bedeckungsgrad der an der Oberfläche haftenden *Staphylococcus sciuri* (*S. sciuri*) Bakterien statistisch analysiert. Die Interaktion der Bakterien mit der Nanostruktur wurde mittels Rasterelektronenmikroskopie (REM) untersucht. Obwohl keine signifikanten Unterschiede hinsichtlich des Bedeckungsgrads der *S. sciuri* auf nanostrukturierten und planaren Oberflächen festzustellen war, konnte eindeutig die Interaktion der Bakterien mit den Enden der "Nanopillars" durch die Ausbildung von Nanofasern vermutlich so genannten "nano-fimbriae" gezeigt werden. Diese Art von Strukturen konnte auf keiner der Kontrolloberflächen gefunden werden. Dies zeigt, dass die Bakterien fähig sind die Nanostruktur zu erkenne und darauf mit morphologischen Veränderungen zu reagieren.

Chapter 1   Introduction

1.1   Overview and motivation

Nanostructured materials have attracted huge interests since they were first proposed in 1960's by Dr. Feymann [1]. Recently, many natural surfaces on animals and plants are discovered exhibiting excellent physical and chemical properties. For example, *Morpho* butterfly wings show an iridescent blue coloration in a wide wavelength range, not because of any pigments present, but due to its multilayer of "Christmas tree" photonic structures on the wings [2-4]. The moth-eye nanostructures on night-active insects have superior anti-reflection (AR) properties in a wide incident angle due to the nanopillar arrays arranged on the surface of their compound eyes [5,6]. The lotus effect is also well known, as the leaf surface has superhydrophobic and self-cleaning properties due to its nano-protuberances [7,8].

Inspired by these nanostructures that have been discovered in nature, artificial nanostructured materials were designed and significantly developed in various applications. For example, Gombert *et al.* [9,10] designed the moth-eye AR structures on Si wafers to improve the light transmission efficiency for solar cells. Potyrailo and colleagues [11] studied the optical response on the lamellar structure of *Morpho* butterfly wing to different vapors for the design of a nano-engineered gas sensor. A biosensor was also developed based on the Fabry-Perot fringes occuring on the nanoscale of porous silicon [12]. One commercial example for nature inspired nanostructures is the "Moth Eye Panel" on liquid crystal displays (LCD) of television produced by the SHARP company [13], which lead to a high contrast image while suppressing the screen reflections to a minimum.

However, the fabrication of such nano-scale structures with high efficiency and high yield still poses extra challenges and it limits the applications of the nano-engineered surfaces. Traditional photolithography techniques [14] do not provide a high enough resolution to nano-scale structures. Electron-beam (e-beam) [15] and focused ion-beam (FIB) lithography [16] exhibit very high resolution, and are commonly used in scientific researches; however, the procedures are very slow and therefore not suitable for the fabrication of large area nanostructures. The nanoimprinting technique [17,18] is a promising method that replicates nanostructures from a mold to a substrate with nano-scale resolution and can be applied to large areas. However, the applied mold is usually fabricated by e-beam lithography, which is still time-consuming and expensive [19].

The overall goal of this thesis is to develop easy, fast and inexpensive techniques to fabricate large areas of nanostructure arrays on both inorganic and organic substrates and to study the

anti-reflection (AR) and anti-bacteria (AB) properties of the nano-engineered surfaces. Specifically, this thesis combined block copolymer micelle lithography (BCML) and reactive ion etching (RIE) techniques to fabricate a large-area of nanopillar and nanohole arrays on glass surfaces. The sample can be used as a mold for subsequent nanoimprinting process to transfer the nanostructures onto polymeric substrates. The method holds the potential to be a large-area and cost-effective nanostructure fabrication method for surfaces with high optical-transmittance and potential anti-bacterial properties.

1.2   Fabrication of nanostructures

1.2.1   Fabrication of nanostructures on inorganic materials

Techniques for nanofabrication can be generally classified into two categories: top-down and bottom-up methods. The top-down approach removes materials from a bulk substrate to achieve designed structures, for example, lithography/etching, molding and imprinting belong to this kind [20]. The bottom-up approach adds (or assembles) materials to the existing substrate, such as the methods of self-assembly [21].

Serial writing techniques such as electron beam (e-beam) lithography [22] and ion-beam lithography [23,24] are common methods used in scientific researches. Although these techniques have a high resolution, the writing process is very time-consuming and not suitable for applications that require a large surface area. Traditional optical lithography with UV light cannot achieve the resolution required to make nanostructures due to the diffraction limit. However, deep UV laser interference lithography provides a large-area nanolithography technique to make sub-wavelength nanostructures by exposing a photoresist layer with two or more coherent light beams [25]. Researchers in Fraunhofer ISE employed this method to prepare surface-relief grating mimicking the moth-eye structure for AR purposes [26,27]. However, the technique still requires a sophisticated optical interference set-up, the feature size is limited to hundreds of nanometers [28,29] and the sensitivity of the photoresist also influences the resolution of the nanostructures [29,30].

The most common bottom-up approach involves self-assembled monolayers. In order to achieve the monolayer, there are two basic strategies available: colloidal lithography and block copolymer micelle lithography (BCML). In colloidal lithography [31,32], mono-dispersed colloidal spheres are normally synthesized by sol-gel method [33]. By using different coating methods, *e.g.* the Langmuir-Blodgett device [34], patterned monolayers or multi-layers can be achieved on a surface and used as a mask for etching. The ion beam passes through the spaces in between the spheres and etches the substrate to form nano-scale structures. However, the method of colloidal monolayer formation only relies on attractive capillary forces and is therefore highly sensitive to the solution evaporation rate and the surface wetting properties of the substrate [35]. The prepared monolayer often has a problem of dewetting and results in grain boundaries over a large-scale surface [35-37]. Different from colloidal spheres, micelles are aggregates of block copolymers dispersed in polar or nonpolar solutions and the metal precursors can be loaded in the central core of the micelles. The pre-

pared micelles assemble into a monolayer on the substrate surface by using a dip- or spin-coating method [38]. The closed-packed micelle monolayer formed on the solid substrate surface is effected by both van der Waals interactions and capillary forces [39], which means that the interactions between micelles and the substrate surface are stronger than colloids. Therefore, it resolves the dewetting problem and provides a homogeneous monolayer compared to the colloidal lithography [39,40].

Hence, in this thesis, a bottom-up technique of BCML and a top-down technique of RIE are combined to fabricate nanostructure array on inorganic substrate. BCML is used to self-assemble a gold (Au) nanoparticle mask and RIE subsequently removes the material that is not covered by the Au nanoparticles to achieve the nanostructure array on SiO_2 substrate. The process combines the advantages of both approaches: 1) rapid and large-area mask preparation; and 2) high resolution and high aspect ratio fabrication.

1.2.2   Replication of nanostructures on polymeric materials

For the purpose of an industrial application, the scale-up method is often required for the fabrication of nanostructured surfaces. High-yield and low-cost are the most important aspects in the procedure. Compared to a direct preparation of the nanostructure via lithography or etching, the replication of the nanostructures from a mold shows many advantages: 1) a wide choice of materials; 2) a simple and rapid fabrication process; 3) negative nanostructures can be readily achieved; 4) a reuse of the mask and 5) low-cost. The replication of nanostructures with polymeric materials is often achieved by two methods, molding and nanoimprinting. In this thesis, both methods were used to replicate the nanostructures from the SiO_2 substrate to polymeric materials to equip them with AR properties.

Replica molding, which is one of the soft lithography methods, was developed by Whiteside *et al.* [19,41]. The main concept is to transfer the micro/nano-strucutres on a mold to an elastomeric material (*e.g.* polydimethylsiloxane or PDMS). The replication is achieved by forcing the liquid prepolymer into the micro/nano-gaps on the surface of the mold and curing the polymer followed by peeling it off from the mold. The polymeric structures can be used as an intermediate stamp for contact printing of chemicals, proteins and cells [42], or they can directly serve as microfluidic channels [43], sensors [44,45], micro-actuators [46] and so on. It is an important and popular micro/nano-fabrication method, as it offers the ability to make a micro/nano-patterning on biocompatible materials or even biomaterials (proteins and cells). It is also a convenient, inexpensive, and a large-area method for the replication of relatively large (micron-sized) features [47]. However, the high-yield replication of nano-scale features remains challenging.

The second nano-scale replication method is the nanoimprinting lithography [18,48], or hot embossing. Chou *et al.* [49] first reported the nanoimprinting lithography method as a nanometer scale fabrication method in 1995. The method is based on the properties of thermoplastic materials. Figure 1-1 shows a typical curve of the storage modulus versus the temperature of one important kind of thermoplastic materials, PMMA [50,51]. As the tempera-

ture increases, the polymer experiences three different states: hard elastic, viscoelastic and viscous. The temperature at the transition from the hard elastic to the viscoelastic state is called glass transition point. After the temperature rises above the glass transition point, the polymer becomes viscoelastic. As the temperature increases further, the polymer becomes more fluidic and, at this state, a fast nanoimprinting process can be carried out. The process cycle of the nanoimprinting [51,52] is depicted in Figure 1-2. The polymer is heated until it reaches the viscous state followed by an application of pressure to force the fluidic polymer into the micro/nano features of the mold surface. During the cooling down step, the pressure is kept until the polymer returns to an elastic state. The temperature where the frozen polymer occurs is called demolding temperature. After releasing the pressure, the polymer can be peeled off or lifted up from the mold and the negative nanostructures can be found on the polymeric surface.

Nanoimprinting transfers the nano-scale pattern by direct mechanical contact, therefore overcoming the restriction of the light diffraction limit. Furthermore it is also a very rapid, large-area and low-cost technique and has been extensively studied for the fabrication of sub-wavelength AR nanostructures. In earlier days, a negative Au mold was prepared from the bio-template of a cicada wing, which was then used for imprinting the nanostrucutres into PMMA [53]. Ting *et al.* [54] reported the preparation of the mold via a process of deep UV lithography, dry etching and Ni mold electroplating. The replication of the nanostructure into a polyethylene substrate was achieved using a roll-to-roll imprinting process. However, the final structures are relatively large with a spatial period of 400 nm and a diameter of 200 nm, thus AR property (reflectance lower than 2.45%) is limited to the visible light range of 400–700 nm. Furthermore, the preparation of the mold is a long and complicated process. Recently, a variety of molds were applied for the imprinting of AR nanostructures. For example, a template was made by a multiple-step anodizing and etching of an aluminum substrate. The created porous anodized aluminum oxide (AAO) (about 85 nm diameter and a periodicity of 100 nm) was imprinted into PMMA [55]. However, the AAO template had to be chemically dissolved to release the polymer structure and could therefore only be used once. Colloidal lithography and dry etching were also applied to prepare molds on silicon [56,57] substrates, however, as mentioned in Section 1.2.1 the colloidal monolayer was not homogeneous due to the grain boundaries and it likely influenced the physical and optical properties of the surfaces.

To my best knowledge, there are only a few examples of successful industrial applications of nanoimprinting [58,59]. It is mainly due to the difficulties and costs in the preparation of the delicate and expensive molds [60]. The key issue to solve these problems of using nanoimprinting is to fabricate a large-area, reusable and low-cost mold with nanostructures that are homogeneous and with tunable parameters. In this thesis, combining BCML and RIE processes provides an approach to address these issues.
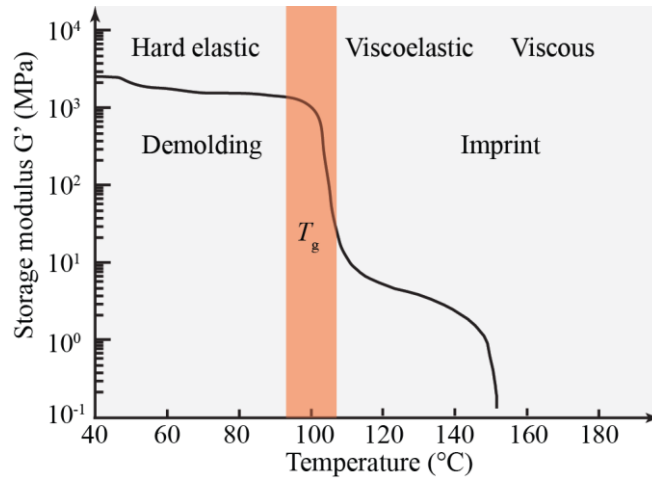
Figure 1-1: Storage modulus of PMMA dependent on temperature T_g of PMMA is around 100ºC. Above this temperature, the thermomechanical properties of PMMA changes from hard elastic to viscoelastic. Picture was adapted from [51].
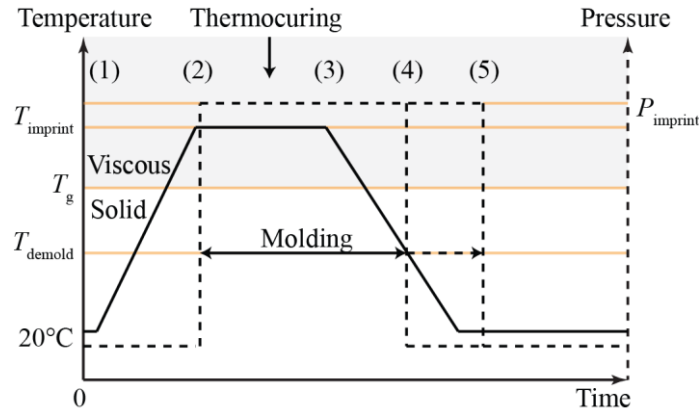
Figure 1-2: A typical process cycle of a nanoimprinting process. (1) heating-up step, (2) nanoimprinting/hot embossing step, (3) cooling step, (4) demolding at elevated temperature, and (5) demolding at room temperature. Picture was adapted from [51].

1.3 Anti-reflection (AR) property of nanostructured surfaces

1.3.1 Optical thin-film theory

The Fresnel reflection occurs due to the sudden change of the refractive indices at the interfaces between two different optical media, *e.g.* air and the substrate. It can be depicted by the formula [61]:

$$R = \left(\frac{n_{air} - n_{substrate}}{n_{air} + n_{substrate}}\right)^2 \qquad \text{(Equation 1-1)}$$

Where R is the total reflection, n_{air} and $n_{substrate}$ are the refractive indices of the air and the substrate.

In order to minimize this reflection loss, the destructive interference principle is utilized by adding a thin film layer on the substrate to reduce the reflectance as illustrated in Figure 1-3.

The thickness h should fulfill the formula to form an effective destructive interference when the incident angle is normal:

$$h = \frac{\lambda}{4n_{film}}$$ (Equation 1-2)

where λ is the wavelength of the incident light and n_{film} stands for the refractive index of the thin film layer. Therefore, the combined reflection is:

$$R = \left(\frac{n_{air}n_{substrate} - n_{film}^2}{n_{air}n_{substrate} + n_{film}^2}\right)^2$$ (Equation 1-3)

If the reflection R is supposed to be zero, the refractive index of the film should fulfill the formula:

$$n_{film} = \sqrt{n_{air}n_{substrate}}$$ (Equation 1-4)

Glass substrates for example have a refractive index of $n_{substrate}$=1.50, while air has a refractive index of n_{air}=1.0. It can be deduced that an ideal refractive index of the film should be 1.22. However, it is quite difficult to find or design a proper material with the refractive index exactly the same as the calculated value. The most typical and closest material used for a single layer anti-reflection coating is MgF_2 with a refractive index of 1.38 [61,62]. The obtained reflectance of the coated substrate is 1.4% which, compared with the reflectance of the uncoated glass being 4%, is an improvement. However, the anti-reflection of the thin film is highly dependent on the incident angle [63] and unstable under ambient conditions, such as heat, humidity and chemicals [64].

Air	n_{air}	=1.00
MgF_2	n_{film}	=1.38
Glass substrate	$n_{substrate}$	=1.50
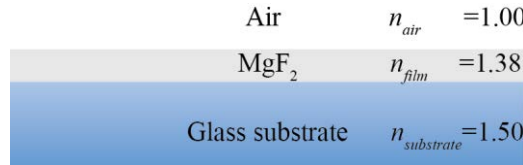
Figure 1-3: Single-layer coating of MgF_2 for anti-reflection on glass substrate.

1.3.2   The anti-reflection principle of moth-eye structures

Bernhard first observed the nano-protuberances on the moth eye under scanning electron microscope in 1967 [5]. The center-to-center distance between two protuberances is 200-250 nm and its height is approximately 250 nm [5]. By analyzing the eye surface structures of night-active and day-active insects, it was found that the corneal surface of day-active insects (*e.g.* bee) is smooth without any nanostructures, while that of night-active insects (*e.g.* moth) has homogenous distributed protuberance pattern. It was indicated that such fine nano-scale structures were used for anti-reflection in order to increase the amount of light passing through into the eye of the insect, and also minimize the reflection of the own eyes to avoid predators [40,65,66]. After Bernhard's publication, the novel "moth-eye" structure attracted lots of scientific attention. Hutley [6,67] was the first to fabricate an artificial nanostructure array to confirm the AR property of the moth-eye. After that, many theoretical works have

been carried out to explain the physical mechanism of the AR property and to simulate the best shape of the highly-ordered structure [68]. Additionally, a lot of artificial structures have been designed in order to mimic the structure of the moth eye [66,69-75].

The AR mechanism behind the moth-eye structure is shown in Figure 1-4, in which the refractive index of the substrate (n_2=1.5) gradually changes from the refractive index of the air (n_1=1.0) due to the sub-wavelength nanopillar array [68]. The best AR structural shape is the quintic-shape, which can be calculated theoretically [68] and is illustrated in Figure 1-5. However, the quintic-shaped nanopillar array is very difficult to be fabricated. Instead, similar sub-wavelength structures have been designed and studied.
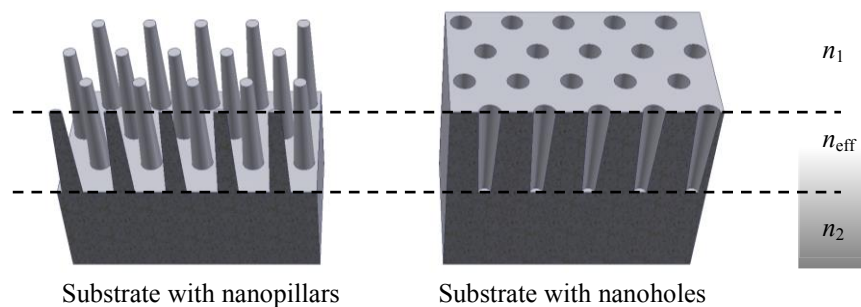
Figure 1-4: Illustration of the nanopillar and nanohole array in a cross-section view, which serve as an effective antireflection layer of the substrates. n_1 indicates the refractive index of the air, n_2 represents the refractive index of the substrate, and n_{eff} means the effective refractive index of the nanostructured array layer, which changes gradually from n$_1$ to n$_2$.
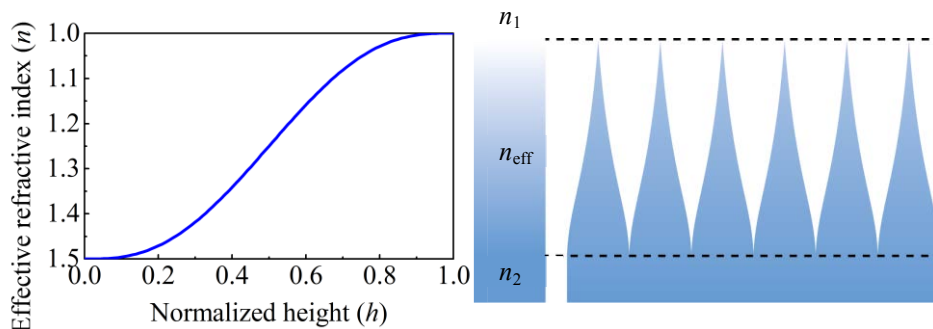
Figure 1-5: Sketch of the cross section of the ideal quintic nanopillar array. The nanopillar layer functions as an effective medium with a specific refractive index gradually changing from the refractive index of the Suprasil® (n_2=1.5) to that of the air (n_1=1.0). The figures were adapted from [68].

In optical theory, the moth-eye structure is often considered as an optical diffractive element with a surface-relief structure in two-dimension (2D) that only produces zero-ordered diffraction [29]. Since there is no closed solution for a 2D surface-relief structure, a 1D surface-relief or grating structure is often discussed [29]. As a beam of light goes through a grating, it can be described by the grating equation [76]:

11

$$n_{substrate} sin\theta_{substrate} - n_{air} sin\theta_{air} = \frac{m\lambda}{P} \qquad \text{(Equation 1-5)}$$

where $n_{substrate}$ and n_{air} are the refactive indices of the substrate and the air; $\theta_{substrate}$ represents the angle of the diffracted light beam and θ_{air} is the incident angle of the light; m means the diffracted order of the light; P stands for the periodicity of the grating and λ is the wavelength of the light. From the grating formula, it can be easily deduced that the periodicity should fulfill the condition as the formula below if there is only zero-ordered diffraction occuring:

$$P < \frac{\lambda}{n_{substrate} + n_{air}} \qquad \text{(Equation 1-6)}$$

Therefore, the moth-eye structure calls for nanostructures with sub-wavelength periods.

The required thickness of the moth-eye structure was first calculated by Rayleigh [77] in 1879. The reflectance depends on both the transition layer thickness (d) and the wavelength (λ). Figure 1-6 shows the reported simulation results of the reflection versus the ratio of structural depth over the wavelength. The inserted figure shows the gradually changing refractive indices of three different profiles. It can be seen that the reflection is high when d/λ is smaller than 0.2. As d/λ is increases, the reflection decreases dramatically until it reaches almost zero when d/λ equals 0.4. When the d/λ value increases further, the reflection of the linear shape structure has an alternating increase and decrease in a small range. For the optimized two shapes, *i.e.* quintic shape [68] (also called Klopfenstein structure) and the crossed sinusoidal shape, the reflections at larger depth (higher value of d/λ) are suppressed to almost zero. This theoretical analysis is based on the effective medium theory (EMT) [29], which is an effective modeling method to predict the AR performance of the nanostructures. It is also used to explain the experimental results in Section 4.7.4.
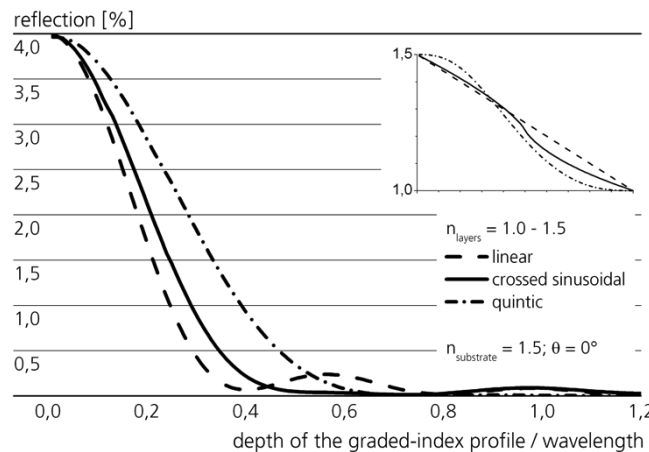

Figure 1-6: Calculated reflectance of gradually changing refractive index layers. The figure was taken from [29].

1.4 Anti-bacterial (AB) property of nanostructured surfaces

An anti-bacterial (AB) coating is critical for numerous applications, the most important of which is to protect sterilized medical instruments and implantable devices to prevent microbial infections [78-81]. Recently, AB coating finds more and more applications in other fields, *e.g.* food industry, homes and electronics [82-85]. The traditional ways of applying antibiotics and disinfectants do not fulfill all the needs, as they may support the development of resistant microbial strains and lead to environmental pollutions. Moreover, in some cases, apart from the AB properties, the same surface normally also acquires other surface properties, for example, a high optical transmittance. The surfaces of the protection glass on an endoscope, touch screen of electronics and contact lenses are all required to be both anti-reflective and anti-bacterial. A nanostructured surface coating provides a unique opportunity to combine both of these properties on one surface [86,87].

1.4.1 Influence of surface properties on anti-bacterial properties

Bacterial attachment to the surface is a complex process that is influenced by numerous interactions between the interface of the cell and the substrate [88]. The important parameters include the material mechanical properties (elastic modulus), fluidic environment (shear rates, pH, temperature, concentration of nutrients), surface energy (hydrophobicity), surface chemistry (functional groups, surface charges), and surface topology [87,89,90]. The latter three of these factors that are most relevant for this thesis are discussed below in detail.

Surface energy

Contradictory results are found in literature about the effect of surface energy on bacterial adhesion [91]. Hydrophobic surfaces (low surface energy) are found to reduce the attachment of micro-organisms in the oral cavity [92], however, hydrophilic surfaces (high surface energy) are also found to have similar bacterial reduction effect on *Staphylococcus aureus* [93]. Tegoulia cooper *et al.* [93] proposed a "water layer theory" to explain the anti-adhesion mechanism on the superhydrophilic surface: a dense water layer is formed due to the superhydophilicity, which prevents the contact between the bacteria and the surface. Vacheethasanee *et al.* [94] found an even more interesting phenomenon of *S. epidermidis* attaching on polymeric biomaterials with applied shear stess. Hydrophobic surface with contact angle larger than 70° enhanced bacterial adhesion and showed statistically higher bacterial coverage. For materials with contact angles smaller than 70°, the bacterial attachment was independent of the surface energy.

Surface chemistry

A traditional approach of AB material is to mix an anti-microbial agent with the material [95,96], *e.g.* quarternary ammonium compounds were widely used in disinfectant [83,97], silver was blended into polymers, ceramics and glass [98,99], and biocides were entrapped in the coating and released in a designed fashion [78,100]. However, a chemical modification of the surfaces is rarely preferable, as it can lead to some side effects such as cytotoxicity, in-

flammatory response, bacterial resistance [86]. It is worthwhile to mention that a chemical surface modification is often coupled with other factors. It can result in a change of the surface charge and hydrophobicity [87,101]. For example, bacterial adhesion is reduced on PMMA surfaces modified with acrylic acid due to its negatively charge [102]; polyethylene glycol (PEG) modification on polyurethane [103], mucin coating on PMMA [104] and oxygen glow discharge on polyvinylchlorid (PVC) [105] also decrease the bacteria adhesion due to their increased hydrophilicity. Since fabrication processes for the nanotopography can change the chemical composition of the surface, the possible effects on bacterial adhesion are important to keep in mind while designing the experiments [87].

Roughness and topography

Roughness and topography of the surface is a primary topic in AB coating studies [106]. To clarify the difference between roughness and topography [107], the roughness indicates randomly distributed micro/nano-structures with irregular shapes and a low aspect ratio; while the latter means patterned micro-nanostructures with controlled shapes and high aspect ratio. In earlier days, due to the lack of fabrication technologies for nano-structures, the surface roughness was investigated. It was reported that decreasing the roughness reduces the bacterial attachment, as less contact area as well as less attachment positions are offered and more fluid shear stress for the bacteria occurs [108]. However, this phenomenon was only observed within a certain range of the roughness and the threshold value varied a lot depending on the materials and the bacterial strains [109,110]. With recent developments in nanotechnology, the influence of the nanotopography on bacterial attachment could also be studied. On the one hand, many nanostructured surfaces were discovered on organisms in nature with AB property, such as the rice leaf [111] and the cicada wing [112]. On the other hand, inspired by nature, artificially patterned nanostructures were fabricated to gain AB properties. These structures include microstructures, such as Sharklet^TM surface, inhibiting the bacterial colonization and migration [113], and nanostructures, such as nano-cones on silicone [114], nano-rods on ZnO [115] and nanopillars on black silicon surface [116]. However, there were also reports about some nanostructured surfaces not triggering significant cellular response: For instance, there is no significant aggregation phenomenon of *Pseudomonas fluorescens* on nanostructured gold substrates compared with control substrates [117]. Anti-fouling studies were also carried out with microscale and sub-micron scale structures ranging from 500 nm to 2 μm feature size in microfluidic channels on PDMS material [118]. It was demonstrated that the topography shows no significantly better AB effect compared to the completely smooth surface. However, it was found that cells preferably attach to "recessed" patterns (holes or grooves) compared to "raised" patterns (pillars) [118]. Some of the typical artificial nanostructures with their important parameters and bacterial responses are summarized in Table 1-1.

Table 1-1: Artificial micro/nanostructures for AB purpose.

Structure	Width	Depth	Material	Bacteria studied	Response
Cone [114]	20, 30, 40 μm	4, 8, 13 μm	PDMS	*E. coli* *S. epidermidis*	Hinder biofilm formation
Nanowire [119]	300 nm	3 μm	Si	*S. oneidensis* MR-1	Recognition of nanowire array
Nanorod [115]	50 nm	500 nm	ZnO	*P. aeruginosa* *S. epidermidis*	Bactericidal
Sharklet[TM] [113,120]	2 μm	0.4 μm	Polyacrylate	*P. aeruginosa* *S. aureus*	Inhibit biofilm formation
Black silicon [116]	20-80 nm	500 nm	Si	*P. aeruginosa* *S. aureus* *B. subtilis* spores	Bactericidal
Grooves [117]	550 nm	120 nm	Au	*P. fluorescens*	No response
Pillars, holes, lines and Sharklet[TM] **pattern** [118]	500 nm-2 μm	500 nm-2 μm	PDMS	*P.aeruginosa*	No response "raised" feature (*e.g.* pillar) is better than "recessed" features (*e.g.* hole)

1.4.2 Bacterial features important for adhesion

The interaction between bacteria and material surfaces is often very complex, which poses a challenge for studying the AB surface properties and the underlying mechanism is still poorly understood. There are several features that should be considered investigating bacterial adhesion:

The cell wall of bacteria is quite rigid due to an external layer of peptidoglycan. In Gram-positive bacteria, this layer is thick; while in Gram-negative bacteria, it is thin and covered by an additional polysaccharide layer. The size of the bacteria is often small and they are less deformable as for instance eukaryotic cells, which may hinder the interaction between the bacteria and surface nanotopography with even smaller sizes. However, there is evidences that bacteria can sense nanosized features, as selectively listed in Table 1-1 and reviewed in [87]. Actually, as discussed above, bacteria are sensitive to multiple parameters in the environment, even minor differences in the surface chemistry or experimental treatment (solution replacement, fixation or freezing) of the bacteria may result in significant influence of the behavior and the morphology of the bacteria, which may cover the effect of topography [87]. Therefore, when conducting experiments with prokaryotic cells, special attention has to be

paid to control all parameters and keep them constant except for the one to be examined, *e.g.* nanotopography.

Some species of bacteria have flagella and fimbriae, some of which provide motility to the prokaryotic cells, interacting with nanostructures on the surface, and aiding bacterial adhesion to the surface [121]. It was proposed by Schmidt *et al.* [122] that the fimbriae play an important role in the bacteria-surface interaction. The fimbriae are less than 10 nm in diameter and difficult to observe by optical microscopy. Therefore in this thesis, besides the optical microscopy for calculating the surface coverage, SEM is used to observe the interface between the bacteria and the nanostructured surface.

Bacteria often form so called biofilms, which is an accumulation of bacteria embedded in an extracellular polymeric substance (EPS) [123]. The biofilm formation is divided into four steps as shown in Figure 1-7 [94,124]. First, the bacteria are transported to the substrate surface by gravity, Brownian motion or hydrodynamic forces [87]; second, bacteria are governed by long-range interactions with reversible physical attachment to the surface; third, bacteria irreversibly attach to the surface via physio-chemical or chemical interaction; and in the last step, bacteria start to proliferate and the biofilm matrix begins to form [87,101]. Once the biofilm is formed it is very difficult to remove and bacteria within the biofilm even resist to host immune responses and antibiotic therapies [79,125]. It is widely accepted that the material surface properties influence the second step of biofilm formation most [87,126]. For that reason, the AB surface designed in this thesis is mainly focused on preventing the second step and the timeline of the experiment is also accordingly determined.
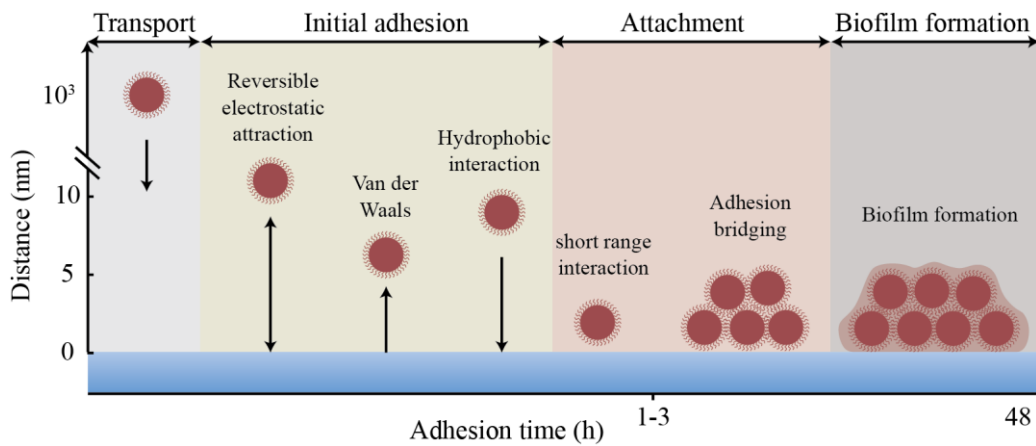

Figure 1-7: Four stages of biofilm formation on substrate surfaces. Picture was adapted from [94].

1.5   Thesis outline

Chapter 2 introduces general materials and experimental methods used in this thesis.

Chapter 3 describes the fabrication of the nanostructure array on inorganic. Nanopillar arrays are fabricated on SiO_2 substrates by combining BCML and RIE techniques. Besides SiO_2 substrate, nanopillar arrays are also prepared on other inorganic substrates, *i.e.* borosilicate, sapphire, stainless steel and SF10, with an extra SiO_2 layer sputtered on the surfaces. A sys-

tematic study is carried out to sweep the nanopillar height and inter-pillar spacing on the SiO_2 substrate to provide nanopillar arrays with controllable parameters.

Chapter 4 reports the replication of the nanostructures (both nanohole and nanopillar arrays) to organic materials (polymers) and the detailed study of the AR properties of such nanostructures. The SiO_2 substrates prepared previously serve as molds for two replication methods, *i.e.* replica molding and nanoimprinting. The transmittance spectra of SiO_2 molds and the imprinted polymeric substrates with nanostructures are measured. Excellent AR properties are shown on both kinds of materials with a wide range of wavelength and large range of incident angle. A theoretical model is also presented that predicts the optical property and matches the experimental results very well.

In Chapter 5, the AB properties are investigated on the nanopillar-structured SiO_2 substrates. The adhesion of the bacteria is statistically analyzed by optical microscopy and the morphology of the adhesion site of the bacteria to the nanopillar surface is observed by scanning electron microscopy (SEM). The observed morphological change of the cell verifies that the bacteria are able to sense and respond to the nanostructured surface, which may lead to some insights of the mechanism of bacterial attachment.

Chapter 2   General materials and methods

In this chapter, general experimental materials and methods that were applied in more than one chapters of this thesis are described. Detailed parameters and special methods for certain applications are reported in the respective chapters.

2.1   Overview

The SiO_2 substrates with sub-wavelength nanopillars described in this thesis were fabricated by combining block copolymer micelles lithography (BCML) and reactive ion etching (RIE) methods (Figure 2-1). First, a monolayer of highly ordered inverse micelles loaded with Au salt was prepared on a SiO_2 substrate by dip coating or spin coating method [39,40,75]. Second, the organic molecules were then removed via H_2/Ar plasma etching, which converted the Au precursors in each micelle into a single Au nanoparticle. In the third step, the Au nanoparticle array was used as an etching mask for subsequent reactive ion etching process. This process transferred the nanopattern into the SiO_2 substrate forming a quasi-hexagonal array of nanopillars on the surface. In order to replicate the nanopillar structures from fused silica substrate into different types of soft polymer materials, a nanoimprinting lithography system and hydraulic press were used.
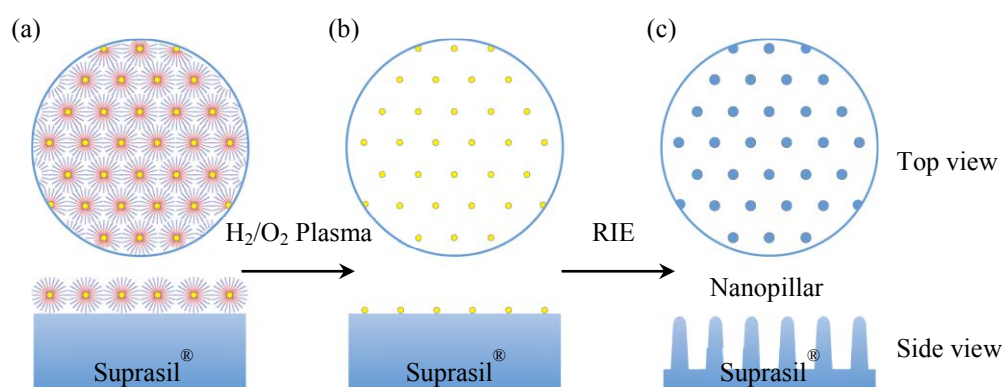

Figure 2-1: Preparation of nanopillar array on Suprasil® surface. (a) Au-loaded micelles were spin-coated on a Suprasil® substrate and (b) it was treated with H_2 plasma (0.4 mbar, 350 W) to covert the Au salt in the micelle core into a single nanoparticle. (c) With the Au nanoparticle array as an etching mask, a specific developed RIE process for Suprasil® substrate was applied to accomplish the nanopillar array.

After the nanofabrication, the optical properties of the nanopillars produced in various materials were characterized by a spectrophotometer and goniometer equipped with a reflection and transmission unit. In order to examine large areas of nanopillars from the top and the

cross section, morphology characterization of nanopillar molds and polymer replicas was performed by Scanning Electron Microscopy (SEM). For better vertical resolution and more precise parameter of nanostructures, Atomic Force Microscopy (AFM) was used. X-ray photoelectron spectroscopy (XPS) is a powerful tool in term of detecting elements and their chemical states of material surfaces. In this thesis, it was used to provide a full understanding of the chemical composition of the nanopillar surface. In the end, to investigate whether these nanopillar surfaces can influence the bacterial adhesion or not, anti-bacterial tests on SiO_2 substrates were studied by investigating the bacterial adhesion and growth with phase contrast microscopy. Relative bacterial concentration was controlled by measuring the optical density of incubated bacteria with a multimode-microplate reader. The micro- and nano-scale of the interactions between bacteria and substrate surface were studied by SEM with proper fixation and critical point drying approach.

2.2 Preparation of nanopillar arrays on SiO_2 substrates

2.2.1 Preparation of Au micelle solution

Au micelle solution was prepared by dissolving diblock copolymer poly (styrene)-b-poly (2-vinylpyridine) (PS-P2VP) (Polymer Source Inc., Montreal, Canada) in toluene (Merck, Darmstadt, Germany) at room temperature for a minimum of 12 hours with strong magnetic stirring. It formed spherical reverse micelles, which allowed for the addition of gold precursor ($HAuCl_4 \cdot 3H_2O$, Sigma-Aldrich, Germany) that penetrated the micelle and bound with the polymer in the core [38,39,127]. The used copolymers are listed in appendix (Table 6-3).

Gold particle size and inter-particle spacing could be varied by selecting different polymer molecular chain lengths and, in later in the protocol, spin coating speeds [39]. The precursor weight was calculated via:

$$m_{HAuCl_4} = \frac{m_{polymer} \times \text{Loading Rate} \times (m_{P2VP}/M_{P2VP}) \times M_{HAuCl_4 \cdot 3H_2O}}{M_{polymer}} \qquad \text{(Equation 2-1)}$$

, where m and M stand for mass and molecular weight. Loading rate was varied from 0.1 to 0.5. Different loading rate determined the volume of the Au nanoparticle, so the diameter of the particle could be adjusted via loading rate.

2.2.2 Preparation of Au nanoparticle arrays on SiO_2 substrates

Suprasil$^®$ substrates (SiO_2, 20 mm in diameter, Heraeus, Germany Substrates) was primarily used for nanostructures preparation. There were different substrates in thickness, *i.e.* 0.17 mm, 0.5 mm and 1 mm. The one with 0.17 mm thickness was mainly used for nanostructure characterization in detail. The thicker ones including 0.5 mm and 1 mm substrate were used for the nanostructure replication.

All of the substrates need to be cleaned before spin- or dip-coating with the micelle solution in order to remove organic residues and hydroxylate the surface. Substrates were immersed in

freshly prepared Piranha solution (3 parts H_2SO_4, ROTIPURAN®, 95-98%, Roth to 1 part 30% H_2O_2, EMPROVE®, Merck) for minimum 1 hour, followed by extensive rinsing in deionized water. The Piranha solution worked via the fast dehydration of concentrated sulfuric acid, followed by the strong oxidization of carbon, which was the product of the former dehydration step.

After cleaning, either dip coating (using a custom-made dip-coater with a step motor controlled by a power supply) or spin coating (WS-650HZ-23NPP/A2/AR2, Laurell) was performed to achieve a semi-hexagonal array of micelles on the substrate surfaces. The advantage of dip-coating was that the extracting speed can be continuously changed via adjusting the power supply voltage from 0 V to 30 V with speeding changing from 0 mm/min to 60 mm/min [72]. With this tuning function, varied inter-particle spacing on one sample surface could be achieved as the thickness of the micelle solution film changed with extraction speed. However, this method was very sensitive to environmental conditions, especially temperature and humidity [128,129]. The spin coating method could achieve a homogenous inter-particle spacing. Due to the rapid coating procedure (< 1 min) and the centrifugal force produced under high rotational speed, the toluene solvent evaporated quickly without severe effects on the micelles. A monolayer of Au precursor-loaded micelles formed on the substrate with a self-assembled and highly ordered pattern [130-132]. In this process, spin speed could be changed to vary the thickness of the micelle film, thereby allowing for controlling the inter-particle spacing. Here, spin speeds were adjusted from 1,000 – 12,000 rpm with inter-particle spacing from 25 nm to 250 nm as shown in Figure 2-2.

After spin coating, H_2/Ar plasma (10% H_2/90% Ar, TePla 100 Plasma System, PVA) was applied to remove organic molecules of the micelles, thereby transforming the Au precursor into single Au nanoparticles. Samples were exposed to the plasma generated by 350 W power for 45 min and the working pressure was kept at 0.4 mbar. Due to the plasma irradiation, Au nanoparticles firmly attach to the surface via covalent bonds while preserving the hexagonal pattern.
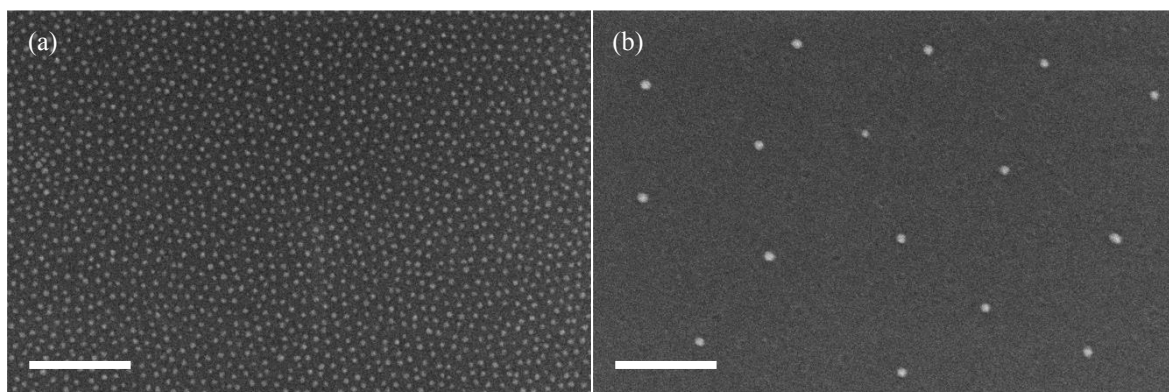

Figure 2-2: Au nanoparticles prepared on Suprasil® substrate with varied inter-particle distance, *i.e.* (a) 25.9±5.9 nm and (b) 258.8±44.1 nm. Scale bars: 200 nm.

2.2.3 Reactive Ion Etching (RIE) to produce nanopillar arrays

RIE (Oxford PlasmaLab80) was performed in order to transfer the nanoparticle pattern into the substrate, resulting in the formation of a nanopillar array [133].
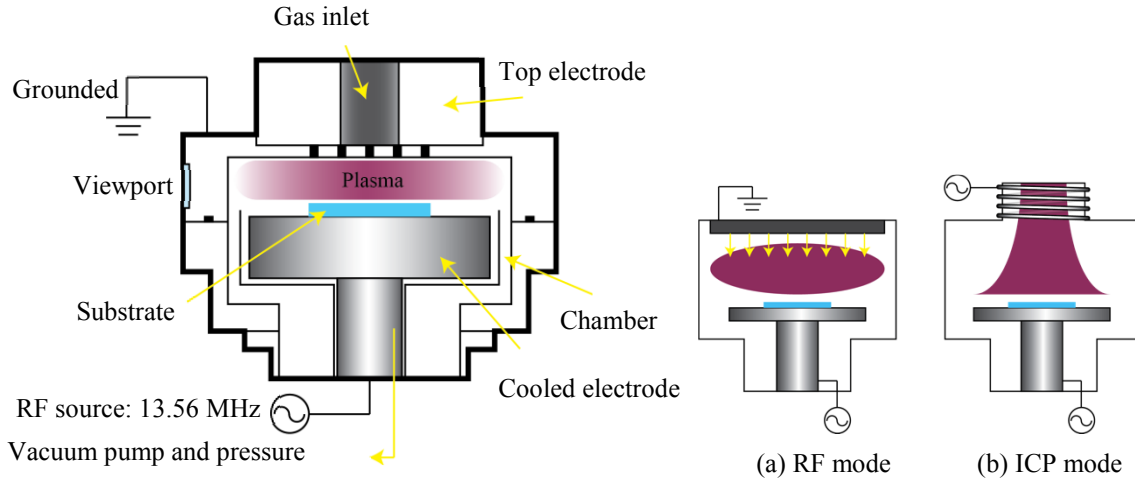

Figure 2-3: RIE system (left-hand side) and two modes used for high-aspect-ratio Suprasil® nanopillar preparation. (a) RF mode and (b) ICP mode. Picture was adapted from Oxford Instruments®.

This method is a common dry etching technique used in micro- and nanofabrication [133], achieved with different modes, *e.g.* radio frequency (RF) mode and induced couple plasma (ICP) mode as shown in Figure 2-3. Both of the modes were used in this thesis. Plasma was generated by the RF applied on a cooled electrode and was biased to the sample surface with the typical frequency of 13.56 MHz. The etching occurred as the chemical radicals were brought to the surface and the reaction products were pumped away because they were normally volatile. However, it was primary with physical bombardment toward the sample surface under RF mode. In other words, it was less anisotropic and with poor etching selectivity. In order to balance this, one method was to increase the bias voltage, accelerating the ions with more impacting energy. However, this method could severely damage the surface of the sample and the etching mask. Another method was to increase the density of reactive chemical radicals. Therefore, ICP mode was used in order to improve the anisotropy. In this mode, based on RF mode operation, another RF source was added at the top electrode in order to produce denser plasma with alternatively changed electromagnetic field.

Table 2-1: RIE process parameters for Suprasil® (SiO_2) substrates.

Steps	Gas	Flux (sccm)	Ar (sccm)	Pressure (mTorr)	RF power (W)	ICP power (W)	Time (s)
Etching	SF_6	40	40	50	120	0	60
Passivation	CHF_3	40	40	50	120	20	20

Detailed etching parameters used for nanopillar etching are shown in Table 2-1 [74,134]. By alternatively repeating this etching and passivation recipe (cycles), different heights of the nanopillar array were successfully obtained. The spacing and the diameter of the Au nanodots mask mainly determined the inter-pillar distance and the pillar diameter. As an example shown in Figure 2-4, the maximal pillar height prepared in this thesis was 400 nm after 7 RIE cycles with 100 nm in inter-pillar spacing and 85 nm in diameter.
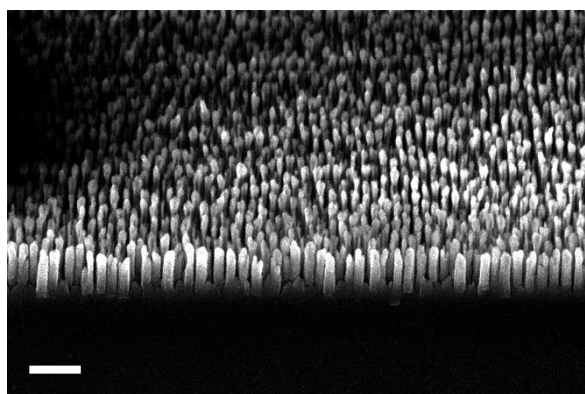
Figure 2-4: Nanopillar array prepared on SiO_2 (Suprasil®) substrate with a pillar height of 400 nm, an inter-pillar spacing of 100 nm and a diameter of 85 nm. Seven cycles of RIE process was applied. Scale bar: 400 nm.

2.3   Replication of nanostructures

2.3.1   Anti-adhesive surface preparation and contact angle measurement

In order to exploit the excellent AR and AB properties on polymeric, a fast, efficient and low cost replicatioin method was introdcued here to fabricate the nanostructures on polymeric materials.

An anti-adhesive layer was first deposited onto the nanopillar surface in order to decrease the surface energy, allowing for easier removal of polymeric materials from the mold [135,136]. As shown in Figure 2-5 (a), a thin layer of 1H, 1H, 2H, 2H-Perfluorodecyltrichlorosilane (FDTS, ABCR, Karlsruhe, Germany), was chemically bound to the surface via molecular vapor deposition (MVP) (custom set-up depicted in Figure 2-5). Substrates were placed in a beaker with ~20 µL silane solution and loaded into a desiccator. The system was then put under vacuum (cooled with liquid N_2) to ~5.0×10^{-1} mbar, at which point the silane evaporated and filled the entire chamber. Once the silane diffused onto the Suprasil® surface, the chemical covalent bond -Si-O-Si- formed between the substrate and FDTS because the hydroxyl groups of Suprasil® displaced the trichloro-silane groups of FDTS.

The wettability and surface energy directly correlate to the extent of silane deposition, which is critical for the demolding of polymers from the substrate. In order to investigate the wetting properties, the contact angle of each substrate was measured before and after silanization treatment. An Optical Contact Angle (OCA) system equipped with a high-speed camera (Dataphysics instruments, Filderstadt, Germany) was used to measure the static contact an-

gle. DI water with surface tension of 72.8 mN/m [137] was used to study the surface wetta-
bility and the volume of the solution was kept constant at 3 μL. Ten times measurements
were carried out on arbitrary spots for each sample surface. The obtained contact angles were
averaged and the deviations were calculated. In order to evaluate the surface energy, it re-
quires solutions with different liquid-vapor surface tensions to do the contact angle measure-
ment. Besides DI water, ethylene glycol (EG, 99.8%, Sigma-Aldrich, Germany) and ethanol
(ROTIPURAN®, 99.8%, Carl Roth, Germany) were selected in this thesis. The details of sur-
face energy experiment are described in Section 5.5.1.
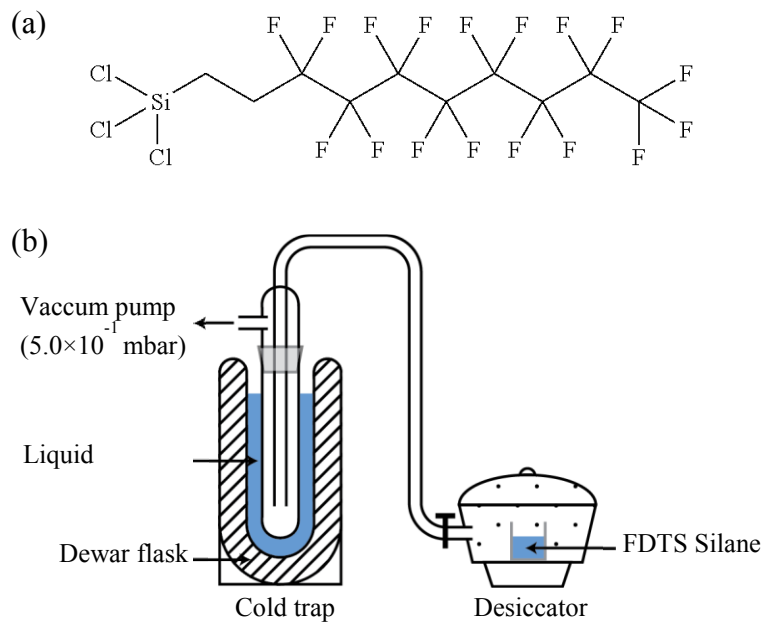
Figure 2-5: (a) Molecular structure of 1H, 1H, 2H, 2H-Perfluorodecyltrichlorosilane (FDTS). (b) Set-
up of silane vapor deposition.

2.3.2 Single-side replication of nanostructures to produce polymeric nanopillars and nanoholes

The first method used to replicate the nanopillar structure is a replica molding process. Two
schemes were designed for the molding process as shown in Figure 2-6. The sketch of pres-
sure molding set-up is shown in appendix (Figure 6-1). The substrate with FDTS-silanized
nanopillars was loaded between two parallel metal plates, on which it was covered by a mix-
ture of 2-component liquid polymer. Two-component polymers consisted of one monomer
component and one curing agent component. The force was applied by tightening the four
screws. The vacuum molding approach used the vacuum to remove the air between nanopil-
lars and supported the liquid polymer to fill the empty space between the nanostructures. The
vacuum was stabled within the pressure range between 10^{-1} mbar and 10^{-2} mbar. In order to
speed up the curing process of the polymer, normally the system needed to be heated up to a
specific temperature, for example 70°C for PDMS [138]. Limited by the maximum working
temperature of both set-ups, the molding process was only performed at room temperature
with long enough time until they were fully cured.

The two-component polymers used in the experiment are listed in Table 2-2 with typical characteristic viscosity and strength properties that are two important factors during the molding process. Polymdimethylsiloxane (PDMS, Sylgard® 184 silicon elastomer kit, Dow Corning) is a commonly used molding material, especially in microfluidics field, because of its excellent physical and biocompatible property. The other four materials, polyurethane (PU, Biothan® 2 MD 1775 XXXL mit Biodur M330 oder M333, Bioresin Limited, Emmerich am Rhein, Germany), MED-6020 (optically clear silicone elastomer, Nusil Technology, Carpinteria, Canada), MED-6215 (optically clear low consistency silicone elastomer, Nusil Technology, Carpinteria, Canada) and VT 3402 KK (Lackwerke Peters GmbH + Co KG, Kempen, Germany), are all medical grade and candidates for potential intraocular lens applications.
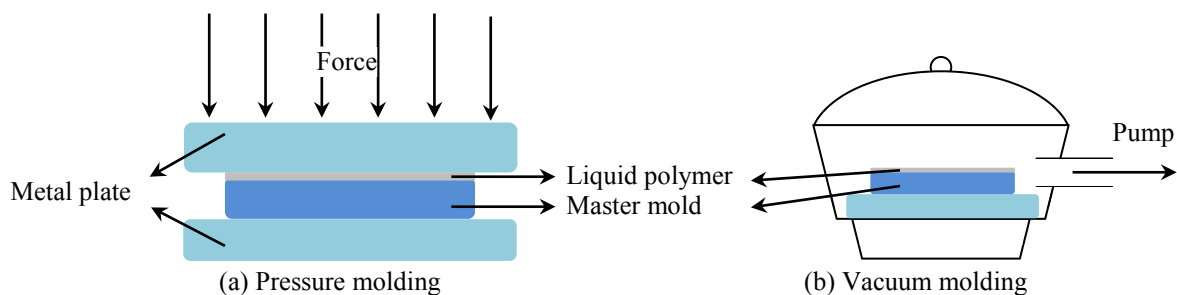
Figure 2-6: Replication of nanopillar structure with molding methods. Two approaches are used respectively: (a) pressure molding and (b) vacuum molding.

Table 2-2: Two-component polymers used in the molding process.

Polymers	Viscosity (mPa·s)	Strength (MPa)
PDMS	3500	7.1
PU (Biothan 2 MD)	1000-1800	>90
MED-6020	43000-63000	5.7
MED-6215	5000-5500	8.6
VT 3402 KK	2700	N.A.

Besides the molding process, another method used for the nanostructure replication is nanoimprinting, also called hot embossing. This method is mainly used for replicating the nanostructures with thermoplastic polymers and it requires successfully performed silanization step as well. The Commercial Obducat Eitre® system (Obducat, Sweden) shown in Figure 2-7 (a) was specially designed for nanoimprinting lithography in a clean room environment and was used here for hot imprinting standard samples with a total thickness of less than 1 mm (pressure and temperature can be independently and precisely controlled up to 40 bar and 200°C, respectively). In case of samples with thickness more than 1 mm and requiring temperature higher than 200°C, another hydraulic press set-up (Paul-Otto Weber, Remshalden, Germany) equipped with two movable metal plates and a temperature controller was also used showing in Figure 2-7 (b). This press can accommodate with much more thick-

er samples up to 20 cm and maximum working temperature up to 500°C. The position of the upper plate could be controlled and fixed by a screw jack, while pressure is applied through the lower plate via a hydraulic system. Since the two plates are rigid and the machine is not kept in a clean room environment, additional two layers of soft polydimethylsiloxane (PDMS) were added in between the mold and the metal plate in order to avoid contamination and damage of the mold, which can happen with sample misalignment or presence of small particles under the mold.
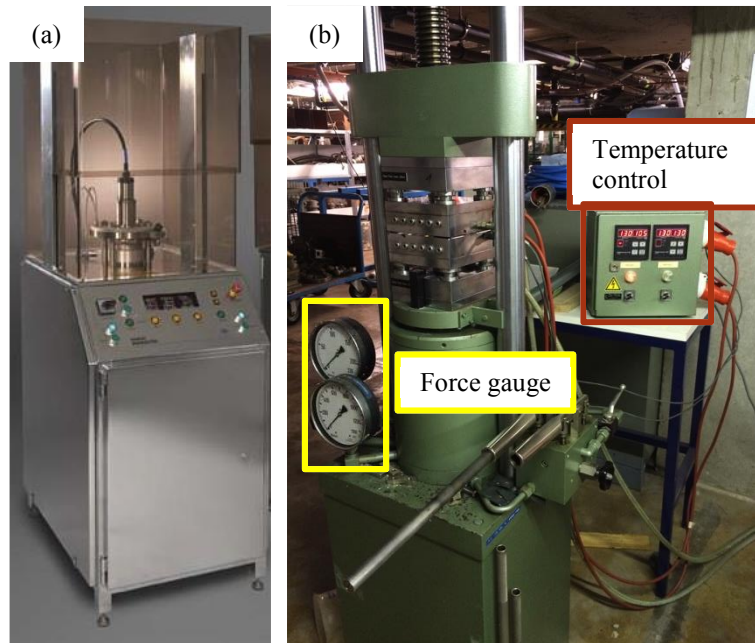
Figure 2-7: Nanoimprinting systems. (a) Obducat Eitre® nanoimprinting system with working temperature and pressure up to 200°C and 40 bar, respectively. The total thickness of the sandwiched sample (polymer+mold) cannot be thicker than 1 mm. (b) Hydraulic presser with temperature control (up to 500°C) and force gauge (up to 1360 kN).
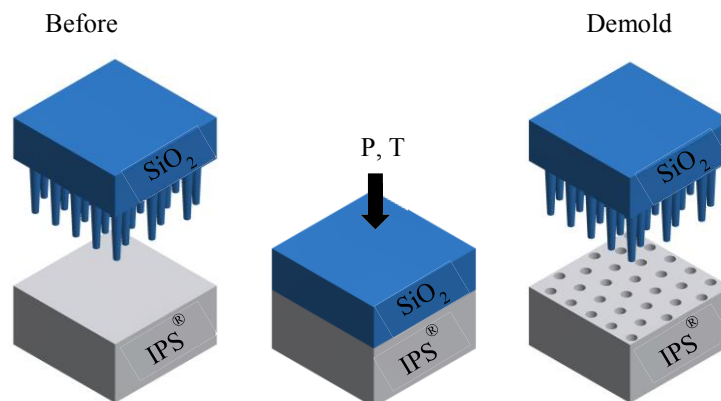
Figure 2-8: Schematic drawing of one-sided imprinting in IPS® polymer sheet with Suprasil® nanopillar substrate as a mold. Nanopillar arrays on Suprasil® were prepared by BCML and RIE techniques. Imprinting was performed at 160°C and 40 bar for 1 min; it was demolded at the temperature cooled down to 80°C.

Both machines utilize the same basic principles as shown in Figure 2-8. The mold and polymer were first aligned, and then the desired pressure and temperature were applied to decrease the polymer viscosity. This porcess allows the penetration of nanopillar structures into the polymer, thereby resulting in inverse nanopillar structures, *i.e.* nanoholes.

Eight types of thermoplastic polymer materials were tested and their properties compared in detail (summarized in Table 2-3). The imprinting temperatures were about 20-180°C higher than the glass transition point (T_g) and slightly lower than the melting point (T_m) of the polymers. IPS® (intermediate polymer stamp) was specially designed for nanoimprinting lithography. PMMA and Trogamid CX7323 were two polymers with high potential to be used for intraocular lens (IOL) application. CI26 (Contaflex 26% UV-IOL) is a commercially available polymer that can be directly processed into an IOL. Ethylene tetrafluoroethylene (ETFE) and polymethylpentene (PMP) are chemically stable and bioinert. Polyethylene terephthalate (PET) and polypropylene (PP) are commonly used as the protection film for smart phone screens. Specific imprinting and demolding temperatures and pressures for IPS®, PMMA and CI26 substrates will be mentioned in the results part where sample preparation will be described in more detail. Preparation parameters and measurement results of other substrates were summarzied in appendix (Table 6-2, Figure 6-3).

Both the Suprasil® and IPS® substrates in this thesis were used as molds for more than once. The repetitative use of Suprasil® as a mold is discussed in Section 4.4.1 and the using of IPS® substrate as a mold for PMMA substrate is described below in Section 0.

Table 2-3: Polymers studied for the replication of nanostructures.

Polymers	PMMA	ETFE	PMP	PET	PP	IPS®	CI26	CX7323
Dimension (mm)	0.175	0.125	0.125	0.175	0.180	0.160	3.000	0.200
Refractive Index (n)	1.49	1.40	1.46	1.58	NA	NA	1.51	1.52
T_g (°C)	105	90	20-40	70	-20	140	90-110	140
T_m (°C)	160	267	240	NA	NA	NA	NA	250
Supplier	Goodfellow, Great Britain					Obducat Sweden	Contamac, Great Britain	Evonik, Germany
T_m (°C)	160	267	240	NA	NA	NA	NA	250

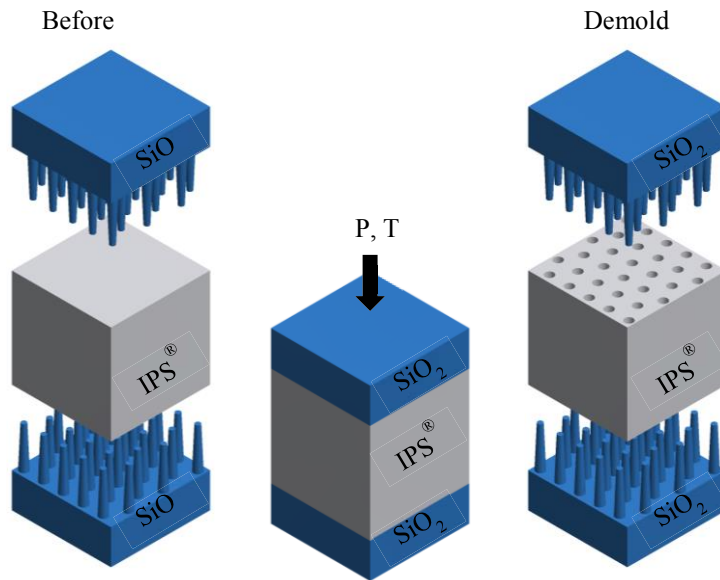### 2.3.3 Double-side replication of nanostructures to produce polymeric nanopillars and nanoholes

Figure 2-9: Schematic drawing of double-sided nanohole array preparation with two Suprasil® molds covered by nanopillar arrays. Suprasil® nanopillars were fabricated by BCML and RIE techniques. As the total thickness excessed 1 mm, nanoimprinting was performed using the hydraulic presser.
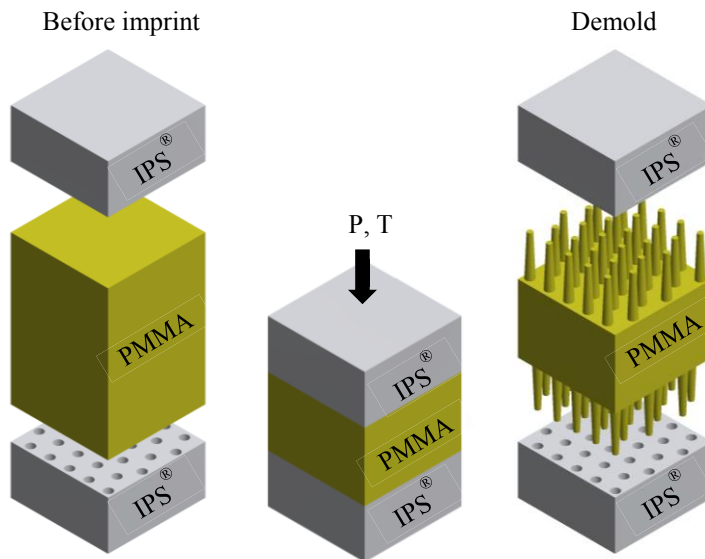
Figure 2-10: Schematic drawing of double-sided nanopillar array preparation with two imprinted IPS® molds covered by nanohole arrays. As all of those polymer sheets were 180 µm, the total thickness was less than 1 mm, the nanoimprinting was performed using the Obducat® nanoimprinter.

As discussed in the introduction chapter, the Fresnel reflection happens at the optical boundaries (air/substrate and substrate/air). Substrate with nanoholes on only one interface will thus still have strong reflection loss on the other interface (backside). Therefore, a double-sided

imprinted material is an ideal solution to minimize the optical reflection on both surfaces. With two parallel solid Suprasil® nanopillar substrate molds (Figure 2-9), nanoholes on both sides of the polymer (*e.g.* IPS®) can be achieved. These IPS® substrates with nanoholes can serve as nanoimprinting molds (Figure 2-10) as well. With these molds, nanostructures can also be further transferred into other polymeric materials, *e.g.* PMMA, with lower glass transition temperatures than that of the IPS® (T_g of PMMA is 35°C lower than that of IPS®).

As soft materials, one of the major advantages of using polymers is that they are flexible to be readily imprinted into a curved surface. In addition, nanostructures on both surfaces can also be imprinted in one step. Curved surface nanoimprinting is illustrated in Figure 2-11. Two molds with concave and convex surfaces were designed based on SiO$_2$ material (Suprasil®) On the surfaces of both molds it was prepared by nanopillar array structures with BCML technique and RIE process. After being deposited by an anti-adhesive layer, those two molds were directly used to imprint nanoholes onto the polymeric substrates in a similar manner to that of the plain surfaces.

A direct application of the curved polymer is the contact lens. Therefore, the base curvature of the polymer was designed as 8.4 mm^{-1}, which was reported to be the most comfortable curvature for human eyes [139]. The curvature of the lower and upper surface of the molds was designed to be 8.4 mm^{-1} and 7.9 mm^{-1}, with a focal length of -0.27 mm, and the Diopter, which is the reciprocal of the focal length, is -3.75 mm^{-1} or -3.75D. A detailed sketch of the molds' profiles is drawn in appendix (Figure 6-2).
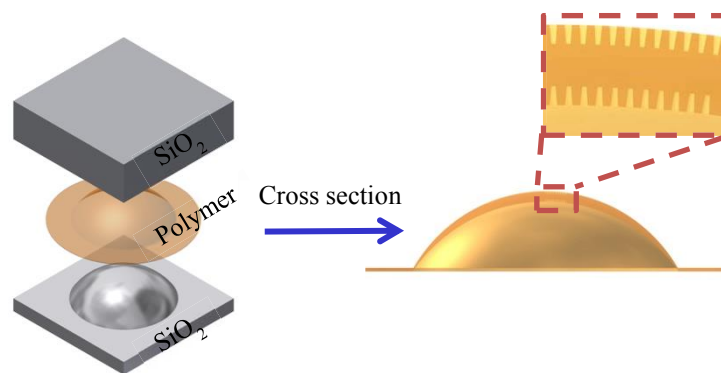
Figure 2-11: Diagram of curved polymeric surface nanoimprinting. The mold was made of Suprasil® and the nanopillar array was directly prepared on the surface by BCML and RIE techniques. Silanization with a FDTS monolayer on the surfaces allowed imprinting of polymers in between. The experiment was carried out with the hydraulic presser.

2.4   Characterization of nanopillar arrays

2.4.1   Morphological analysis via Scanning Electron Microscopy (SEM)

SEM (Microscope Ultra 55, Carl Zeiss, Jena, Germany) is a versatile technique in characterizing sample morphology, topography and compositions. Different information can be obtained by selectively detecting the multiple signals originated from the interaction of the elec-

tron beam and sample surface. Figure 2-12 depicts a typical interaction volume with different regions where the secondary electrons (SE), backscattered electrons (BSE) and characteristic X-rays are emitted. This volume is dependent on the energy of incident electron beam, the atomic weight and the sample position, *i.e.* perpendicular to the e beam or tilted. In brief [140], the SE signal originates near the surfaces with several nanometers to a couple of ten nanometers in diameter. The surface structure, morphology and topology are clear with SE signal. The BSE is mainly used for the chemical composition measurement due to its interaction with atomic nucleus. It is normally emitted from the volume with a fraction of micrometer. The characteristic X-rays often aim for the elemental and chemical analysis and they are produced from the sample surface with a volume in several micrometers.
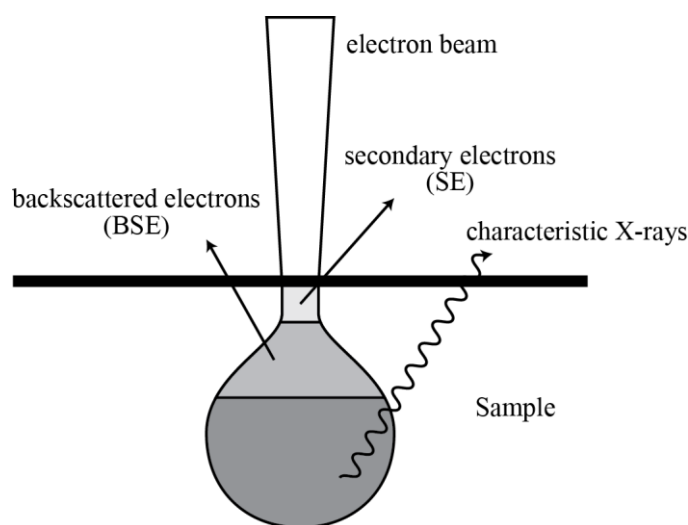
Figure 2-12: Interaction volume of e-beam at the sample surface. It shows the regions where the secondary electrons (SE), backscattered electrons (BSE) and characteristic X-rays are emitted. The picture was adapted from [140].

In this thesis, SEM was used to investigate the surface morphology of gold nanoparticles, silica nanopillars, and polymer nanoholes and pillars. Using secondary electron (SE) imaging mode with an In-Lens detector, size, spacing and hexagonal order of the arrays were readily observed. This mode was used because it has high lateral resolution due to its efficient collection of SEs, which was generated in a very small volume around the surface under illumination of the primary electron beam. Such interaction volume depth is usually around 1-2 nm, which determines the resolution of SE imaging. SE yield is almost independent of the material, but highly sensitive to the local radius of curvature; thus, SE images mainly provide information on surface morphology.

When non-conductive samples are exposed to the electron beam, an accumulation of excess electrons occurs over the surface. In order to avoid charge accumulation, the silica and polymeric substrates used in this thesis must be coated with a conductive layer. Normally, 10 nm-thick carbon or Au layer was deposited by using a thin film coating system (BAL-TEC MED020, Leica Microsystems, Wetzlar, Germany). Although Au thin film sputter deposition was widely used due to the excellent conductive properties of Au, the growth of islands lead-

ing to grain boundaries in the film strongly obstructed the observation of the nanostructured surface [141]. Therefore, thermal evaporation of carbon that did not produce islands was used.

Nanopillar height of the Suprasil® substrate was examined by cutting the substrate in order to obtain a cross section of the sample. However, the depth/height of the nanoholes/nanopillars on polymeric materials was much more difficult to be measured compard to the Suprasil® substrate. It was not possible to break the flexible polymer substrate at room temperature with a good view of the cross section. Thus, the polymer substrate was put in a dewar flask filled with liquid nitrogen and was broken with a better cross section as shown in Figure 2-13. However, this method was not reproducible and highly dependent on the type of polymers. Therefore, the depth of imprinted polymeric nanoholes and nanopillars were evaluated according to the previously measured pillar height of the substrate mold. And this estimation method is proven to be valid in Section 4.4.1.
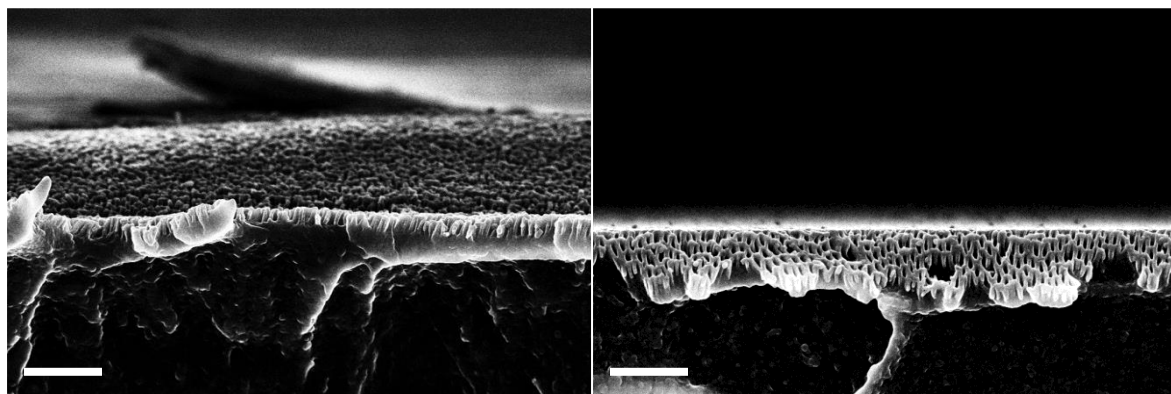
Figure 2-13: Cross sections of IPS® substrate imprinted with nanohole array. The inter-hole spacing was 100 nm and the depth of the hole was approximate 250 nm. The height of the nanopillar on the Suprasil® mold was approximate 250 nm as well. Scale bars: 1 μm.

The SEM images were analyzed in ImageJ (National Institutes of Health, USA) using a customized plug-in to analyze nanostructures, programmed by D. P. Girard [142,143]. Using this toolbox, the inter-particle spacing and the order parameter of the Au nanoparticles were readily achieved.

2.4.2 Nanoparticle size determination via Atomic Force Microscopy (AFM)

AFM is an approach for local surface structure and morphology measurement with high vertical resolution. Figure 2-14 shows an AFM detection system (MultiMode 8, Brucker, Massachusetts, USA). Driven by the Van der Waals force between the probe tip and the sample surface, the deflection of the cantilever is detected by a laser reflection into a photodiode. There are basically three imaging modes in AFM, *i.e.* contact mode, tapping mode and non-contact mode. In contact mode, the probe tip is brought in contact to the sample surface; thereby a small force is produced on the tip resulting the deflection of the cantilever. In non-contact mode, the probe tip is hung above the sample surface. Given an oscillation on the tip, the Van der Waals force between the tip and surface can be detected by measuring the change

in amplitude, frequency or phase of the cantilever. In tapping mode, it measures the frequency signal of the cantilever via a photodiode detector while keeping the amplitude constant. Compared to the other two modes, this approach can provide lower possibility of damaging the sample surface and the tip, which can occur under contact mode. In the meantime, it offers much better resolution than that of the non-contact mode. Therefore, the tapping mode is selected in this thesis.
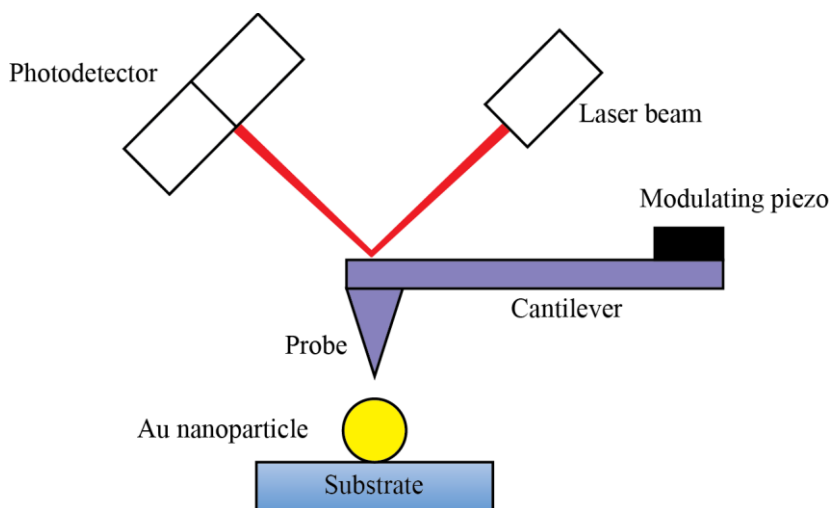

Figure 2-14: Schematic of an AFM system. It consists of scanning probe, cantilever, modulating piezo, laser beam and photodetector.

AFM was used to measure the size of Au nanoparticles, as SEM measurements cannot achieve accurate values due to the limited resolution [140] and the presence of a carbon layer that covers the particles with a certain thickness (~10 nm). AFM has a rough lateral resolution of 20 nm, while its vertical resolution is much more precise at ≤ 0.01 nm [144]. Au nanoparticles were assumed to be spherical and the more precise measured height value can be used as the diameter of nanoparticle. Tapping mode with a pyramidal SiO_2 tip (Nanosensors^{TM} PPP-NCHR, radius of curvature: <10 nm, force constant: 42 N/m, resonance frequency: 330 kHz) was used. This method can only be applied to the nanoparticle surfaces because the tip cannot properly scan the surfaces of high nanopillars or deep nanoholes (20-80 nm-diameter, 50-500 nm-height/depth, 50-250 nm-spacing), as evidenced by large fluctuations and distortion in the morphology of acquired AFM images due to the high aspect ratio profile. Thus, the heights of Suprasil$^{®}$ nanopillars were measured by SEM as discussed above. AFM images were analyzed by NanoScope Analysis Software (Brucker, Massachusetts, USA). The mean particle diameter was calculated by setting the threshold in depth histogram and detecting depths of all selected particles.

2.4.3 Optical property characterization

Two different spectrometers were used to measure the transmittance and reflectance properties of nanostructured samples.

A Cary 5000 spectrophotometer (Agilent, Califonia, USA) was primarily used for transmittance measurements in a broad wavelength range, from deep UV (200 nm) to near infrared (3000 nm), under double beam mode. Double beam mode utilized two parallel channels for the light beams to pass through air as a reference and a sample for data collecting. The light intensity from the sample channel was normalized by the intensity of the reference channel to measure the transmittance of the sample over different wavelength ranges. The detector and grating changed at the wavelength of 800 nm, the light source changed at 350 nm, and the transmittance was measured at a data interval of 1.0 nm. The diameter of the aperture in the sample holder, which was made of VeroBlack material and printed by a 3D printer (Objet 260 Connex, Stratasys, Israel), is 14 mm in diameter. Whenever the sample holder is changed, the background of the light source was re-measured.
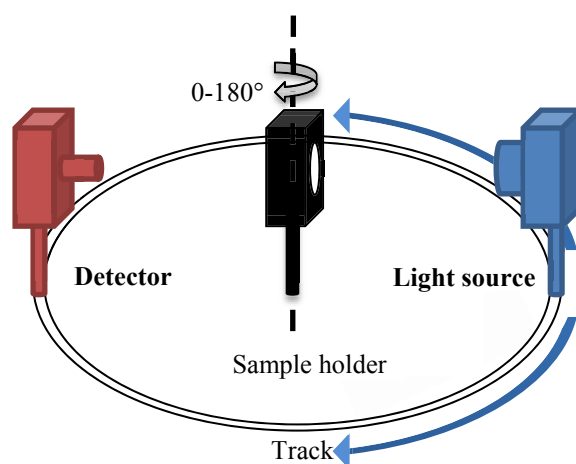
Figure 2-15: Sketch of the Goniometer for both reflection and transmission measurements. The angle of the transmittance can be measured from 0° to 60°. And the angle of reflectance can be measured from 10° to 60°.

A Goniometer equipped with a reflection and transmission unit (Omt, Ulm, Germany) was used for investigating transmittance and reflectance at different angles of incidence with a relatively short wavelength range, 380 nm - 1000 nm. The light source and detector of the set-up limit this wavelength range. This spectrometer operates with single beam mode. Therefore, the setup needs a warm-up step of 2 hours to stabilize the light source before each measurement. Otherwise, the light source intensity increases with the time during the measurement. As shown in Figure 2-15, the light source and sample stage can be rotated from 0° to 180°. The transmittance of a sample can be measured with an incident angle from 0° to 90° by only rotating sample stage. The reflectance of a sample can be measured with an incident angle from 8° to 90°.

2.5 Investigation of bacterial adhesion and growth on SiO$_2$ nanopillar surfaces

2.5.1 Bacterial strains and culturing conditions

Two bacteria strains were selected for investigating bacterial adhesion and growth on our nanopillar surfaces: *Escherichia coli* (*E. coli*, DH5α), which is gram-negative, and *Staphylococcus sciuri subspecies sciuri* (*S. sciuri subsp. sciuri*, DSMZ20345, Germany), which is gram-positive. Stocks of both strains were stored in glycerol in a -80°C freezer. For *E. coli*, Lysogeny Broth (LB) medium was prepared using LB tablets (10 g/L tryptone, 5 g/L yeast extract, 5 g/L NaCl, 2.2 g/L inert binding agents; Lennox, Sigma, Germany) dissolved in 1 L distilled deionized water (ddH$_2$O). For *S. sciuri*, Tryptic Soy Broth (TSB, Merck, Germany) medium was prepared by dissolving 30g in 1 L ddH$_2$O, along with 3 g Yeast (Sigma, Germany). To avoid the cross-contamination of unexpected bacteria, all experiments relating to bacteria was performed under sterile conditions in a biological safety cabinet (Herasafe, Thermo scientific, Massachusetts, USA). All glassware, before and after use, was burned by an alcohol blast burner. All medium, PBS and ddH$_2$O, were autoclaved (Systec V150, Wettenberg, Germany) at 120°C for 20 minutes.

As the bacteria were frozen, they needed time to recover until they reach normal metabolism. *S. sciuri* was pre-warmed one night before by incubating in TSB medium (50 mL) placed in an incubator (Certomat$^®$ BS-1, Sartorius Stedim Biotech, Göttingen, Germany) at 37°C with shaking speed of 225 rpm. In order to quantitatively control the bacterial concentration, a new bacteria culture solution was prepared by diluting the original culture 1:500 (*i.e.* 100 μL bacterial culture from the dense overnight culture and 50 mL TSB medium). The optical density (OD) of the new solution was indicative of the relative bacterial concentration, and was examined every 30 min until it reached an exponential phase using a spectrophotometer (Tecan infinite$^®$ M200, Männerdorf, Switzerland) at a wavelength of 600 nm (OD600). A hemocytometer (Neubauer Improved, LO-Labor optik, Bad-Homburg, Germany) was also used in conjunction with the plate reader to determine absolute bacterial concentration (cells/mL). Plotting the optical density and coverage against time in a linear scale or a logarithmic scale, a typical bacterial growth curve was achieved. The adhesion and growth experiment on nanopillars was performed once the bacterial OD600 reached approximately 0.2, which was when the exponential growth occurred.

2.5.2 Bacterial adhesion and growth on SiO$_2$ nanopillars

Figure 2-16 shows the experimental setup of bacterial adhesion and growth on Suprasil$^®$ nanopillar substrates. The prepared samples were first transferred into 6-well plates and incubated with 3 mL bacteria solution in a 37°C incubator (Heraeus Heracell 240, Thermo scientific, Massachusetts, USA). At 20 and 40 min, after incubation, the bacteria that settled onto the substrates were recorded by phase contrast microscopy. When the surface coverage reached saturation, the bacterial culture solution was extensively rinsed by phosphate buffered saline (PBS, Gibco$^®$ Lifetechnologies, Darmstadt, Germany) such that the bacteria that

were not firmly attached to the surface were washed away. Clean TSB medium was then added and the growth of the attached bacteria were observed. During this step, the bacterial growth on the surfaces was recorded every 60 min until reaching saturation coverage again. The obtained images were analyzed using the image analysis module of Matlab, and the area coverage was calculated.
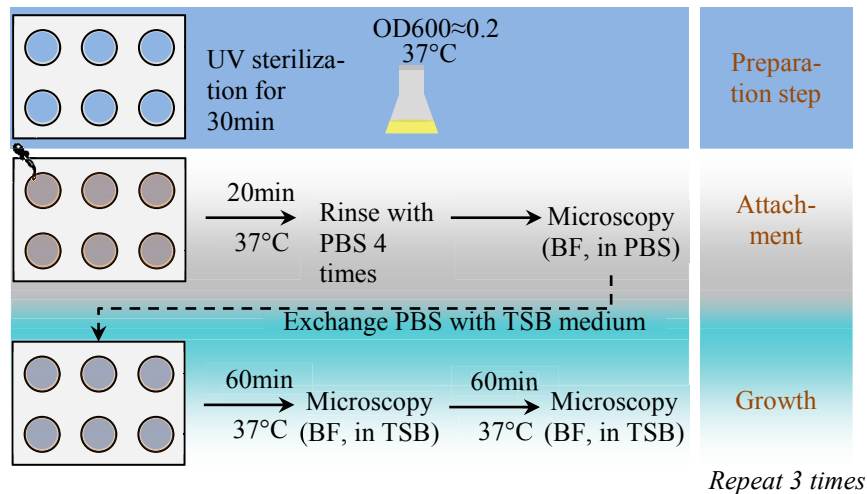

Figure 2-16: Bacterial adhesion and growth experimental setup. Substrates were loaded in the 6-well plate and exposed to UV light for 30 min for sterilization. The bacterial culture solution was incubated at 37°C in a shaker. Once the OD600 reached to 0.2, the bacterial culture was added into the 6-well plate, 3 ml for each well, to fully cover the substrate. After 20 min incubation under 37°C, samples were thoroughly rinsed by PBS and observed by optical microscopy to study the attachment of bacteria. For a further investigation of bacterial growth, PBS was exchanged by TSB medium and samples were incubated again at 37°C. BF means bright field mode of the microscopy.

2.5.3 Quantification of bacterial surface coverage

Imaging was performed in phase contrast mode with an inverted Axiovert 200M microscope (objective lenses: 40X NA=0.6 / 20X NA=0.4, Zeiss, Germany) in order to visually observe bacterial attachment and growth. To obtain a sufficient sample size, bacterial coverage should be observed for a large area, requiring a low magnification; however, due to the small bacteria size (1-2 μm), phase contrast mode must be used in order to observe distinct edges of the bacteria compared to the background at such magnification. Phase contrast mode works by converting the brightness of the recorded images via the phase shift of the light as it passes through the sample. In order to obtain enough statistical power of the large recorded areas without confounding the data due to time-dependent bacterial growth, five images at random positions were recorded for every sample. The obtained images were analyzed using Matlab (Mathworks®, US). Briefly, the images were loaded in gray scale and converted into black and white images with a threshold. The bacteria appear in white color and the uncovered area is with black color. The coverage of the bacteria was calculated by dividing the quantities of the black pixels to the total pixels of the image. Take the bacteria seeded on plain Suprasil® substrate as an example which is shown in Figure 2-17, the calculated bacterial coverage is 16.67%.
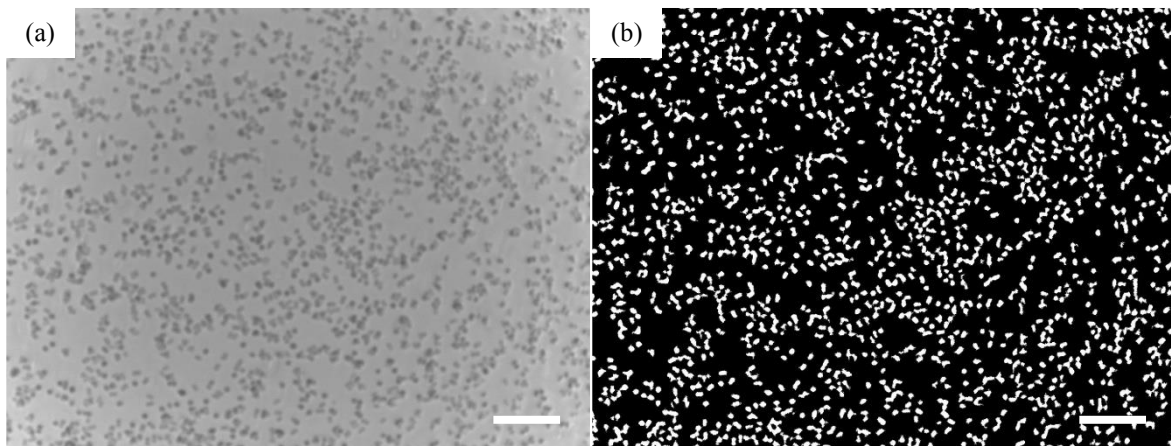
Figure 2-17: *S. sciuri* seeded on planar Suprasil® substrate. (a) Phase contrast image of the bacteria and (b) The converted binary image for bacterial coverage calculation. The calculated coverage is 16.67%. Scale bars: 25 μm.

2.5.4 Hemocytometer

A hemocytometer (Neubauer, Blau Brand, 0.100 mm depth) is a device for counting cells. It consists of two chambers, each with nine 1 mm × 1 mm squares (Figure 6-4). The bacterial culture solution was added using the capillary force between the cover slip and the chamber surface. By counting the bacteria presenting in the four middle squares (200 μm × 200 μm) located at the four angles of the central square (1 mm × 1 mm), the bacterial concentration in original solution can be calculated according to (Equation 2-2).

$$concentration\ (ml^{-1}) = \frac{number\ of\ bacteria\ counted}{4 \times (0.004\ mm^3)} \cdot dilution\ ratio \quad \text{(Equation 2-2)}$$

2.5.5 Critical point drying

Biological samples must be fixed and dried before observing with a SEM. If the sample is dried in air, the surface tension of the water inside the bacteria will damage their structure due to the phase changing from liquid to gas. Thus, critical point drying (Bal-Tec CPD 030 Critical Point Dryer, Leica Microsystems, Germany) is a method used to dry biological samples without damaging them. The bacterial sample was first fixed with PFA (paraformaldehyde) and then thoroughly rinsed with PBS. The PBS was then gradually exchanged with ethanol solutions (diluted with PBS, ranging from 10% to 100 %, with a 10% increment) in order to avoid any damage of the cytoskeleton due to differences in osmotic pressure. At each step, the sample was kept in the ethanol solution for 15 min., with two exchanges for the last step of 100% ethanol (ROTIPURAN®, 99.8%, Carl Roth, Germany).

For critical point drying, the sample was loaded into the chamber that was filled with ethanol. Once the temperature decreased to 10°C, the dry agent (liquid CO_2) was added into the chamber, mixed with the ethanol inside. The mixture was drained until the liquid interface was just above the sample. The filling and the draining were repeated for 7 times until the interface between the ethanol and liquid CO_2 disappeared, which indicates the ethanol was

completely exchanged by liquid CO_2. The cooling process was then stopped and the system was heated up. As the temperature was raised to 40°C, the liquid CO_2 transited into the gas phase without going through the liquid-gas boundary [145] (pressure 50-80 bar, no higher than 80 bar). Using this method, the morphology of the bacteria was successfully preserved and the sample was then coated with carbon for SEM observation.

Chapter 3   Fabrication of the nanopillar arrays on inorganic substrates

3.1   Overview

Block Copolymer Micelle Nanolithography (BCML) followed by Reactive Ion Etching (RIE) [40,75] is used to fabricate highly precise nanopillar arrays on Suprasil® and other substrates. In order to explore potential applications of the SiO_2 nanopillar arrays, various parameters are investigated systematically. Several topics are discussed in detail in each of the following chapters, in relation to either the height or the interspacing of nanopillars. Specifically, we explore optical transmittance properties (Chapter 4), replication using nanoimprinting technique (Chapter 4), and the influence of nanostructured surfaces on bacterial attachment and growth (Chapter 5).

The height and spacing of the nanopillars are influenced by several factors. The spacing can be modified during the BCML process by adjusting the polymer chain length, polymer concentration and spin coating speed. The height can be tuned via etching time (number of cycles) of the RIE process and Au nanoparticle size. Various substrates for different applications were also examined for nanopillar preparation, including Suprasil®, borosilicate glass, sapphire, SF10 and stainless steel. In the following sections, we will focus on sample preparation on each substrate.

3.2   Control of nanopillar height on Suprasil® substrate

3.2.1   Reactive ion etching cycle time

The height of the nanopillars is influenced by RIE cycle time and the size of the Au nanoparticles deposited before etching. Using Au nanoparticles of 9.28±1.4 nm diameter and a spacing of 101±15 nm made with 1056-*b*-671 polymer (Figure 3-1), the pillar height can be varied from 50 nm up to 400 nm by adjusting etching time (Figure 3-2). The relationship between the height of the pillars and the cycle time is clear: more RIE cycles result in larger pillar height as shown by SEM images of cross-sections of various etching times (Figure 3-2). Longer etching time also results in an increase of pillar diameter from 30±5 nm to 80±5 nm, thereby reducing residual spacing between pillars from 60±5 nm down to 10±5 nm. Such narrow inter-pillar spacing hinders ion etching, which dramatically slows down the etching rate, resulting in a limit to the pillar height. Moreover, longer etching processes promote the

deposition of SiO_xF_y and fluorocarbons onto the surface, which inhibits the vertical etching as well.
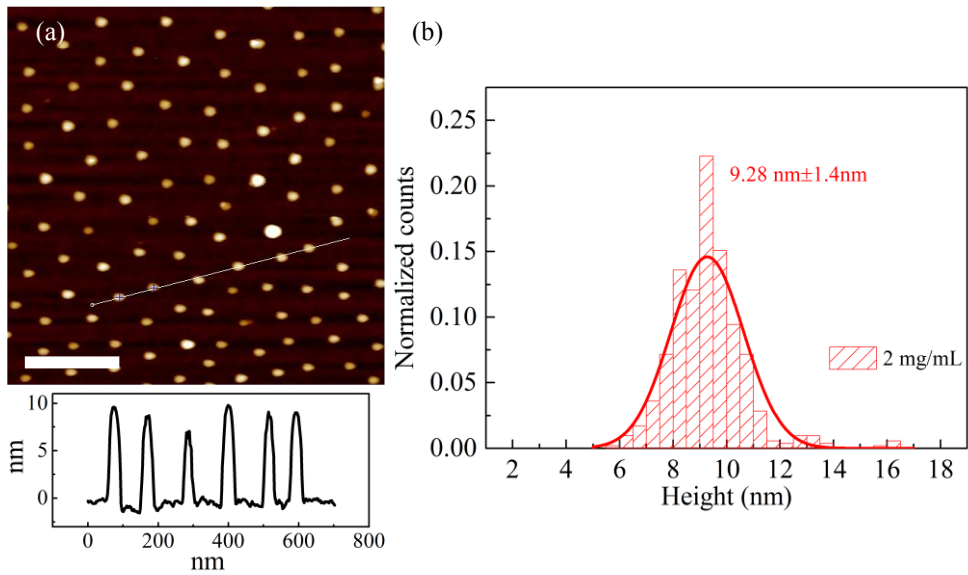
Figure 3-1: AFM topography measurement of the Au nanoparticles used for the etching mask (top image) and the measured height profile of the nanoparticles with inter-particle spacing of around (a) 105 nm (bottom image). (b) The measured Au nanoparticle diameter distribution.
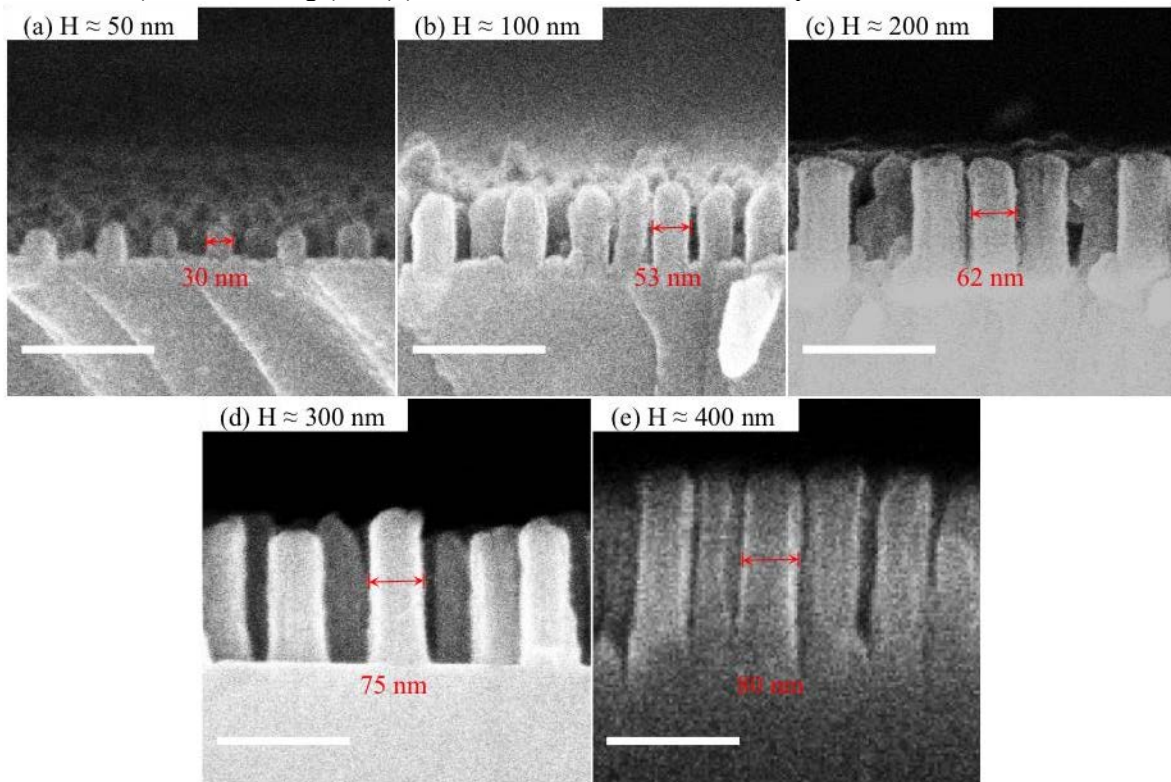
Figure 3-2: SEM images of cross sections of the Suprasil nanopillar array with heights changing from 50 nm to 400 nm by varying the RIE cycles. 50 nm: 1 cycle; 100 nm: 2 cycles; 200 nn: 4 cycles; 300 nm: 6 cycles; 400 nm: 7 cycles. The diameters of the pillars are indicated in the images. Scale bars: 200 nm.

3.2.2 Diameter of the Au nanoparticle

The second parameter affecting nanopillar height is the diameter of Au nanoparticles which serve as a mask prior to etching. Larger diameter, and thereby larger volume, increases the length of time the mask can work in the etching process, allowing for greater nanopillar heights.

The Au nanoparticle size is dependent on the molecular weight of block copolymers. There is a relation reported by Förster *et al.* [146] :

$$Z = Z_0\left(N_{P2VP}{}^{\alpha}N_{PS}{}^{-\beta}\right) \qquad \text{(Equation 3-1)}$$

Here, Z stands for the aggregation number, *i.e.* the number of copolymer molecules per micelle, and N_{P2VP} and N_{PS} are the degrees of polymerization of the two blocks [147]. The experimental values of α and β are reported as 1.71 [148] and 0.79 [146], respectively. Z_0 is a coefficient that can be deduced from previous experiments [148], wich is1.48. The loading rate used for experiments is 0.5. The reduced Au nanoparticle is supposed to be perfect face centered cubic (FCC) structure and the lattice constant is 4.065 Å [149]. Using this model, the size of Au nanoparticle is calculated to be 6.0 nm, 11.3 nm and 16.4 nm, in order of increasing polymer molecular weight for the polymers 240-*b*-143, 5343-*b*-713 and 1056-*b*-671.

Figure 3-3 summarizes Au nanoparticle size depending on the polymer molecular weight, *i.e.* 3.74±0.66 nm for polymer 240-*b*-143 (shortest polymer chain length), 7.00±1.07 nm for polymer 5343-*b*-713 (medium polymer chain length) and 9.44±0.88 nm for polymer 1056-*b*-671 (longest polymer chain length). All solutions were prepared at 0.2 mg/mL, with an Au loading rate of 0.5. The height of the nanoparticles was analyzed via AFM, and assuming a perfect spherical shape, the height is equal to the diameter of the particle. Although the measured values are slightly different from the calculated ones, the trend of increasing particle size with increasing polymer chain length is consistent with the size-based molecular weight dependency.

When RIE remains constant at 6 cycles, Au nanoparticles with different diameters result in different pillar heights as shown in Figure 3-4. The sample with a 3.74±0.68 nm diameter Au nanoparticle mask results in nanopillars with height of 160±10 nm, 7.00±1.07 nm diameter results in 220±10 nm high pillars, and 9.44±0.88 nm diameter results in 260±10 nm high pillars. Therefore, the volume of the Au nanoparticle mask influences nanopillar height, with larger nanoparticles producing higher nanopillars.
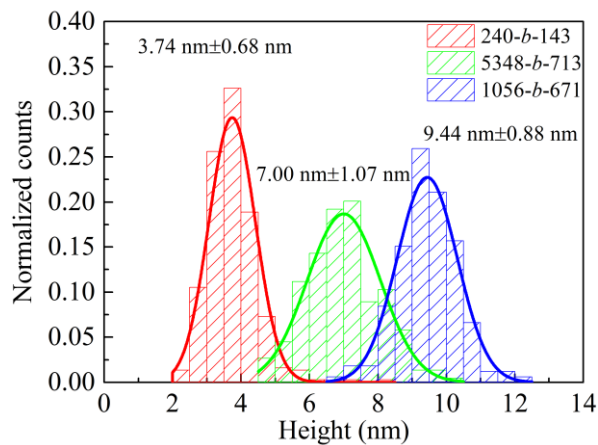
Figure 3-3: Distribution of the gold nanoparticle diameters measured by AFM. The diameter increases with increasing polymer chain lengths. All other experimental values were kept the same. Au salt loading rate: 0.5; polymer concentration: 0.2 mg/mL; spin coating speed: 8000 rpm.
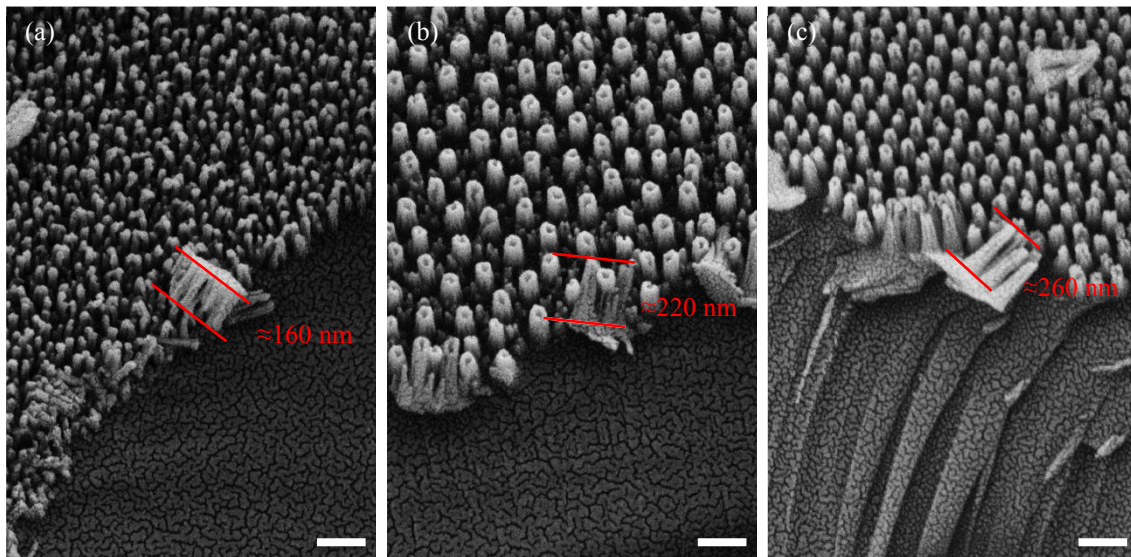
Figure 3-4: Different pillar heights obtained from different Au nanoparticle diameters. RIE processes are all set to 6 cycles. (a) Pillar height: 160 nm; Au diameter: 3.74±0.68 nm. (b) Pillar height: 220 nm; Au diameter: 7.00±1.07 nm. (c) Pillar height: 260 nm; Au diameter: 9.44±0.88 nm. Scale bars: 200 nm.

3.3 Control of inter-pillar spacing on Suprasil® substrate

3.3.1 Spin-coating speed and polymer concentration

There are three factors that can influence Au nanoparticle spacing, and therefore inter-pillar spacing: spin-coating speed, polymer concentration and polymer chain length [39,72]. Here we examine the effects of Au nanoparticle distribution on inter-pillar spacing by varying the spin-coating speed, ranging from 2000 rpm to 12000 rpm, and polymer concentration, examined at 2 mg/mL, 3 mg/mL and 4 mg/mL. Although the polymer concentration is altered, a similar diameter of Au nanoparticles can still be achieved for the same type of polymer (here we used 1056-*b*-671), which is approximate 9.5 nm according to the topography measure-

ments performed by AFM (Figure 3-5 and Figure 3-6). It is important to keep the Au nanoparticle diameter constant in order to maintain nanopillar height and diameter, such that only the inter-pillar spacing is varied.
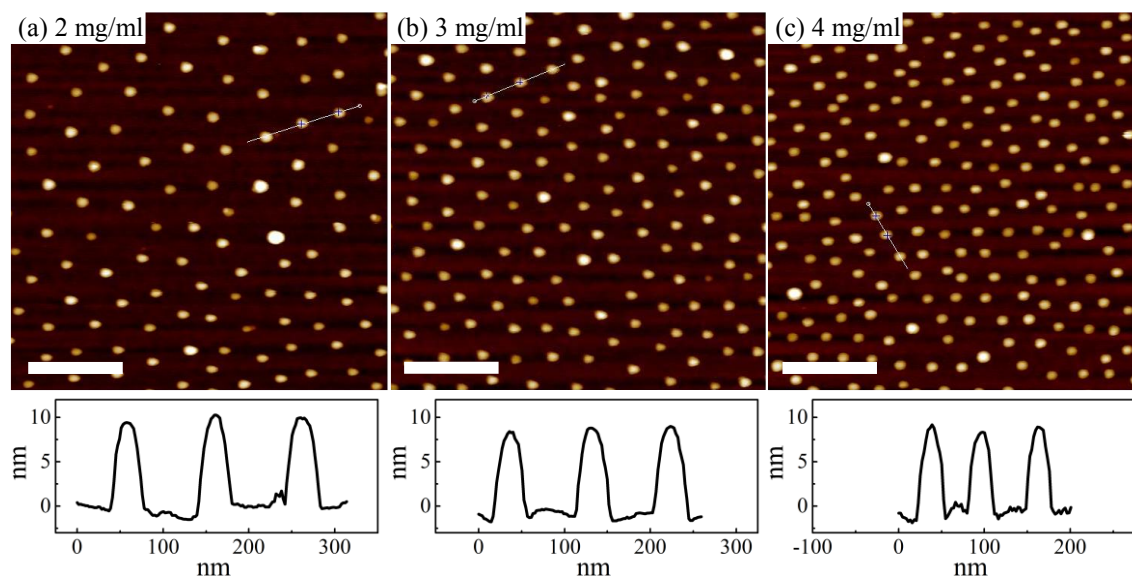
Figure 3-5: AFM topography image of the Au nanoparticles prepared from different concentration of the micelle solutions: (a) 2 mg/mL, (b) 3 mg/mL and (c) 4 mg/mL on silicon wafer with 1056-*b*-671 polymer. The height profile and the height variations are comparable to each other. All of the measured nanoparticles are summarized in Figure 3-6. Scale bars: 250 nm.
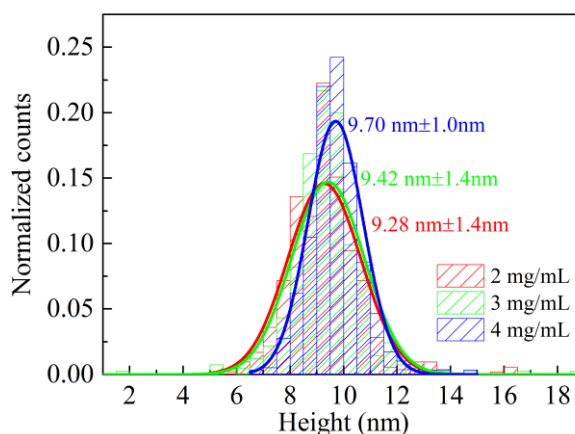
Figure 3-6: Size distribution of the gold nanoparticle diameters obtained by using the same polymer (1056-b-671) but different concentrations (2 mg/mL, 3 mg/mL and 4 mg/mL) to prepare the micelle solution.

Inter-particle spacings resulted from adjusting these two parameters are summarized in Figure 3-7 (SEM pictures) and Figure 3-8 (quantified results). In each column of Figure 3-7, the polymer concentration is kept constant, and the spacing can only be adjusted by < 47 nm. By altering the polymer concentration, which is shown in each row, inter-particle spacing can be adjusted by up to 80 nm, *i.e.* the smallest spacing is 56±11 nm while the largest spacing is 132±22 nm. When examining spin-coating speed as a function of polymer concentration, we

can also achieve a difference of up to 80 nm, from 50 nm to 130 nm, which is highlighted with the hash-marked shading in Figure 3-8. It is also interesting to note that inter-particle spacing varies linearly with the spin-coating speed. The calculated slope for the linear fit of each polymer concentration is 0.0050 ± 0.0007 nm/rpm (2 mg/mL), 0.0035 ± 0.0006 nm/rpm (3 mg/mL), 0.0030 ± 0.0005 nm/rpm (4 mg/mL). Therefore, linear interpolation can be used to determine the appropriate speed to produce the desired spacing.
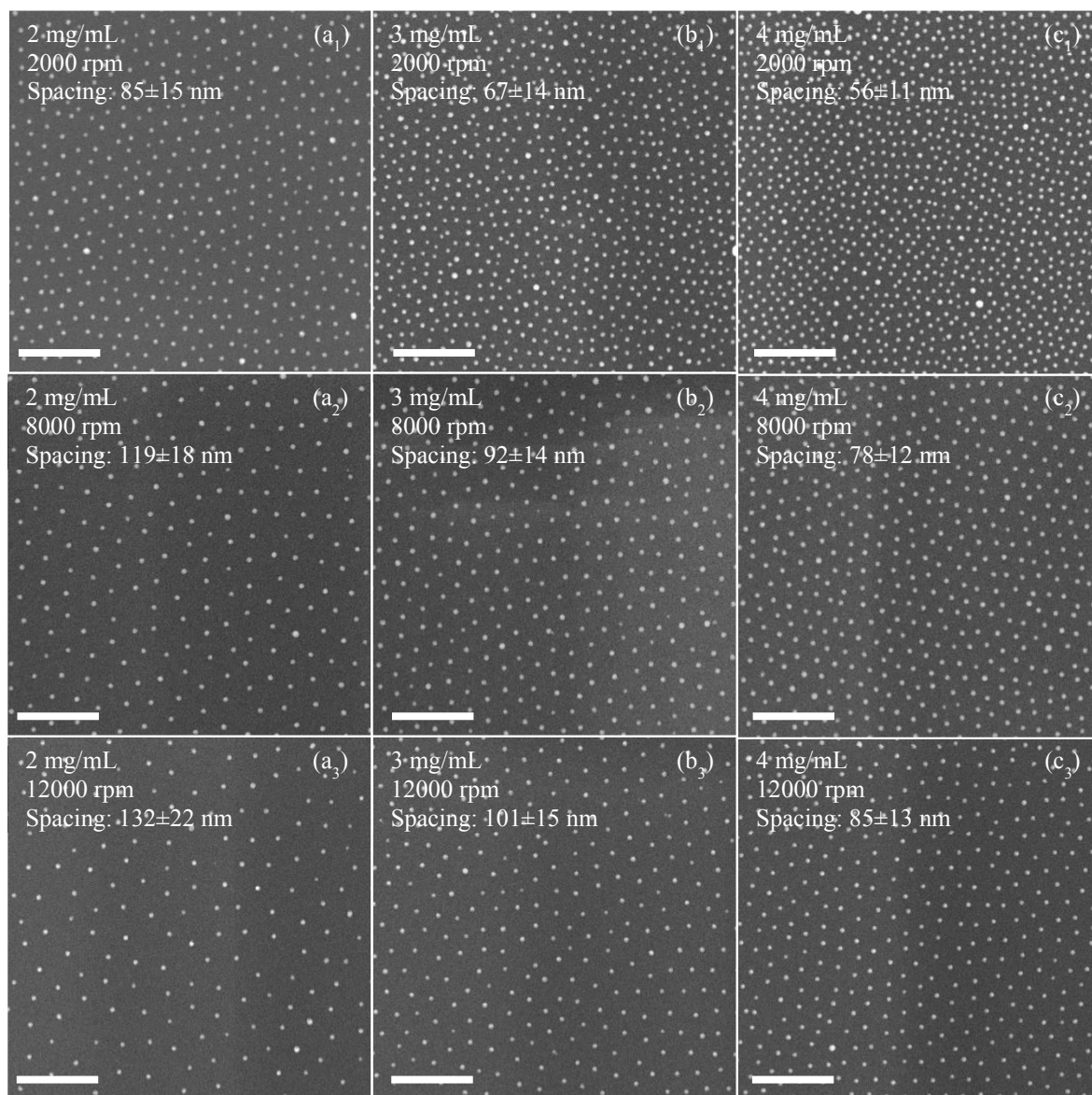
Figure 3-7: SEM images of Au nanoparticle array with inter-particle spacing tuned by polymer concentration (2 mg/mL, 3 mg/mL and 4 mg/mL, in rows) and the spin coating speed (2000 rpm, 8000 rpm and 12000 rpm, in columns). Scale bars: 300 nm.
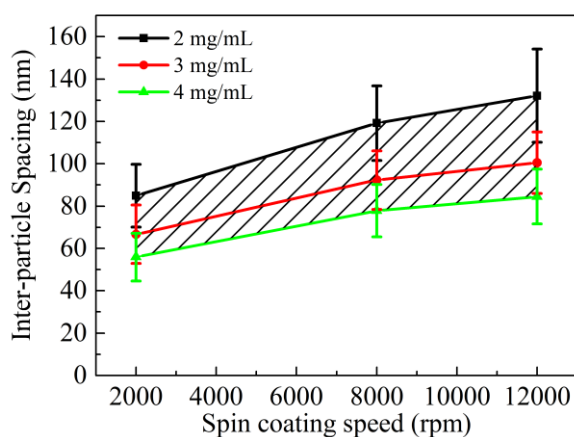
Figure 3-8: Influence of spin coating speeds and polymer concentration on inter-particle spacing. All of these three micellar solutions are synthesized using polymer 1056-*b*-671; and every data point is an average of all the inter-particle spacing in nine SEM images at random positions on the surface.

3.3.2   Polymer chain length

Polymer chain length is another parameter influencing nanoparticle spacing, which is shown in Figure 3-9. The longer the polymer chain lengths of blocks A and B, the larger the spacing will be between the nanoparticles. Table 3-1 summarizes the inter-particle spacing and hexagonal ordering index measured from SEM pictures. When the ordering index, which is defined in Section 2.4.1, is close to 1, the arrangement of nanoparticles is a perfect hexagonal order. As reported by Förster [146], the theoretical diameter of the micelles is

$$R \sim (N_{P2VP} + N_{PS})^{\delta} \qquad \text{(Equation 3-2)}$$

where δ is 2/3 (crew cut micelle), which is also listed in Table 3-1 for comparison. The results of the observed spacing is consistent with this relation; however, as evident in the SEM images in Figure 3-9 (a), the 154-*b*-33 polymer results in extremely small Au nanoparticles due to the short block chain lengths. Thus, the ordering index cannot be calculated, rendering this polymer unsuitable for use as an etching mask for nanopillar arrays.

45
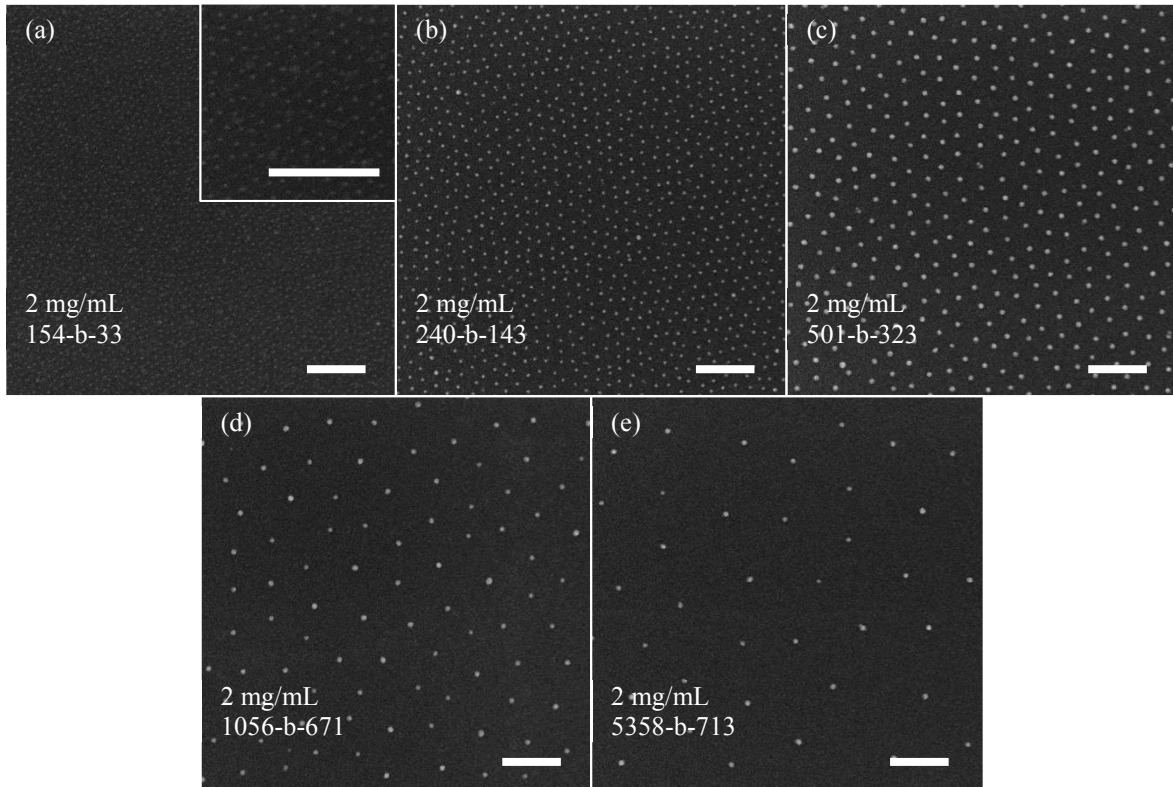
Figure 3-9: SEM images of Au nanoparticles prepared with polymers that have different chain lengths with the same polymer concentration of 2 mg/mL. Scale bars: 200 nm.

Table 3-1: Au nanoparticle spacing adjusted by varying the polymer chain length. Polymer concentration and the spin-coating speed are kept constant at 2 mg/mL and 6000 rpm. The mean inter-particle spacing, the ordering index and the theoretical diameter of the Au nanoparticle are summarized, respectively.

	Spacing (nm)	Ordering Index	$(N_{P2VP} + N_{PS})^\delta$ (nm)
154-*b*-33	~15	NA	1.6
240-*b*-143	50±8	0.57	5.4
501-*b*-323	85±13	0.60	9.4
1056-*b*-671	105±15	0.63	14.9
5358-*b*-713	165±25	0.53	10.3

Figure 3-10 shows a series of nanopillar arrays with varied inter-pillar spacings were successfully achieved, while maintaining the nanopillars' height at 300 nm, as seen from the cross section. The diameter of the nanopillar is slightly different, as higher density of ions and stronger ion bombardment occur at narrower positions during the RIE process. SEM images of the Au nanoparticle mask (inserts) indicate the corresponding inter-pillar spacing, *i.e.* approx. 55 nm, 65 nm, 85 nm, 100 nm and 130 nm, respectively.
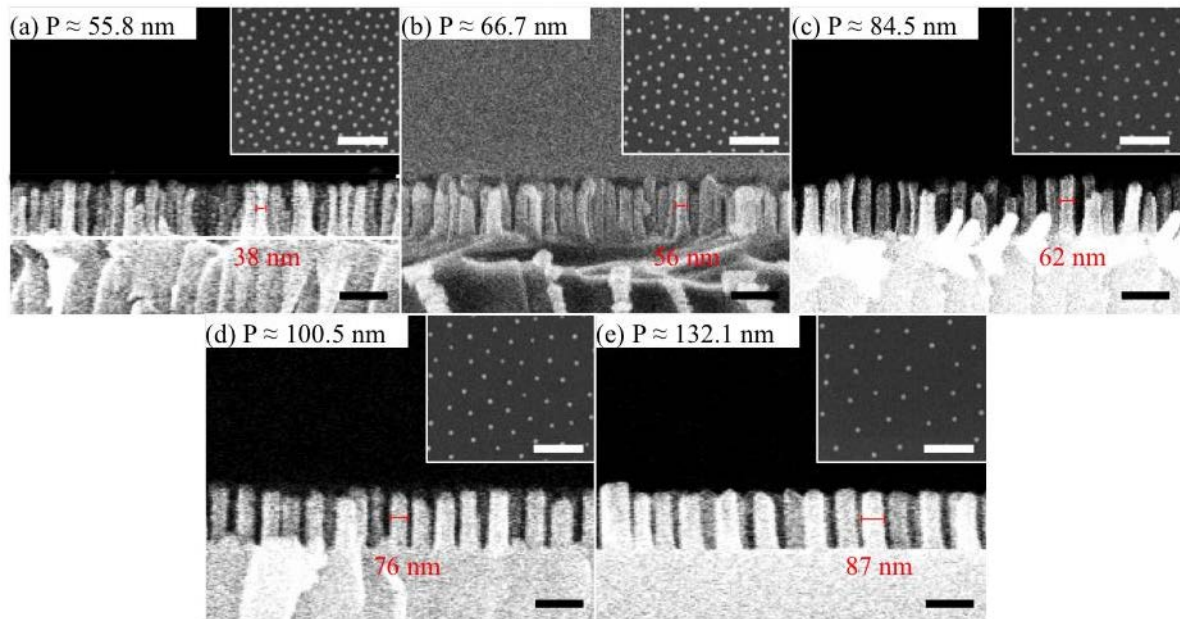
Figure 3-10: SEM images of cross sections of nanopillars with varied inter-pillar spacings: (a) 55.8±11.2 nm, (b) 66.7±13.9 nm, (c) 84.5±12.9 nm, (d) 100.5±14.5 nm and (e) 132.1±22.0 nm. Inserted images show the Au nanoparticle masks, which indicate the spacings of the nanopillars. The diameters of the pillars are indicated in the images. Notice that pillar heights and the Au diameters are kept constant, which are 300 nm and 9.5 nm respectively. Scale bars: 200 nm.

3.4   Fabrication of nanopillar arrays on other inorganic substrates

Nanopillar arrays are useful in various optical applications due to their excellent anti-reflective (AR) and potential lotus-effect properties; therefore, we studied the production process on a variety of other substrates (summarized in Appendix (Table 6-1). Parts of the samples prepared in this section were in collaboration with Prof. Brunner's group at the Ernst-Abbe-Hochschule Jena.
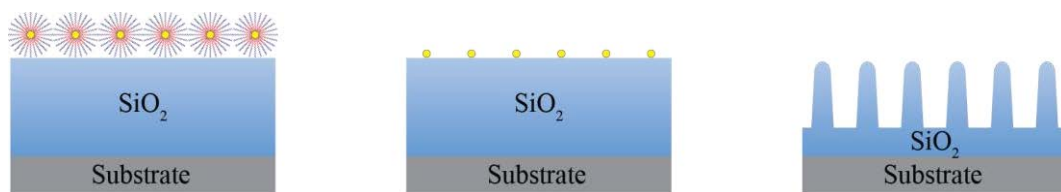
Figure 3-11: Sketch of preparation of SiO_2 nanopillar on different substrates with a sputtered SiO_2 layer via BCML and RIE technique.

The examination of RIE parameters for each type of material as studied for Suprasil[®] substrates is out of the scope of this thesis. Therefore, we utilized our optimized etching recipe for SiO_2 on new substrates modified with an additional layer of SiO_2, which is shown in Figure 3-11. For AR applications, only a substrate with a refractive index higher than SiO_2 (n=1.46) is useful to be sputtered with a SiO_2 layer because the sputtered SiO_2 reduces part of the reflective properties. After preparation of nanopillars on the sputtered SiO_2, the reflec-

tion loss from the SiO_2/air interface can be reduced, which results in a dramatic increase in the overall transmittance of the substrate.

3.4.1 Sputtering of SiO_2 layer

Physical sputtering of a SiO_2 layer was employed and performed by Mr. Reinhart Volker from the Central Scientific Facility Thin Film Laboratory (CSF Thin Films, Max Planck Institute for Intelligent Systems). It was conducted under an ultra-high vacuum (UHV) system with a SiO_2 target (3.00″ Dia. × 0.125″ Thick, 99.995%, Kurt J. Lesker Company, Germany) that was connected with a copper base for better cooling. The process begins at a base pressure of 10^{-6} mbar and the working pressure was kept at 2×10^{-3} mbar in O_2 and Ar atmosphere. Substrates were ground in the chamber and were sputtered at room temperature with 150 W RF power. A profiler (Dektak$^®$ 8, Advanced Development Profiler, Veeco Instruments Inc., USA) was used to measure the thickness of the sputtered thin film.

3.4.2 Cover slip substrate

Glass cover slips are made of borosilicate glass that contains SiO_2, B, Na, Ca and son on. Coverslips have a very low thermal expansion coefficient (3.3×10^{-6} K^{-1}) and good optical properties. The Abbe number is ~65 and refractive index is between 1.51-1.54. Due to its excellent thermal stability, this material is widely used in many biological, clinical and optical applications. Especially, for fluorescence studies, the transmittance property is extremely crucial to improve the weak fluoresecnt light quality [150].
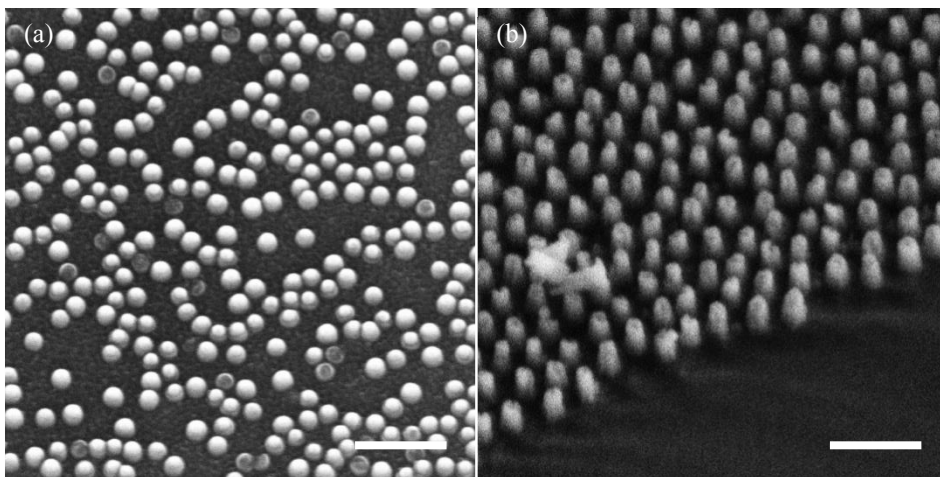
Figure 3-12: SEM images (tilted 20°) of nanopillar preparation on cover slip substrates without (a) and with (b) sputtered SiO_2 layer. The sputtered SiO_2 layer is measured as approx. 300 nm. The prepared nanopillars are approx. 200 nm in height (4 RIE cycles). Both of the samples are treated with the same cycles of RIE process (4 cycles). Scale bars: 300 nm.

Figure 3-12 shows the surface of cover slip substrates after nanopilllar preparation with and without a sputtered SiO_2 layer. In Figure 3-12 (a) the cover slip substrate can only be etched up to 50 nm (4 cycles of RIE process) because of the formation of an impeding layer caused by its impurities [134]. We also find that some of the short nanopillars (nanospheres) are cut

open from the top, indicating that the etching process can only etch away the top of the pillars and does not progress further into the substrate. By sputtering a layer of SiO_2, the nanopillars are well formed and the height is comparable to the pillars prepared on the Suprasil® substrate, as shown in Figure 3-12 (b).

3.4.3 Sapphire substrate

Sapphire also called alumina (Al_2O_3) is the second hardest and stable material preceded only by diamond ($n_{sapphire}$ =1.78 [151]). Also due to its good thermal stability and low frictional coefficient, it is commonly used in scientific instruments (*e.g.* infrared optics), luxury products (*e.g.* watch bearings) as well as electronics (*e.g.* anti-scratch screens). However, in the visible light range, sapphire only has a transmittance around 87% [152]. Therefore, it is highly needed to improve the optical properties and nanopillar array fabrication on the surface is introduced.

Al_2O_3 is most commonly etched with Cl^- containing etchant gases [151,153], with a slow etching rate, while we use F^- containing gases (CHF_3, SF_6 and CF_4). Since the size of Au nanoparticles used here is only 9.5 nm, and Al_2O_3 substrates do not form a passivation layer to protect the sidewall, etching with fluorine gases becomes very difficult. The inset of Figure 3-13 (a) shows the sapphire surface (without a SiO_2 layer) originally covered by an Au nanoparticle mask array. After the RIE process is applied, the topography of the surface has no obvious change but only the Au nanoparticles are consumed completely (Figure 3-13 (a)). In Figure 3-13 (b), however, nanopillars are able to form after the surface is sputtered with a SiO_2 layer, with a height of 100 nm.
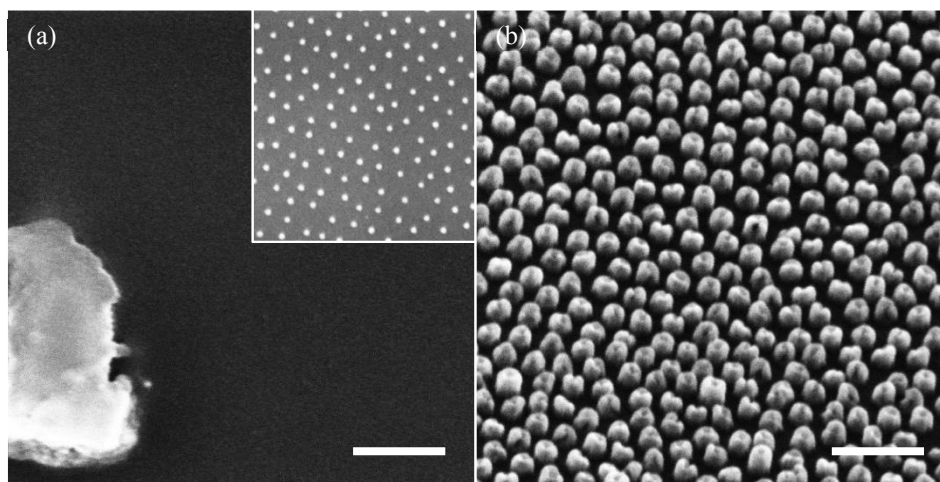
Figure 3-13: SEM images of sapphire substrates after RIE etching with (a) and without (b) sputtered SiO_2 layer. (a) The big bright impurity is dirt to show the surface is in focus under SEM, but the sapphire substrate is not etched and the Au nanoparticles are etched away. The insert is a SEM image showing the Au nanoparticles pattern on sapphire substrate surface before the RIE. (b) The nanopillar array is fabricated on the sputtered SiO_2 with the height of approx. 100 nm. The sputtered SiO_2 layer is measured as approx. 200 nm in height. Tilted angle: 20°. Scale bars: 300 nm.

3.4.4 Stainless steel substrate

Electrowetting is an interesting phenomenon in both biological and chemical applications [154]. To achieve controllable electrowetting, surface properties are critical, especially the hydrophilicity and hyphobicity. From the methods section in Chapter 2, we already know that the nanopillar surface can be silanized with FDTS. In order to control the wettability by applying an electrical potential, the substrate has to be conductive, thus stainless steel substrates were selected. These experiments were performed in collaboration with Prof. Brunner's group at the Ernst-Abbe-Hochschule Jena. After their group selected and polished the substrate, I sputtered SiO_2 on top and prepare the nanopillar array as previously described. In Figure 3-14, SEM images of the top-view (a) and tilted-view (b) of the nanopillar array are presented. Prof. Brunner's group has shown that the wetting of the water droplet can be controlled electrically on the nanopillar-covered stainless steel substrate, and that the hydrophobic surface enhances the bouncing of the droplets (data not shown).
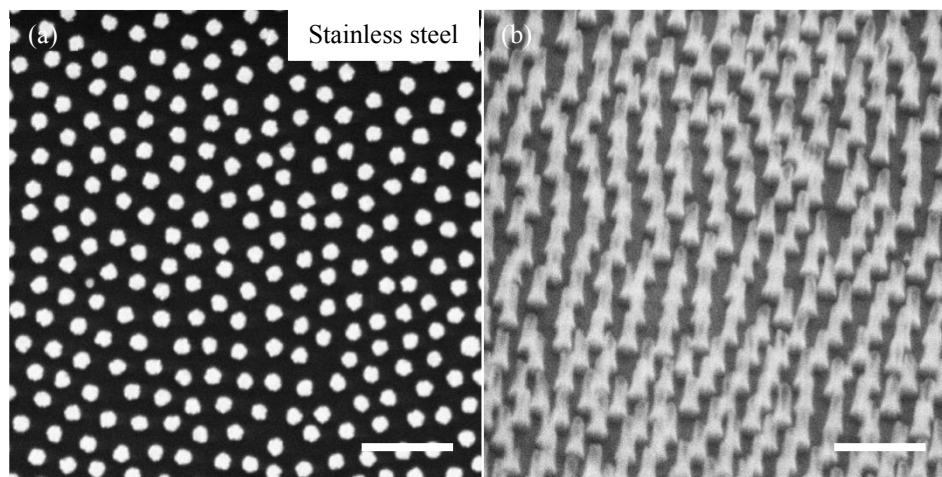
Figure 3-14: (a) Top view of the nanopillar array with the height of approx. 165 nm is prepared on a 300 nm-height sputtered SiO_2 layer on top of stainless steel substrate. (b) SEM image taken at a tilted angle of 45°. Scale bars: 300 nm.

3.4.5 SF10 substrate

SF10 is a dense flint optical lens material, which is often made into concave lenses as an achromatic lens together with crown glass [155]. In order to protect the lens surface from corrosion as well as to prepare the nanopillars on the surface, a gradient-index (GRIN) layer is deposited on the surface. This GRIN layer consists of a SiN_x layer, a SiN_x and SiO_2 transition layer, and a 200 nm SiO_2 layer (substrate was prepared by Prof. Brunner's group at the Ernst-Abbe-Hochschule Jena). Nanopillar arrays were fabricated on the top of this layer as previously described. The SEM images in Figure 3-15 show that 200 nm high nanopillars are prepared on the surface.
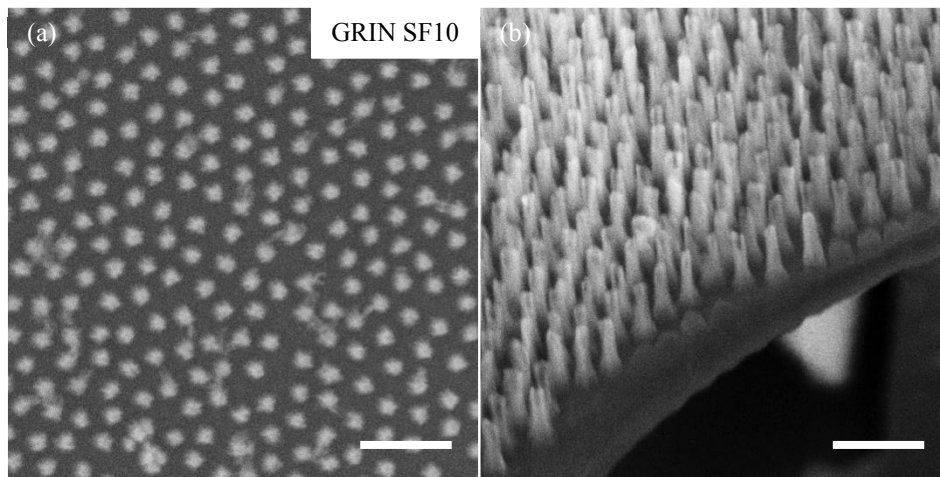
Figure 3-15: (a) Top view and (b) 20° tilted view of the prepared nanopillar under SEM. The height is approx. 200 nm on top of approx. 200 nm intermediate SiO_2 layer. Scale bars: 300 nm.

3.5   Discussion

3.5.1   Comparison of Suprasil® substrate and other substrates

Suprasil® is a high purity synthetic UV-grade fused silica material. It has excellent optical properties in the deep UV and visible wavelength range. This material is highly recommended for the high-aspect ratio nanopillar preparation [40,66,74] due to the following three major reasons.

Firstly, pillars with dimension in the nanometer scale range possess outstanding AR properties in the UV light range. It needs a substrate with excellent transparent property in the UV range. Compared with the normal optical glasses, *e.g.* BK7 (borosilicate crown glass) and fused silica, the reference sample of Suprasil® shown in Figure 4-6 has a transmittance of 90% at the wavelength of 200 nm. At the same wavelength, the light was completely absorbed by BK7 glass and the fused silica only has 10% transmittance [156].

Secondly, hardness, thermal expansion coefficient (CTE) and UV transparency are three critical properties of the material for a master stamp [51]. Hardness determines the lifetime and wearability of the mold, CTE significantly influences the demolding process and may cause structure distortions if the dimension mismatch occurs [157,158] and the transparency becomes essential when the UV nanoimprinting lithography is applied. Compared with the common used silicon stamp with a hardness of 7 Mohs and CTE of 2.6×10^{-6} K^{-1}, Suprasil® substrate has a comparable hardness of 6.5 Mohs and lower thermal expansion coefficient of 5.8×10^{-7} K^{-1}. Moreover, the transparency of the Suprasil® offers more choices of the nanoimprinting approaches.

The most important reason is about the processibility. In normal glasses, impurities are normally added to lower the melting point. During RIE, these compounds often form non-volatile elements, thereby slowing down or blocking the etching process. Taking BK7 as an

example, it contains 15% of non-volatile impurities including BaO, K_2O and Na_2O and the etching rate was found to be only 10 nm/min. [134]. Due to the fact that Suprasil® is a highly pure fused silica that contains extremely low metal and inorganic impurities, the etching process is much easier and faster (etching rate: 44 nm/min), thereby creating nanostructures with higher aspect ratio.

3.5.2 Mechanism of the hierarchical nanopillar formation
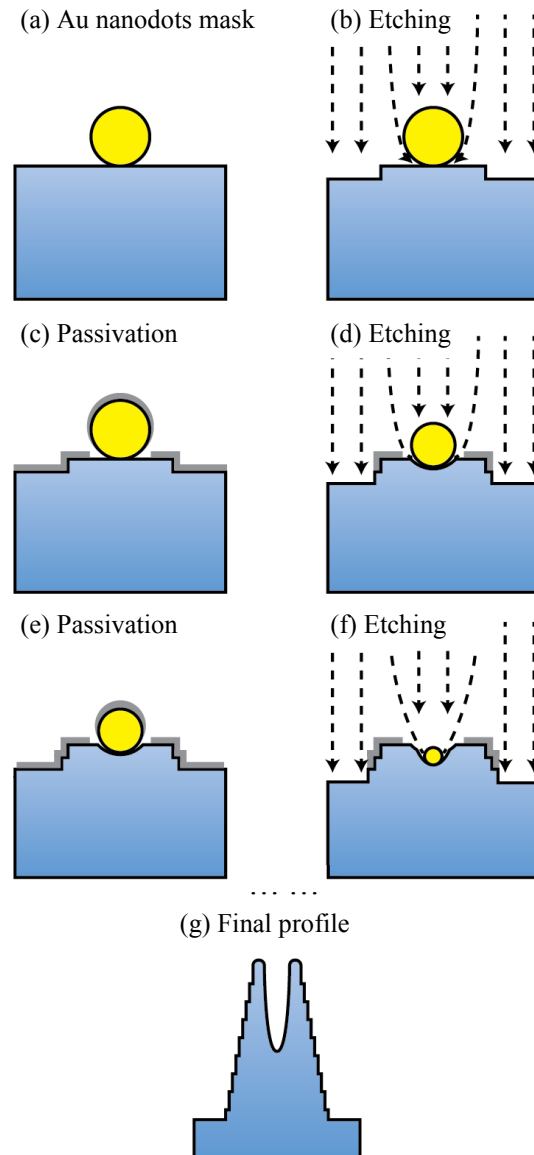
Figure 3-16: Schematic drawing of the nanopillar etching mechanism on silica substrate. (a) Au nanodots prepared by BCML technique serves as an etching mask. (b) The etching step uses SF_6 and Ar gases with RF. Because of the focusing of the ion beam by the Au dot, the etching rate underneath the Au nanodot is faster than the nearby region. (c) The passivation step using the gas CHF_3 forms a deposited layer of etching inhibitor (shown as the black layer). (d) The etching step etches the horizontal surface by ion bombardment, while the sidewall is protected by the passivation layer. (e) and (f) By alternatively repeating the etching and passivation processes, vertical nanopillars are formed; and at the same time, the Au nanodots were also eroded gradually, (g) thus the final profile of the nanopillar is achieved.

As seen in SEM images of nanopillar strucutures, *e.g.* Figure 3-4, Figure 3-12, Figure 3-13, Figure 3-14, Figure 3-15, a nanohole structure is observed in the center of the pillar top. Such hierarchical nanopillar structure is unique with our combined BCML and RIE technique. The formation mechanism of this hierarchical nanopillar is important to analyze the optical properties of the nanostructured surface and will also be beneficial for further development of RIE recipes for a better nanopillar profile. Therefore, the formation mechanism of the hierarchical nanopillar is discussed below.

Figure 3-16 depicts the developed RIE recipe on the Suprasil® substrate. A combination of two gases was utilized alternatively to achieve a high aspect ratio of nanopillars on the SiO_2 substrates: SF_6 and Ar for etching (b, d, f) and CHF_3 and Ar for passivation (c, e). Due to its intensive physical bombardment, Ar was used in both steps to enhance the chemical etching process. Radio frequency (RF: 13.56 MHz) was applied in both steps to generate ionic species and chemical reactive species (neutrals/free radicals). In order to increase the density of the plasma, the inductively coupled plasma (ICP) was introduced in the second step to enhance the isotropic fluoropolymer passivation.

During the SF_6 etching step, active F-containing neutral radicals etch the substrate by diffusion [159] and the charged ions were accelerated directionally towards the substrate surface (b, d, f). Due to the existence of metallic Au nanoparticle on the surface, the active radicals were strongly deflected [65,72]. The area around the particle was rarely sputtered and etched; thereby the passivation layer produced during the process could stay there for a longer time. During the CHF_3 passivation step, SiO_xF_y and fluorocarbons (c, e) were readily formed, which protected the sidewalls of the nanopillars [160]. By alternatively applying these two processes, the passivation layer gradually built up along the sidewall, thereby resulting in nanopillars with high aspect ratio (nearly vertical sidewalls, ~80º). Concurrently, the Au nanoparticle mask was gradually eroded. Therefore, the nanohole formed in the top center where the Au nanoparticle was previously located on the surface (g). When the diameter of the Au nanoparticle is 9.28±1.4 nm, the depth of the nanohole in the center is up to one third of the pillar height varying with the etching cycles from 1 cycle to 7 cycles. As the RIE cycle is further added, the nanohole will gradually shorten until disappear and the nanopillar will become longer and sharper. Therefore, the anti-reflective property will extend to long-wavelength, *i.e.* infrared light, which is not included in this thesis.

3.5.3   Summary of the achievable range of nanopillar dimensions

In summary, two important parameters of the nanopillar array, *i.e.* the height and inter-spacing are systematically investigated in this chapter. The nanopillar height is significant influenced by the RIE cycles and slightly influenced by the Au nanoparticle diameter that can be adjusted by the polymer chain length when the loading rate is fixed. The inter-pillar spacing is influenced by the polymer chain length, polymer concentration and spin coating speed, which is summarized in the functions below:

$Height = f_1(polymer\ chain\ length, RIE\ cycle, loading\ rate),$

Spacing $= f_2$ (polymer chain length, polymer concentration, spin coating speed).

As the polymer chain length is a variable in both functions, if the height and the spacing need to be adjusted independently, then the polymer chain length should always be kept constant. Hence, taking the polymer of 1056-*b*-671 as an example, which is also the most commonly-used polymer in this thesis, the height of the nanopillar in principle can be varied from several nanometers to micrometers range. However, as the height increases to higher than 400 nm, the antireflection property will gradually changing from visible light range to infrared light range, which is not the goal of this thesis. Therefore, the maximal height of the pillar adopted in this thesis is 400 nm that has already resulted in higher than 99% transmittance. The spacing of this polymer can be varied from 50 nm to 130 nm as shown in Figure 3-8. Larger inter-spacing is achievable by using longer-chain polymer. However, besides the interspacing, it will also cause the variation in the diameter and the height of the pillars. Therefore, 1056-*b*-671 polymer is mainly used in this thesis.

Chapter 4 Replication of nanostructures for improved anti-reflective properties

4.1 Overview

The preparation of nanostructures on organic polymeric materials is of great interest, as polymers exhibit many advantages such as biocompatibility, flexibility, low density and low cost compared to inorganic substrates. However, preparing nanopillar structures using the same method as for SiO_2 substrates is not possible due to fact that the H_2/Ar plasma treatment used to reduce Au nanoparticles severely damages polymer substrates, and the organic solvents and plasma bombardment during the RIE process corrodes the material. Instead, the replication of nanostructures into polymers from a glass mold is an indirect but promising approach to fabricate nanostructures without damaging the polymer surface.

As a non-destructive and cost-effective method, the nanoimprinting technology has become an increasingly popular technique to replicate micro- and nanostructures for both academic and industrial applications [48,52,161]. However, there still exist many challenges in this technique. Most importantly, fabricating master stamps is often complicatd and very expensive. This is especially true for a master stamp with nano-scale structures, in which costly and time-consuming electron-beam writing is often required [162]. To overcome this problem, the BCML technique introduced previously can be utilized to prepare stable and durable SiO_2 master stamps, which contain a large area array of nanostructures with adjustable parameters. The combination of BCML, RIE and a nanoimprinting technique could efficiently replicate large areas of nanostrucutres on different types of polymeric materials, as well as reduce the cost of the fabrication process. The nanostructures on the master stamp can be nanopillars with tunable parameters of 20-80 nm in pillar diameter and 50-250 nm in inter-pillar spacing.

Transparent polymers are used in numerous optical applications, such as cell phone lenses, the protection layer of electronic displays, glasses, intraocular lenses [163] and contact lenses due to their resilience, chemical stability, low density and low cost. However, compared with traditional optical materials such as silica, the major disadvantage of a relatively low optical transmittance severely hinders its application. For example, PMMA has a transmittance of approx. 90% at the wavelength range of 400 nm -1500 nm [164]. Nanostructures imprinted onto polymeric materials developed in this thesis work as a gradient layer for an anti-reflection effect, which can largely improve the optical transmittance of the material. As illustrated in Figure 1-4, the nanopillar and nanohole array serve as an intermediate layer with sub-wavelength structures in between two materials with different refractive indices. The

cross-sectional area, *i.e.* the effective refractive index, in this layer changes gradually; thus, the nanostructures work as an effective anti-reflection layer. The mechanism of moth-eye structures is discussed in detail in Section 4.7.4.

In experiments, the fabrication of large areas of uniform nanostructures poses a great challenge. In previous studies, nanostructures were fabricated by imprinting with the natural structures on the moth eye or cicada wings [165,166]. However, replication using natural structures suffers from the inability to tune parameters, poor reproducibility and the mold is not reusable. Other nanofabrication methods, such as e-beam lithography [167] have also been applied to create nanostructures, but they exhibit common disadvantages such as small area, low speed and high cost. Our group first reported using the BCML technique to fabricate large areas of nanopillar arrays on SiO_2 surfaces exhibiting anti-reflection properties in deep-UV range [75].

In this chapter, the previously described method is expanded upon in two respects. First, a systematic study was carried out in order to better understand how the dimensions of the nanopillars, *e.g.* the height and the inter-pillar spacing, influence the anti-reflective property. Second, the fabrication of nanopillar and nanohole arrays on polymeric materials was studied in detail. The limitations of two molding methods were first introduced, followed by the results of structure replication via nanoimprinting. A combination of BCML, RIE and nanoimprinting was used to replicate the anti-reflective structures onto polymer substrates. The transmittance of Suprasil® and two kinds of polymers, *i.e.* IPS® and PMMA, with single- or double-sided imprinted nanostructures was measured and compared. The angle-dependent anti-reflection was also studied. Table 4-1 summarizes the samples used for the anti-reflection study in this chapter.

Table 4-1: Summary of the samples for anti-reflection study.

Section	Material	Nanostructure	Side	Height (nm)	Inter-spacing (nm)
4.3	Suprasil®	nanopillar	single	50, 100, 200, 300, 400	55, 65, 85, 100, 130
4.4	IPS®	nanohole	single	50, 100, 200,300, 400	100
			double	100, 200	100
		nanopillar	single	50, 200	100
4.5	PMMA	nanopillar	single	300	100
			double	300, 400	100
		nanohole	double	400	100

4.2   Replication of nanostructures

4.2.1   Anti-adhesive layer deposition

To replicate the nanopillar structures on Suprasil® molds, either using the replica molding approach or the nanoimprinting technique, it is required to modify the mold surface and de-

crease the surface energy for better demolding. Therefore, a hydrophobic silane of FDTS was selected and deposited onto the surface.

Table 4-2 shows Suprasil® surfaces with nanopillars of approx. 300 nm height and 100 nm inter-pillar spacing exhibit a very small contact angle of < 5°. This superhydrophilicity is consistent with previous reports [74], and is likely due to the hydroxylation of the SiO_xF_y complex [168,169]. With enhanced surface area as well as hyrdroxylated –OH groups, the surface energy is so high that it causes strong adhesion of the master mold to the imprinted surface, leading to surface damage and structure distortion problems. After vapor deposition of the FDTS-silane, the contact angle of the same surface dramatically increases to 150°±0.7°, indicating that the surface modification of FDTS-silane successfully converts a hydrophilic surface to a superhydrophobic one, and thus lowers the surface energy.

Table 4-2: Contact angle measurement of the Suprasil® substrates before and after FDTS silane modification.

	Cleaned plain substrate	Nanopillar surface without FDTS silane	Nanopillar surface with FDTS silane
Pillar height (nm)	-	300	300
Contact angle (º)	15°±0.4°	<5°	150°±0.7°

The contact angle of surfaces with different nanopillar heights was also measured. Figure 4-1 shows the contact angles of the Suprasil® substrates after silanization with varied nanopillar heights, *i.e.* 0 (plain surface), 100, 200 and 300 nm. As seen from the figure, it is evident that the contact angle of the nanopillar-structured surfaces are around 50° higher than that of the plain surface, which is due to the large surface area enhancement with the nanostructures on the surface. Moreover, it shows that the contact angle is almost constant around 150°, independent of nanopillar height from 100 to 300 nm; thus the surface energy is low enough for imprinting. The silanized coating serves as an anti-adhesive layer, making the demolding of the nanopillar structures easier.
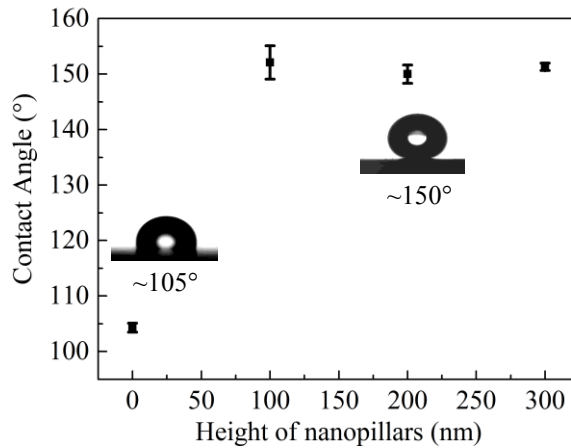
Figure 4-1: Contact angle of the Suprasil® surface with different nanopillar heights after FDTS-silanization. The contact angle is independent of pillar heights up to 300 nm.

4.2.2 Replica molding

Pressure molding

One method used to replicate the nanostructures is termed "pressure molding", and illustrated as a sketch in Figure 4-2 (a). This process first involves covering the Suprasil® mold with a PDMS monomer mixture (base to curing agent ratio 10:1) and subsequently degassing. By tightening the screws between the top metal plate and the bottom one, mechanical force is applied to the polymer-mold. PDMS is then cured with heat in such a pressurized state, and after curing, the thin film is carefully peeled off from the top.
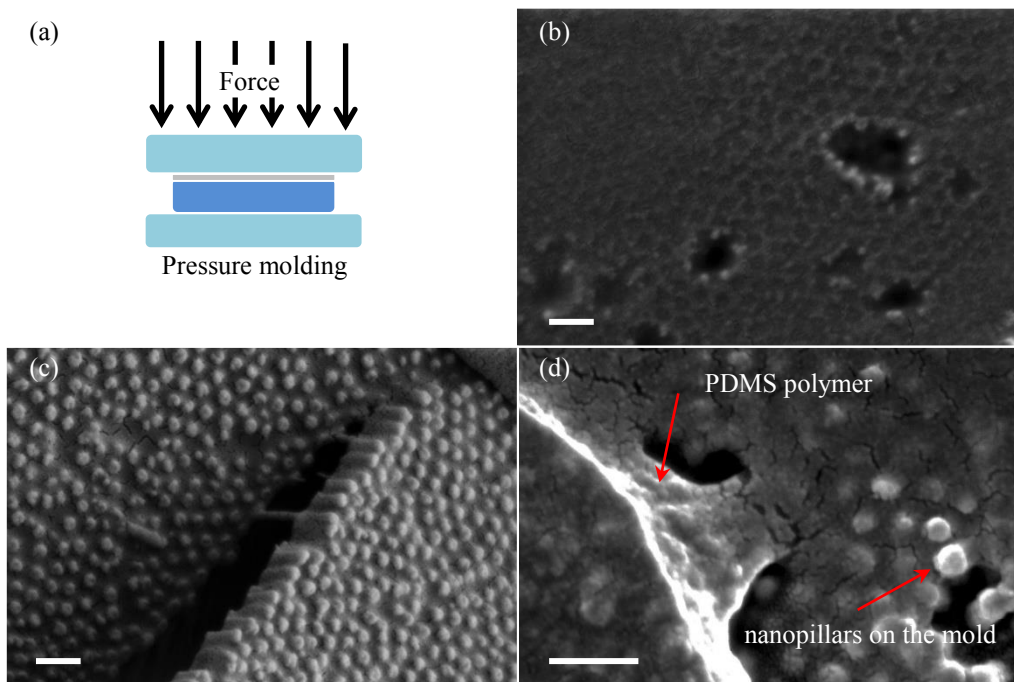
Figure 4-2: Pressure molding of PDMS on the nanopillar surface with pillar height of approx. 200 nm. (a) A schematic drawing of the method, (b) Peeled PDMS surface with shallow nanoholes, (c) The residual polymer on the nanopillar surface and (d) The polymer broken during the peel-off process and polymer leaves among the nanopillars. Scale bars: 200 nm.

Figure 4-2 (b) shows a piece of partially peeled-off film that has very shallow nanohole structures and also some nano- to micro-range defects. These defects might be caused by small gas bubbles stuck among the nanostructures due to insufficient degasing performed at a pressure of 10^{-1} mbar. Another challenge is that the mechanical force is difficult to control and the brittle Suprasil® substrate is very often broken. Moreover, the polymer film covered on the nanopillar surface after pressure casting is too thin to be completely peeled off and it is easily torn into small pieces, as shown in Figure 4-2 (d). Figure 4-2 (c) shows that the space among nanopillars is mainly filled by cured polymer, although the top layer of the polymer is peeled off with shallow nanoholes. The master mold cannot be reused for a second imprinting process due to these residual polymers. To solve the problem of the residual polymer remaining on the nanopillars, another molding method termed "vacuum molding" is used.

Vacuum molding

To control the thickness of the two-component polymer viscous mixture, a customized sample holder was designed, as shown in Figure 4-3. The master mold was fixed between an aluminium ring and a teflon basement. With this holder, additional polymer mixture can be scratched off from the surface before applying the vacuum; thus the thickness of the polymer film is limited to about 200 μm, which is thin enough to decrease the required vacuum pressure, but thick enough to be peeled off after curing. Furthermore, to solve the problem that the master mold is frequently broken, the force was applied via vacuum in this method without direct contact as discussed above in the "pressure molding" method.
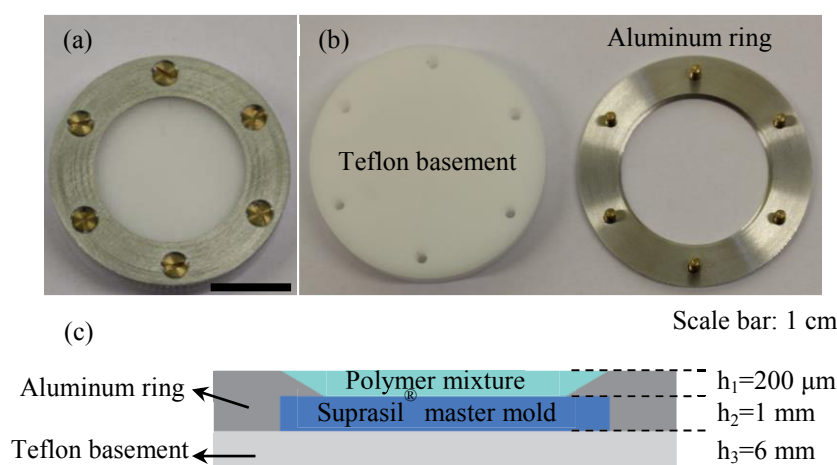
Figure 4-3: Customized sample holder for vacuum molding. (a) Pictures of the assembled holder and (b) The separated parts. (c) The schematic drawing represents the cross-section of the holder with important dimensions. With the holder, a 200 μm thin film of the polymer mixture is prepared on the master mold.

Figure 4-4 shows a polyurethane (PU, Biothan[®]) surface peeled from the master molds after the vacuum molding method. The mold was coated with a nanopillar array of 200 nm in height, 50 nm in diameter, 100 nm interspacing. The two-component PU was mixed and degased thoroughly. Then it was poured to the Suprasil[®] mold surface, which was already fixed in the sample holder. After scratching the extra PU mixture, the polymer was kept at room temperature for curing.

Figure 4-4 (c) shows a semi-hexagonal ordered nanohole pattern with spacing of approx. 100 nm that is consistent with the spacing of the master mold (Figure 4-4 (a)). The diameter of the nanoholes is approx. 30 nm on average, which is similar to the diameter of the nanopillar tip, but far from that of the nanopillar bottom, as shown in Figure 4-4 (b). This is a result of two processes. First, the surface replication is incomplete, and the nanoholes are shallower than the nanopillars on the mold because the polymer cannot fill to the bottom of the nanopillar array. Such phenomenon is more obvious in Figure 4-4 (d), in which the polymer shows even lower quality of the nanohole array. The replicated nanoholes on PU are inhomogeneous and a fraction is very shallow in depth with a small diameter. Second, the viscoelasticity of the polymer causes the shrinkage of the nanoholes after demolding. Cracks are also seen in

the images, as indicated by arrows in Figure 4-4 (d), likely due to the stress applied during the peeling-off process.
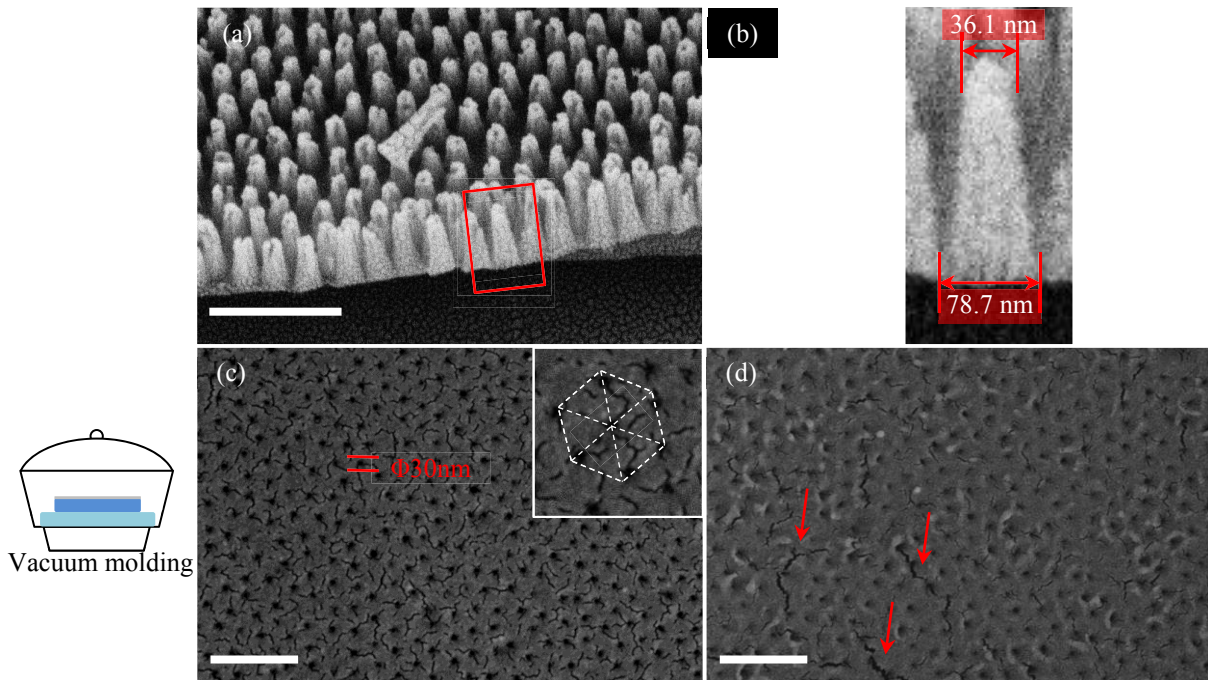
Figure 4-4: SEM morphology images of the Suprasil® mold and the replicated PU surface. (a) Master mold with a nanopillar height of 200 nm. (b) An enlarged image of one nanopillar, showing its slightly conical profile. (c) (d) Two random positions on the polymer surface. The diameters of the nanoholes are measured to be around 30 nm in diameter, and cracks (red arrows) can been visualized. Scale bars: 400 nm. The sketch on the left illustrates the vacuum molding method.

Table 4-3: Summary of the 2-component polymers used for pressure molding and vacuum molding.

Polymer	Nanopillar height	Pressure molding result	Vacuum molding result
PDMS	100 nm	negative	negative
PDMS	200 nm	negative	negative
PDMS	300 nm	negative	negative
MED6020	100 nm	-	negative
MED6020	200 nm	-	negative
MED6020	300 nm	-	negative
MED6215	100 nm	-	negative
Biothan® (PU)	200 nm	-	positive
Biothan® (PU)	300 nm	-	positive with defects

Table 4-3 summarizes the replication results of the polymers with the previously mentioned methods. From rheology and Young's modulus measurements, the difference in rheological

properties of the liquid polymer and mechanical properties is clear. The measured data are shown in Figure 4-5. The viscosity of the Biothan (PU) (Figure 4-5, left-hand side) is the lowest compared to the other two, which indicates that the Biothan[®] (PU) polymer mixture can relatively easily fill up the nano-scale inter-pillar spacing during the molding process. On the other hand, its modulus is the largest among all polymers, as seen in Figure 4-5 (right-hand side). Its high tensile modulus ensures it can sustain stronger peeling-off force with much less surface damage (cracks or tear-off). The rheology was measured by a rheometer (Kinexus Pro, Malven, UK) using a plate-to-plate (40 mm in diameter) geometry and the modulus was meaured by a tensile testing system (Nano Bionix Testing System, MTS, USA).
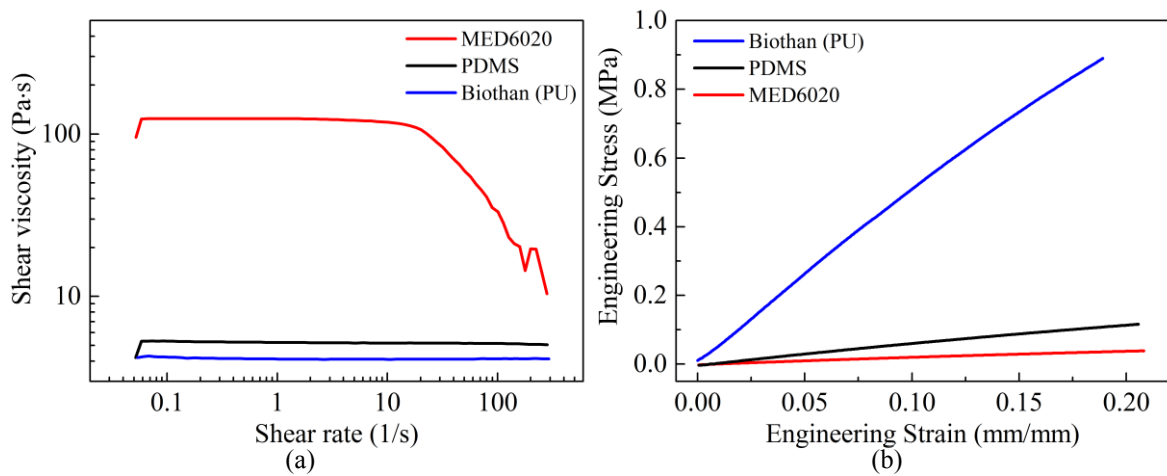
Figure 4-5: Viscosity and elasticity measurement of PDMS, MED6020 and Biothan[®] (PU). With the lowest viscosity and the highest Young's modulus, Biothan[®] (PU) performs the best among three polymers for the molding method.

4.2.3   Nanoimprinting

The vacuum molding method controls the film thickness and solves the problem of residual polymer sticking to the mold surface; however, it is still difficult to replicate the full profile of the nanopillars due to the limitation of the vacuum pressure (10^{-1} mbar). In order to improve the fidelity of the imprinted polymeric nanostructures with high aspect ratio, another approach named nanoimprinting, or hot embossing, is thus applied. The imprinted polymeric nanostructures and the AR properties of the molds and polymers are discussed in Section from 4.3 to 4.5.

4.3   Anti-reflective properties of the Suprasil® mold

4.3.1   Influence of the nanopillar height

The height of the nanopillars can be well-controlled by adapting the RIE parameters, which has been discussed in detail in Chapter 3. For anti-reflection measurement, nanopillars with different heights were prepared on one side, *i.e.* 50 nm, 100 nm, 200 nm, 300 nm and 400 nm. Inter-pillar spacing was kept constant at 101±15 nm by using the same type of block copolymer, solution concentration and spin-coating speed. The reference sample was a plain

substrate cleaned with CARO. The samples were measured with a Cary 5000 in the wavelength range of 200 nm to 1500 nm, covering UV, visible, as well as near infrared range. The transmittance spectra were plotted in Figure 4-6.

Compared to the reference sample (Figure 4-6, black curve), there is a gradual enhancement in transmittance for pillars with different heights (colored curves) over the entire measured wavelength range. Among these samples, the highest transmittance of 96% is achieved at both 450 nm and 900 nm with the tallest pillar height of 400 nm. Compared with the control sample which exhibits a transmittance of only 92.8%, the sample with nanopillar array on one side provides approximately 3.2% improvement in transmittance. The absorption at the wavelength of 1390 nm is due to the OH groups contained in the Suprasil® substrate (< 1000 ppm) [170-172].
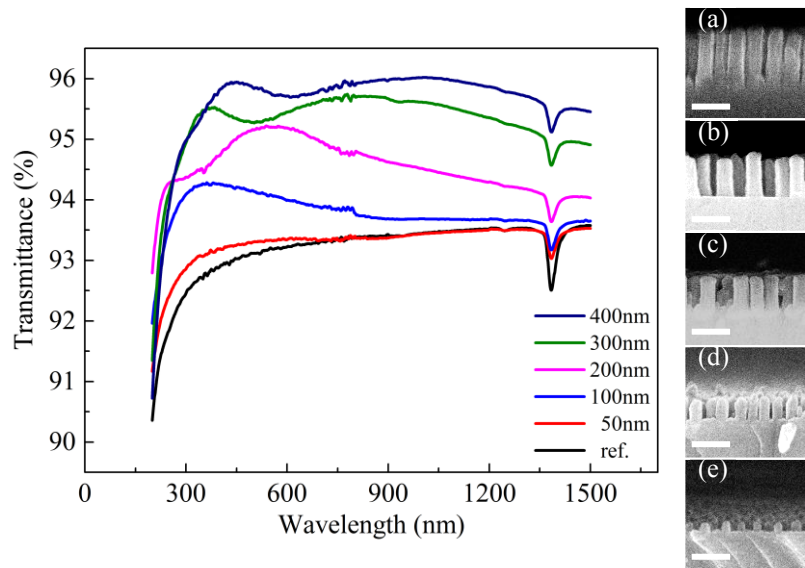
Figure 4-6: Transmittance measurement of the Suprasil® substrates with gradually increasing nanopillar heights from 50 nm to 400 nm, as shown in corresponding SEM images from (e) to (a). Scale bars: 200 nm. Au nanoparticle mask is prepared by BCML technique with spacing of approx. 100 nm and Au diameter of approx. 9.5 nm. The height of the nanopillars is controlled by using different RIE cycles.

It was also observed that the peak position of the highest transmittance depends on pillar height. 50 nm height nanopillars (Figure 4-6, red curve) exhibit an increase in transmittance by only a maximum of 0.3% for wavelengths below 700 nm compared with the control sample. With increasing the pillar height, the maximum transmittance is tuning towards larger wavelength range. The peak transmittance of 100 nm, 200 nm, 300 nm and 400 nm nanopillars are at 350 nm (Figure 4-6, blue curve), 580 nm (Figure 4-6, pink curve), 800 nm (Figure 4-6, green curve) and 950 nm (Figure 4-6, dark blue curve), respectively.

4.3.2 Influence of the inter-pillar spacing

Five different inter-pillar spacings, spanning from 55 nm to 130 nm, were prepared by gradually increasing the spin-coating speed of the deposited Au micellar solution. 130 nm is the

maximum spacing of polymer 1056-*b*-671, which was demonstrated previously (see Chapter 3 Figure 3-8). Polymers with higher molecular weight can achieve even larger inter-pillar spacing. However, the diameter of the Au nanoparticles is smaller, which can lead to shorter nanopillars. The same Au micellar solution was used to maintain the Au nanoparticle diameter of approx. 9.5 nm and to keep the nanopillar height constant.

Figure 4-7 illustrates the measured transmittance of each substrate with varied inter-pillar spacing of 55 nm to 130 nm. The reference sample, without nanopillars, is shown as the black curve in the figure. Nanopillar inter-spacing of 130 nm (Figure 4-7, red curve) demonstrates the lowest transmittance of the nanopillar samples in the wavelength range from 200 nm to 600 nm. Within this wavelength range, the transmittance is gradually increasing by decreasing nanopillar inter-spacing. The highest transmittance is observed on sample with 55 nm inter-pillar spacing. At the wavelengths greater than 600 nm, there is no obvious difference in transmittance observed. The samples with interspacing of 65 nm (Figure 4-7, green curve), 55 nm (Figure 4-7, dark-blue curve) and 85 nm (Figure 4-7, pink curve) have very close transmittance values.
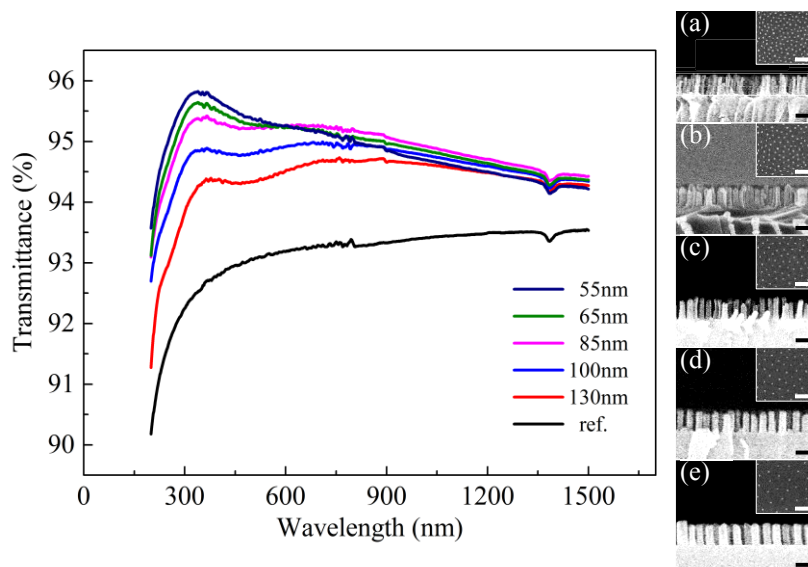
Figure 4-7: Transmittance measurement of the Suprasil® substrate with gradually increased inter-pillar spacing from 55 nm to 130 nm (represented in (a)-(e)) with the same nanopillar height of approx. 300 nm. This spacing range is obtained according to the results shown in Figure 3-8 by using the same polymer with Au diameter of 9.5 nm. Scale bars: 200 nm.

4.3.3   Angle dependent transmittance of Suprasil® substrates with nanopillar surfaces

One of the major advantages of the nanostructures for AR is the improved transmittance of the substrate in a wide range of incident angles. Angle dependent transmittance measurements were carried out with these samples to prove this advantage. The Suprasil® substrate with 400 nm high nanopillar (100 nm spacing) was investigated here compared with the reference sample comprising a planar surface. Both the transmittance and the reflectance were

measured from 10° to 60° incident angle by the Goniometer set-up that is introduced in section 2.4.3.

As shown in the measured spectra in Figure 4-8, the transmittance of the Suprasil® with nanopillars gradually decreases from 96% to about 90 %, as the incident angle increases from 10° to 60°. The same tendency is also observed for the referenced sample with a drop in the transmittance from 93% to 85%. However, comparing these two plots, a remarkble improvement of the transmittance is clearly shown at different incident angles. Even at the large incident angle of 60°, the transmittance is still above 90% and the reflectance is lower than 8% at the wavelength from 400 nm to 500 nm.
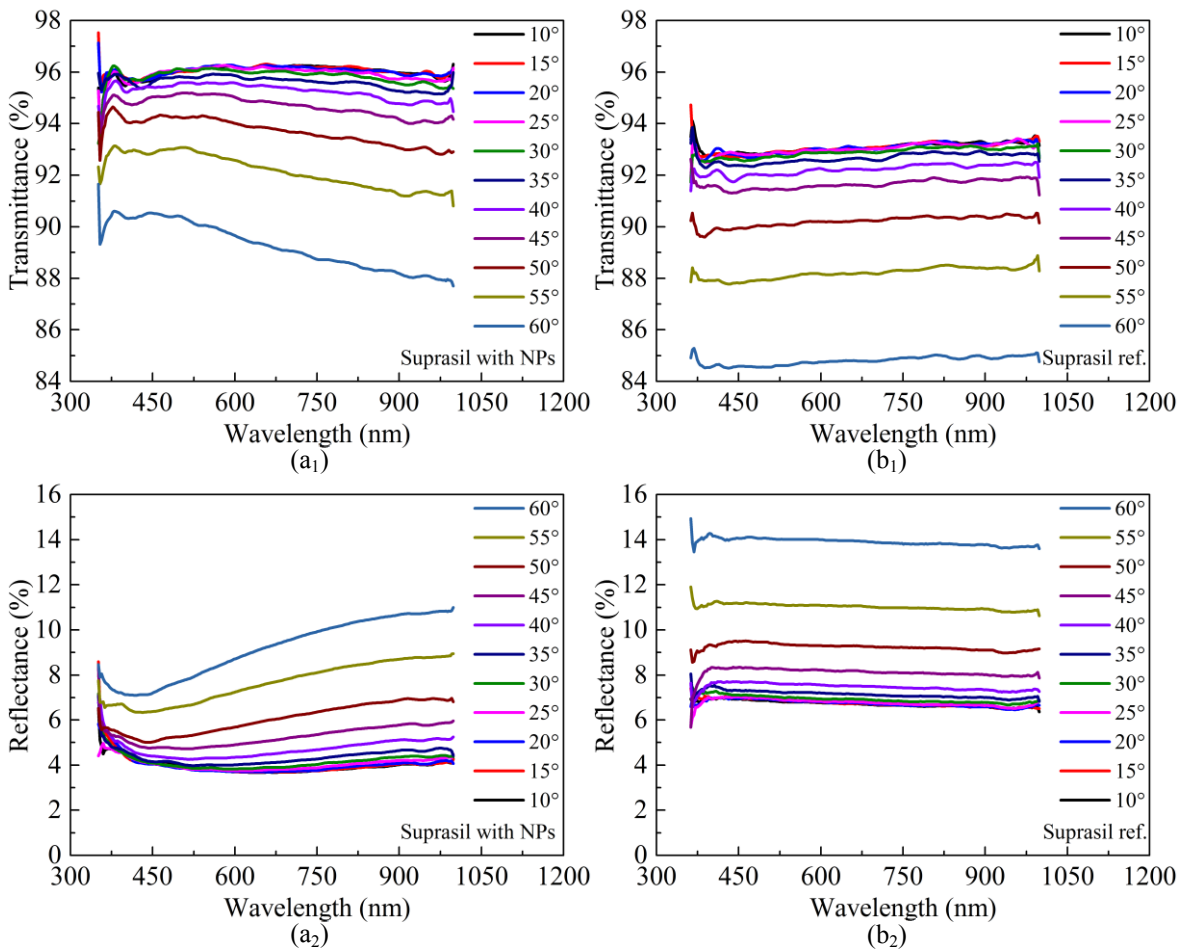
Figure 4-8: Incident angle dependent measurement of the transmittance and reflectance of Suprasil® substrates with and without nanopillar arrays. The nanopillar array is fabricated on only one surface of the substrate with a height of approx. 400 nm and an inter-spacing of approx. 100 nm. (a$_1$) and (a$_2$) are the spectrum of transmittance and reflectance measured on Suprasil® substrate with nanopillar prepared on one side. (b$_1$) and (b$_2$) are the spectrum measured on reference sample of Suprasil® substrate.

4.4 Anti-reflective properties of the IPS®

4.4.1 Anti-reflection of the IPS® with single-sided nanohole surface

The structure of the IPS® with single-sided nanohole surface

Two different aspect ratios of the Suprasil® master molds were prepared and used for nanoimprinting. The nanopillar arrays of those two molds are prepared by BCML and RIE, with only varying the RIE cycle time, *i.e.* 1 cycle for sample (a) and 6 cycles for sample (b). After silanization, a thermoplastic transparent polymer sheet, IPS®, was then placed on the surface of the molds. Under 40 bar and 165°C, the IPS® sheet changes to a viscous fluid state and flows to fill the inter-pillar spacing. Once the sample is cooled below the glass transition point (80°C), it reverses to the plastic state. Due to its hydrophobic surface and the silanized master mold's surface, the polymer sheet was easily removed from the mold, thereby preserving fine nanostructures.

Figure 4-9 shows the SEM measurement of both samples. Figure 4-9 (a_1) illustrates the nanopillar arrays with a height of approx. 50 nm, an inter-pillar spacing of approx. 100 nm and a diameter of approx. 35 nm. Figure 4-9 (a_2) shows the corresponding imprinted IPS® sheet surface with nanoholes. It reveals a very well-ordered semi-hexagonal arrangement with hole-diameters of approx. 35 nm and inter-hole spacings of approx. 100 nm, which are both consistent with the master mold. Figure 4-9 (b_1) shows the demolding process, in which a small piece of the mold surface was broken and left on the polymer surface as the polymer is lifted up from the master mold. This image clearly illustrates how the nanoimprinting works even with high aspect ratios and dense nanopillar arrays (65 nm in diameter, 300 nm in height and 100 nm in inter-pillar spacing). Figure 4-9 (b_2) shows ordered nanoholes with a diameter of approx. 70 nm and an inter-hole spacing of around 100 nm that also exactly replicates the mold. For optical applications, a well-defined nano-scale shape and the area of the uniformly structured surface are essential. Figure 4-10 is a SEM picture of a relatively large area of the IPS® surface, showing that the imprinted nanoholes are very homogenous in a large area. In fact, SEM observation shows that the whole sample area of 20 mm diameter contains uniform imprinted structures.
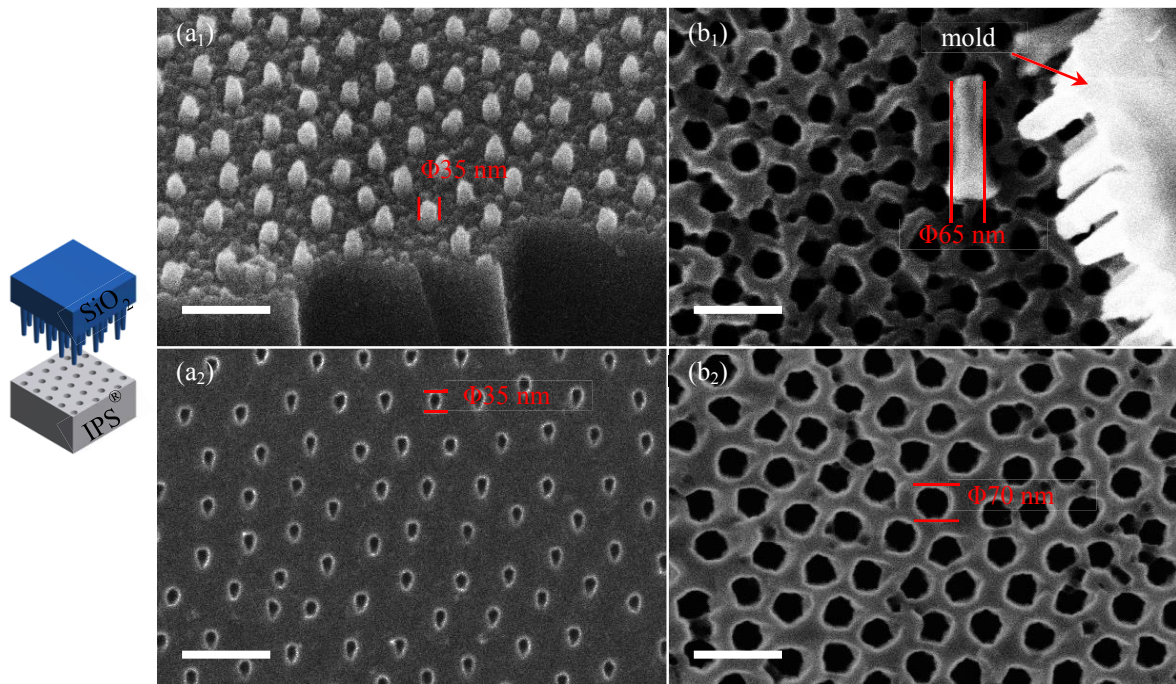
Figure 4-9: SEM images of master molds (a_1, arrow in b_1) with nanopillar heights of 50 nm (a_1) and 300 nm (b_1). (a_2) and (b_2) are the corresponding nanohole array imprinted on IPS® substrates. The inter-pillar spacings of both molds are 100 nm. The schematic drawing besides the SEM images shows that the one-side nanoimprinting method was used. Scale bars: 200 nm.
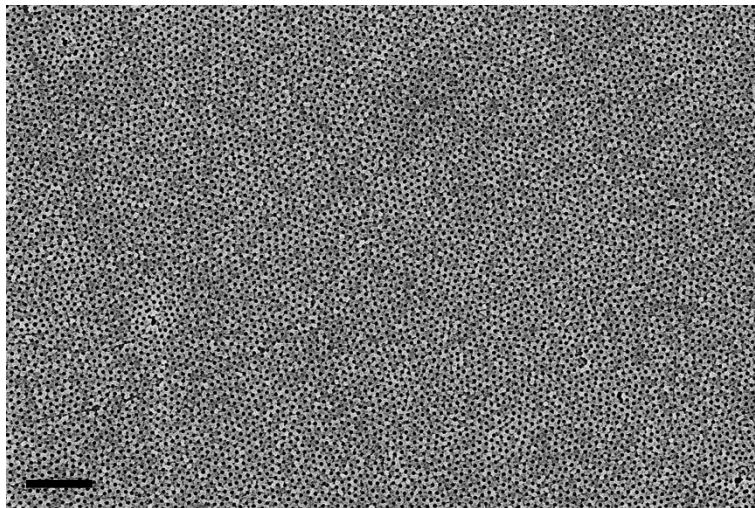
Figure 4-10: SEM image showing a large area of homogeneous nanoholes on IPS® surface replicated from a master mold with a pillar height of 300 nm, a diameter of 65 nm and an inter-pillar spacing of 100 nm. Scale bar: 1 μm.

Since the polymer is too soft to be cut for cross sectional viewing with SEM, and the nano-scale structure of nanoholes is too small to withstand the ultramicrotome, the depth of nano-holes is evaluated from the height of the related nanopillar (master mold). As an example, the SEM image in Figure 4-11 demonstrated that the IPS® polymer is filled to the bottom of the nanopillar-structured surface. It proves that the polymer reaches the bottom of the nanopillars. This sample was prepared prior to polymer sheet demolding and after breaking down the

middle in order to observe the cross section. The SEM image shows that the nanopillars on the master mold are approx. 300 nm high (red arrows) and the IPS® polymer (yellow arrows) is imprinted to the bottom of the nanopillar gaps. The master mold can be reused, and transmittance measurements of the imprinted polymers will be discussed in the next section.
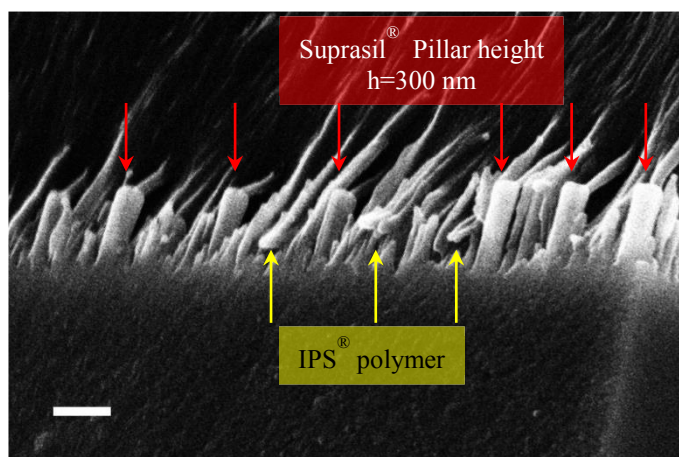
Figure 4-11: SEM image of IPS® polymer attached to Suprasil® master mold with nanopillar height of 300 nm. Sample was prepared without demolding the polymer from the surface, but breaking it in the middle to observe the cross section. It can be seen that the polymer is filled to the bottom of the pillar gaps (yellow arrows). Scale bar: 200 nm.

The transmittance of the IPS® with single-sided nanohole surface

The samples were prepared with a gradually changing height from 50 nm to 400 nm, and a reference sample without structures was also imprinted with a plain Suprasil® substrate. Their optical transmittance was measured and plotted in Figure 4-12.

The enhancement of transmittance in Figure 4-12 (a) and (b) is consistent between the master molds and the imprinted IPS® sheets. Both transmittances are gradually improved when the height/depth of the nanopillar/nanohole is increased up to 200 nm. The IPS® sheet with 200 nm-depth nanohole arrays shows a significant transmittance increment of approx. 3% compared with the IPS® reference sample as a plain surface. The transmittance reaches as high as 94% (at 800 nm wavelength), which is higher than a plain glass surface. If the reflection loss from the other interface is excluded, the transmittance of IPS® with nanopillar height of 200 nm can probably reach even higher up to 96% - 97%.

When the master molds have higher nanopillars, in other words the imprinted IPS® sheets have deeper nanoholes as shown in Figure 4-12 (c) and (d), the transmittance of the Suprasil® molds is improved further, reaching 95%. However, the transmittance of the imprinted IPS® does not show the same tendency as that of the corresponding master molds. The transmittances appear to be non-uniform. This two samples with large depth in Figure 4-12 (c) (d) alternatively show relatively higher transmittance. The sample with a 300 nm-depth nanohole array shows a valley that dramatically drops in transmittance at around 550 nm, while the sample with a 400 nm-depth nanohole array shows two drops at approx. 450 nm and 900 nm. At the range below 700 nm, the sample with a 400 nm-depth nanohole shows higher trans-

mittance than the sample with a 300 nm-depth nanohole. As the wavelength goes above 700 nm, it reverses.
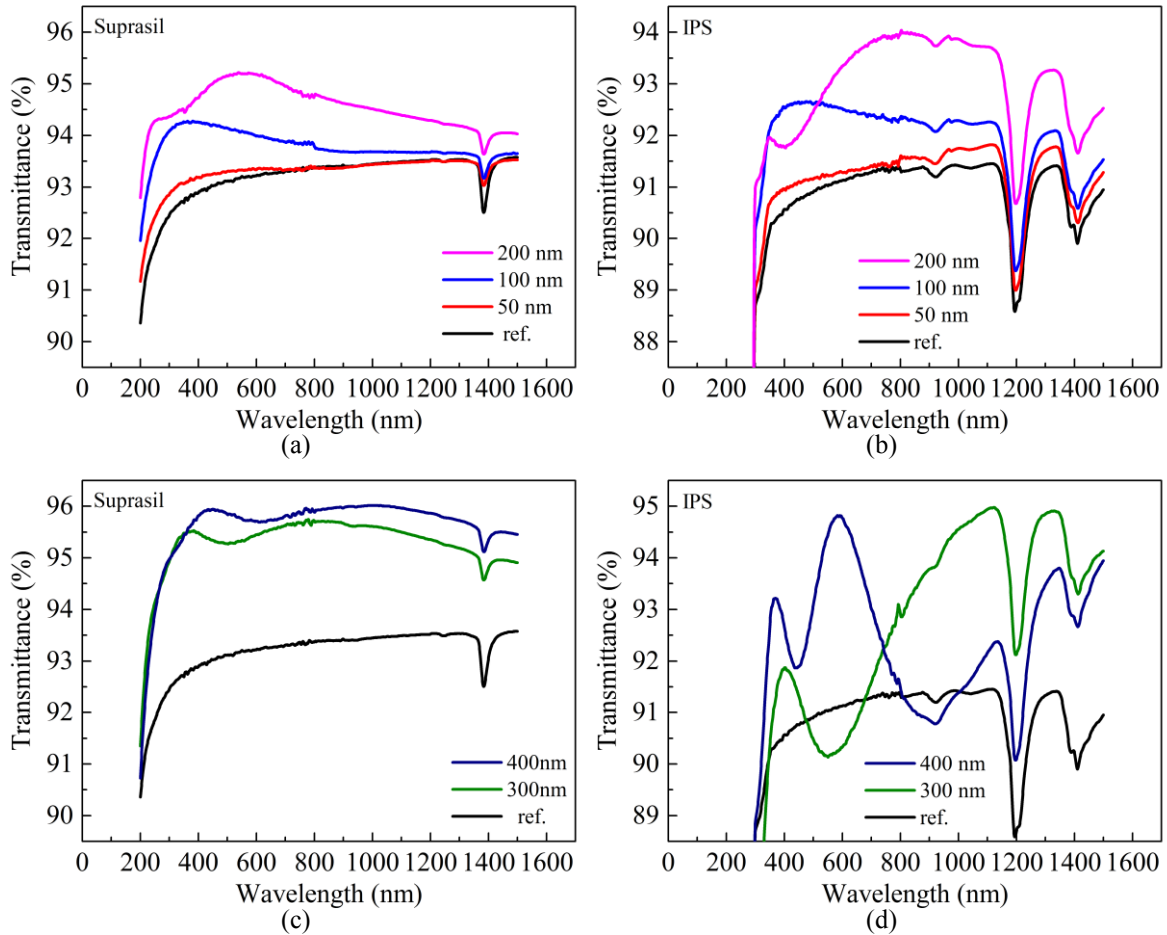
Figure 4-12: Transmittance of the Suprasil® molds ((a) and (c)) and the imprinted IPS® sheets ((b) and (d)) with gradually increased nanopillar height and corresponding increased nanohole depth, *i.e.* reference sample with plain surface (black curve), 50 nm (red curve), 100 nm (blue curve), 200 nm (pink curve), 300 nm (green curve) and 400 nm (dark blue curve). Inter-spacing of the nanostructures is kept constant at approx. 100 nm.

Repetitive use of the Suprasil® mold

For industrial applications, production of the master mold should be low-cost, thus, it is very important that the master mold is reusable and still able to produce imprinted polymers with high quality optical properties. To test the reusability of our master mold, one Suprasil® substrate with a 200 nm-height nanopillar array and 100 nm inter-pillar spacing was used for eight times to imprint different IPS® sheets without intermediate cleaning step. The transmittance of each imprinted IPS® sheet was then measured to check whether the improved transmittance is affected.

Figure 4-13 shows the eight transmittance measurements in the wavelength range between 200 nm and 1500 nm as a 3D plot and the inserted figure shows the zoom-in of the visible

wavelength range from 500 nm to 900 nm, as the transmittance increment is maximal in this range. Compared with the reference IPS[®] sheet without a nanohole array that has a transmittance of approx. 91%, the improved transmittance of the measured sheets is almost constant at approx. 94% (at 750 nm wavelength). The first and the last imprinted IPS[®] sheets were measured by SEM to check the surface morphology and the pictures are shown in Figure 4-14. This indicates the repeated use of the master mold does not affect the quality of the imprinted nanostructures and preserves the anti-reflection property. The nanopillar array on SiO_2 is stable under 40 bar pressure and 165°C temperature, and it can be repeatedly used at least eight times. Eight times is certainly not the limit for the reproducibility of the master mold; further tests can be carried out in the future. It is also worthwhile to mention that each IPS[®] sheet imprinted from the SiO_2 mold can be further used to imprint PMMA samples as discussed in Section 4.5, and the product of the Suprasil[®] mold life cycles and the IPS[®] mold life cycles is the number of samples that can be produced by a single master mold, which can be conservatively estimated to be over 100 pieces.
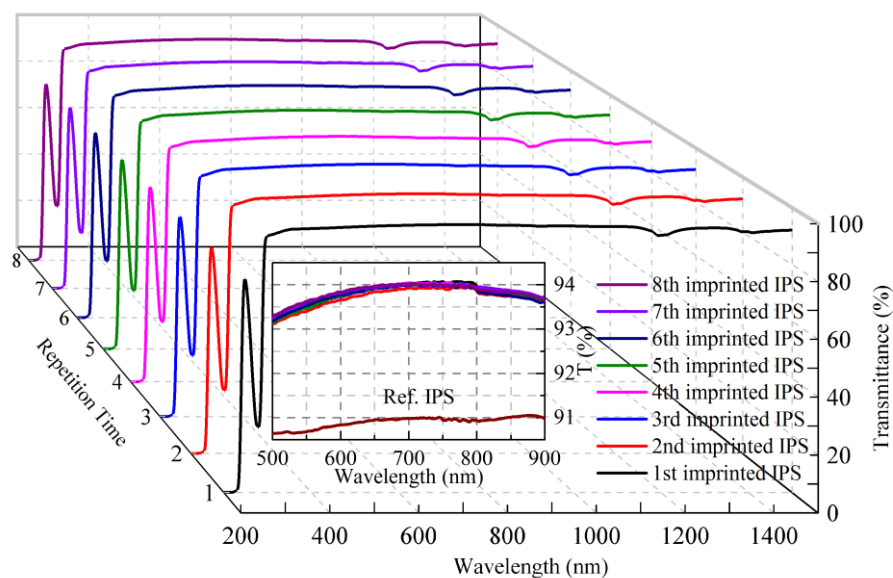
Figure 4-13: Transmittance spectra of IPS[®] sheets consecutively imprinted with the same Suprasil[®] master mold (200 nm in height, 100 nm in inter-pillar spacing and 65 nm in diameter). The transmittance spectra overlap within an accepted deviation range, as shown in the inset. It indicates the optical quality of the imprinted IPS[®] sheets are guaranteed throughout many times of imprinting and the master mold can be reused at least for eight times.
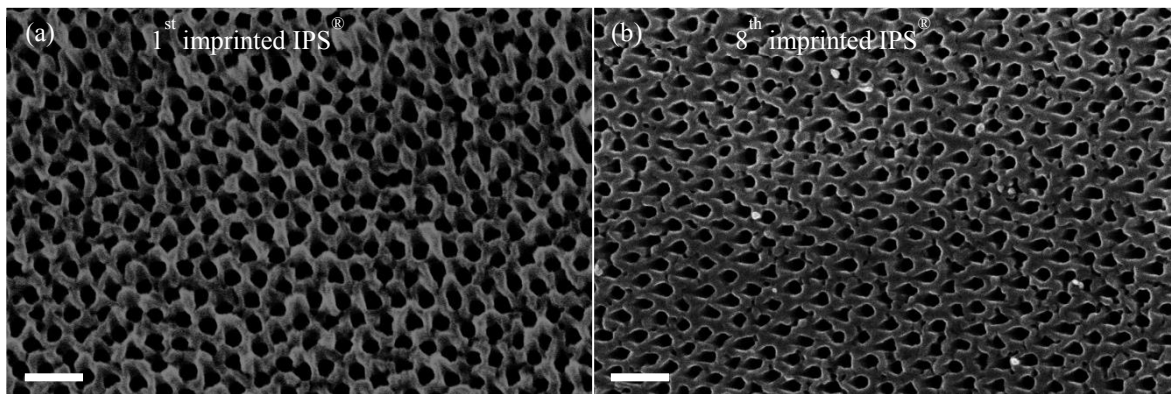
Figure 4-14: SEM images of (a) the 1st imprinted IPS® sheet surface and (b) the 8th imprinted IPS® sheet surface from the same master mold (200 nm in height, 100 nm in inter-pillar spacing and 65 nm in diameter). It shows the size of the nanoholes and the hexagonal arrangement are consistent. Scale bars: 200 nm.

4.4.2 Anti-reflection of the IPS® with single-sided nanopillar surface

Glancing angle deposition (GLAD) assisted Au nanohole array mask

A SiO_2 substrate with nanohole arrays was also fabricated with the glancing angle deposition (GLAD) technique [173]. Mr. Hyeon-Ho Jeong from Prof. Peer Fischer's group did the GLAD deposition [174].

This technique utilizes the BCML prepared Au nanodot arrays tilted at a large angle in order to produce a shadowing effect from the Au nanodots (see sketch in Figure 4-15). Using BCML-prepared samples on a SiO_2 surface (*e.g.* inter-particle spacing and diameter of approx. 100 nm and 9.5 nm, respectively, with polymer: 1056-*b*-671, loading rate: 0.5), samples were tilted at an angle of around 80° in order to deposit an Ag layer on the Au nanodots but not on the surface between the dots, as this area was covered by the shadow (Figure 4-15 (a)). The diameter of the dots was then increased as the Ag layer enveloped the Au nanodots (Figure 4-15 (b)). Another deposition step with Au at a normal incidence angle was then performed to form an Au/Ag/Au hybrid mask (Figure 4-15 (c)). After that, H_2O_2:NH_3 (1:1) was used to dissolve the Ag, followed by sonication to remove the Au dots (Figure 4-15 (d)). An Au nanohole array mask with partial Au nanodots in the center was obtained. Subsequent RIE could achieve different depths of nanoholes on the SiO_2 substrate (Figure 4-15 (e)). Although the Au nanodots can also serve as a mask, they are trapped in the nanoholes such that the etching rate to the dot-covered area is much faster than the flat areas. Thus, after etching, a nanohole array structure can be achieved. For nanoholes with shallow depths, there was a small protuberance sitting in the center of the nanohole, but as etching proceeded further, the protuberance was eventually removed.

Two samples with the same masks were prepared on SiO_2, followed by different RIE etching cycles (1 cycle and 4 cycles) in order to make pillar heights of 50 nm and 200 nm, respectively.
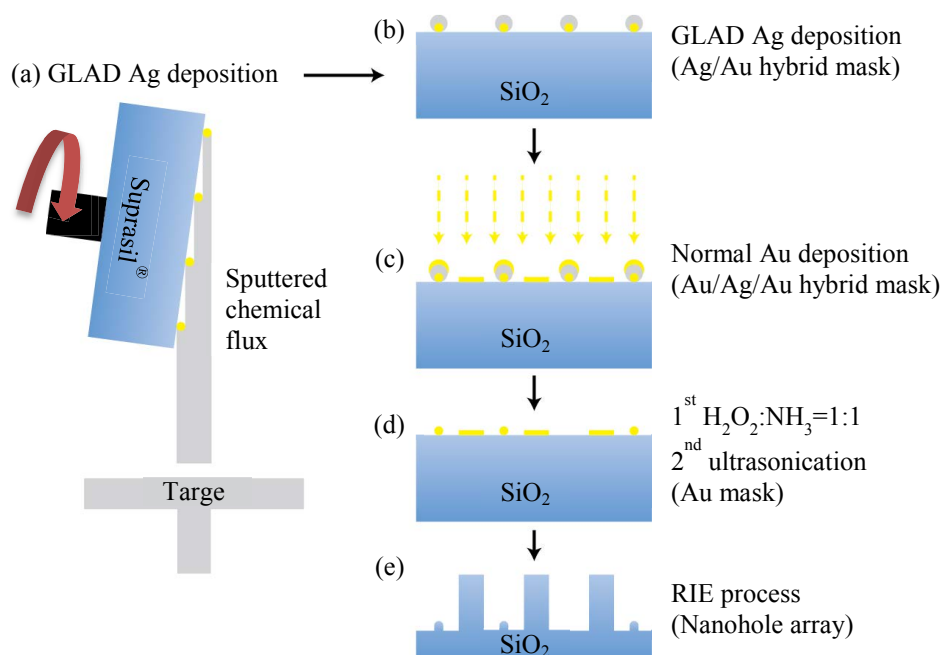
Figure 4-15: Schematic drawing of GLAD assisted nanohole array preparation on SiO_2 substrate. (a) The tilted angle of the substrate is approx. 80°. (b) After deposition an Ag/Au hybrid mask is formed. (c) Au was deposited from normal incidence angle. (d) H_2O_2:NH_3 solution was used to dissolve and remove the Au-covered Ag layer. During this step, the Au-covered Ag layer can be thoroughly cleaned, however the Au nanodots underneath were statistically removed by sonication. (e) Finally the nanohole array can be achieved by RIE.

The structure of the IPS® with single-sided nanopillar surface

The prepared SiO_2 substrates with nanohole arrays were used as the molds to do the nanoimprinting on IPS® substrate surfaces. The same nanoimprinting parameters were used as described in Section 4.4.1.

Figure 4-16 shows the surface of the master mold with the nanohole array and the surface of the imprinted IPS® polymer with nanopillar array. Group (a) shows the sample with nanoholes and nanopillars of 50 nm in height and 50 nm in diameter. The image and the inset in Figure 4-16 (a_1) show there are a number of nanoholes with one small, bright nanodot in the middle. Similarly, the imprinted polymer nanopillars also show the corresponding nanoholes, seen as dark shadows in the center at the top of the pillar (Figure 4-16 (a_2)). The nanodots are the residual Au nanoparticles from the BCML process that are not yet completely consumed by the etching process. On the right side, group (b) shows a sample etched longer in RIE, in which no small Au nanodots are observed. By imprinting, longer nanopillars with approx. 200 nm in length and 50 nm in diameter (Figure 4-16 (b_2)) can be achieved. The advantage of this method is that it provides a useful technique to reverse the Au nanodot mask by the BCML technique, and the polymeric nanopillar array can thus be imprinted. However, the disadvantage is the inter-hole spacing is limited by the Au nanoparticle size, as the GLAD technique highly depends on the shadowing effect. Therefore, it is very challenging to modi-

fy the inter-spacing in this method. Moreover, the overall process is complicated and time-consuming.
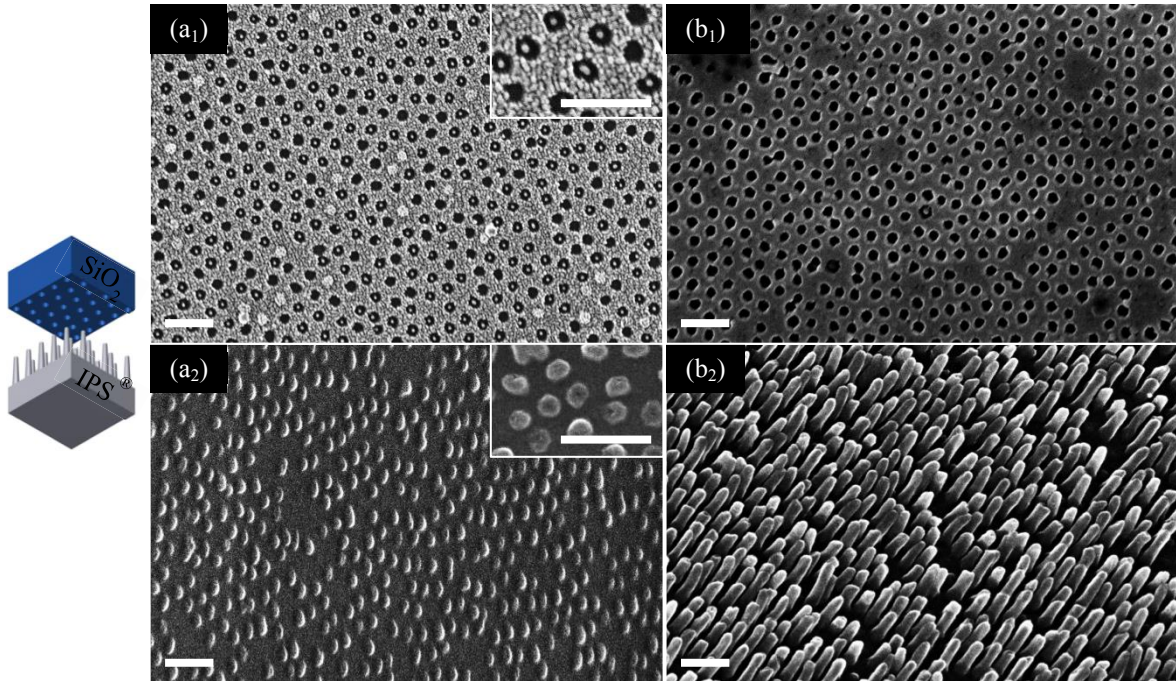
Figure 4-16: SEM images of SiO$_2$ molds produced using GLAD (a$_1$, b$_1$) and the corresponding polymers after imprinting (a$_2$, b$_2$). (a) Shallow nanoholes result in short IPS® nanopillars of 50 nm in height. (b) Deep nanoholes result in long IPS® nanopillars of 200 nm in height. The schematic drawing on the left illustrates the used approach. Scale bars: 200 nm.

The transmittance of the IPS® with single-sided nanopillar surface
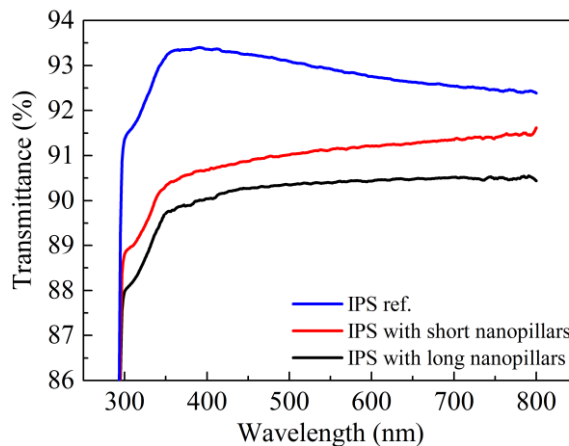
Figure 4-17: Transmittance measurement of the IPS® with nanoimprinted nanopillars of different length, 50 nm (red curve) and 200 nm (blue curve). The IPS® was imprinted with a Suprasil® master mold covered by nanohole array that was prepared by the GLAD technique (Prof. Fischer's Group).

Successfully imprinted IPS® sheets with nanopillar arrays also exhibit an anti-reflection property, as shown in Figure 4-17. Similar to the AR properties of the polymeric nanohole structures in Figure 4-12, the transmittance increases with increasing height of the structures.

Compared with the nanopillar structure, the nanohole structure is more desirable for AR coatings, as the holes are presumably more stable and resistant to mechanical stress.

4.4.3   Anti-reflection of the IPS® with double-sided nanohole surfaces

Nanostructures presenting on both sides of the substrate is essential for the optical properties of anti-reflection and transmittance, as the light transmits through the substrate and the reflections occurs at the interface on both sides. With nanostructures on both sides, the transmittance can be improved two-fold compared with one-sided nanostructured substrates. Hence, imprinting was performed on both sides of the substrate.

Two Suprasil® master molds were prepared with nanopillar heights of approx. 100 nm and 200 nm. The inter-spacing between pillars was approx. 100 nm. After silanization with FDTS-silane, the IPS® sheet was imprinted on both sides with the two molds, as shown in the schematic drawing in Figure 4-18.

The structure of the IPS® with double-sided nanohole surfaces

The SEM images in Figure 4-18 show the morphology of the IPS® surfaces with imprinted nanoholes on both sides. Although the combined molds successfully imprinted nanoholes on both sides, the demolding process is extremely difficult, especially for high nanopillar structures. It is difficult to remove the imprinted polymer away from the mold, and the molds can be easily damaged in the demolding process. Compared with the one-side imprinting, the demolding problem stems from the two rigid master molds sandwiching the soft polymer. As only very small deformations are allowed for the hard mold, and the deformation of the polymer sandwiched in between is also restricted, the process becomes more challenging than the one-side imprinting, in which the soft polymer can be peeled off with ease. Thus, soft master molds were introduced for better detachment in double-sided imprinting experiments and the results are shown in Section 4.5.1.
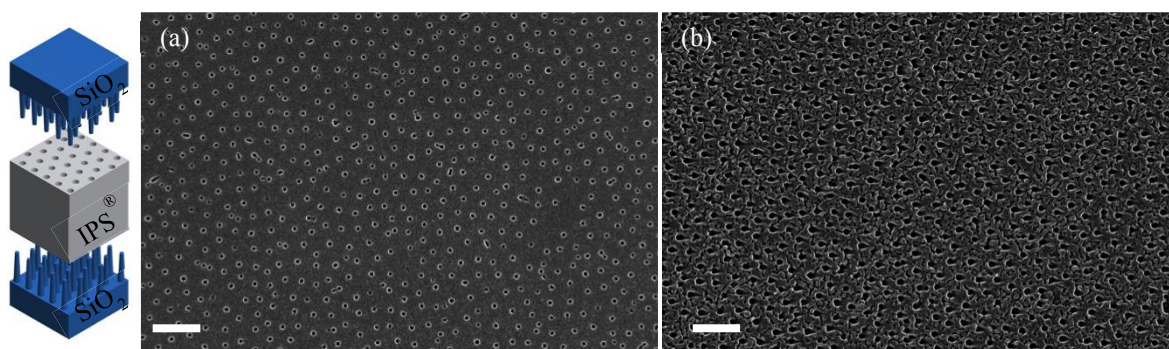
Figure 4-18: Double-sided imprinting of polymeric nanoholes. The sketch of the method is shown on the left. SEM morphology images of the IPS® surfaces with replicated nanoholes of (a) 100 nm in depth on the topside and (b) 200 nm in depth on the bottom side. Scale bars: 400 nm.

The transmittance of the IPS® with double-sided nanohole surfaces

The transmittance of the two Suprasil® molds was measured as shown in Figure 4-19 (a). One is a nanopillar array with height of approx. 100 nm (red curve) and the other is that with approx. 200 nm (blue curve). The transmittance of the corresponding one-side imprinted IPS® sheets are shown in Figure 4-19 (b). The extra pink curve on the top is the IPS® sheet imprinted with a combination of the two molds. The double-sided imprinted IPS® exhibits a transmittance up to 94.3%, which is higher than the single-side imprinted IPS® sheets. Moreover, the improvement of the double-sided sample is approx. the linear superposition of the increments of the two single-sided imprinted IPS® sheets.
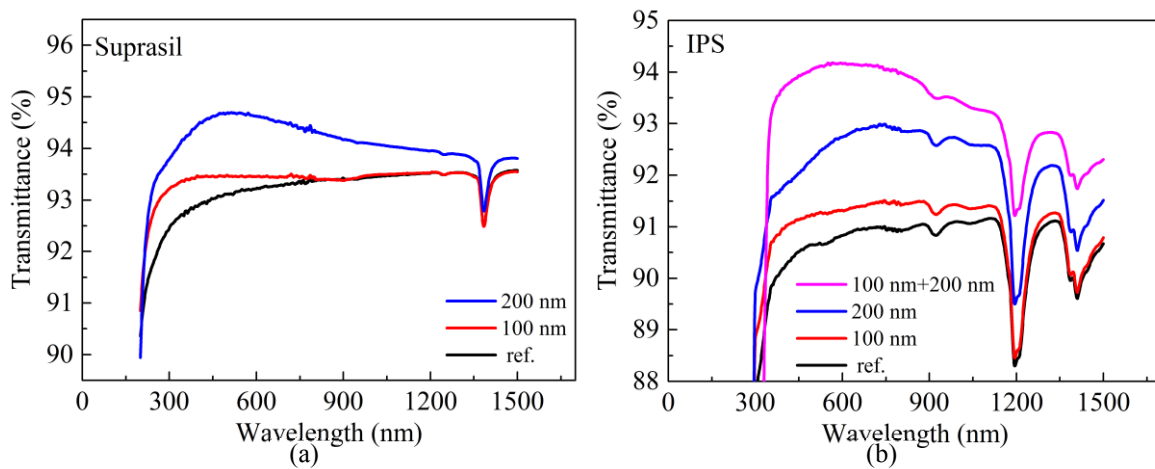
Figure 4-19: Transmittance of the Suprasil® molds (a), the single-sided imprinted IPS® sheets (red curve and blue curve in (b)) and double-sided imprinted IPS® sheets (pink curve in (b)). The interspacing of nanostructures is kept at 100 nm.

4.5 Anti-reflective properties of the PMMA

4.5.1 Anti-reflection of the PMMA with double-sided nanopillar surfaces

In addition to the commercial IPS® sheet designed for nanoimprinting the nanopillar structure, replication on the PMMA sheet was also investigated because of its high biocompatibility and good transparency.

The principle of the nanoimprinting is to heat up the polymer to a temperature higher than its glass transition temperature, at which point the polymer will melt to the liquid state and can flow under a certain pressure. Thus, an ideal material for double-side imprinting is a soft polymeric material with glass transition point higher than the working temperature of the imprinted polymer. The glass transition temperature of the IPS® and PMMA is approx. 140°C and 105°C, respectively. Hence, the working temperature of PMMA can be set between 105°C and 140°C, which is below the glass transition of IPS®. It would well preserve the nanostructures on the mold. Here, the imprinting temperature, the duration of imprinting and the demolding temperature were set to 130°C, 1 min and 70°C, respectively. The master mold of Suprasil® was prepared with 200 nm-height nanopillars and the intermediate tem-

plate of IPS® sheets were imprinted on this master mold with nanohole arrays on the surface. Nanopillar structures on PMMA substrate were achieved by sandwiching the PMMA sheet in between the imprinted IPS® sheets (schematic drawing in Figure 4-20). Therefore, the imprinted PMMA sheet has nanopillars with a height of approx. 200 nm.

The structure of the PMMA with double-sided nanopillar surfaces

As shown in Figure 4-20, the SEM pictures of the resulting PMMA sample reveal that both sides of the sample were successfully imprinted with nanopillars with height of approx. 200 nm. The nanopillars are not perfectly straight, which is likely due to the fact that the demolding temperature of 70°C is still within the transition region where the nano-scale PMMA pillars are very soft and thus can deform during the detachment process. However, according to Siddique *et al.* [175], irregular oriented nanopillars likely have better anti-reflection effect, especially at large incident angles. One big advantage of the soft molds is that they are easily deformable, thus the demolding process is no longer a problem. Moreover, as the working temperature was always kept under the glass transition temperature of the mold material, the mold can be used many times before wearing. In this experiment, the same mold was used 5 times and nanopillar structures can still be replicated, with no visible wearing found on the mold. This is advantageous because it can further lower the fabrication costs.
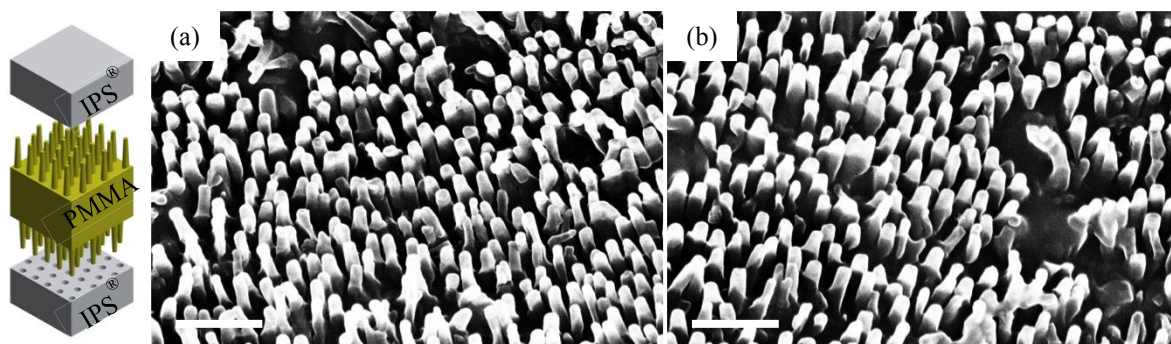
Figure 4-20: SEM images of the PMMA surfaces with nanopillar height of 200 nm on both the top-side (a) and the bottom side (b) replicated from the IPS® master molds. The sketch on the left shows the double-sided nanoimprinting method with soft IPS molds. Scale bars: 400 nm.

The transmittance of the PMMA with normal incident light

Figure 4-21 illustrates the transmittances of single-sided and double-sided imprinted PMMA sheets compared with the reference PMMA sheet without nanostructures. The reference sample was imprinted with a plain IPS® sheet. Transmittance was measured in the wavelength range from 400 nm to 1500 nm because the PMMA sheet is not transparent to UV light. The figure shows that the planar PMMA sample (Figure 4-21, black curve) has a transmittance of approx. 91.5% on average. The sample with single-sided imprinted nanopillars (Figure 4-21, red curve) shows maximal 3% increase of the transmittance compared with the reference sample throughout the entire measured wavelength range. The maximum increase occurs between 400 nm and 900 nm, which is in the visible range. For the sample with double-sided nanopillar-modifications (Figure 4-21, blue curve), the transmittance is even higher, with a

maximum of 96.5%, which shows an additional 3% increase compared with the single-sided nanostructured PMMA. The transmittance of the double-sided nanopillars is increased by a factor of two compared with that of the one-sided nanopillars. This is consistent with the above-discussed model to explain the AR property of the double-sided Suprasil® substrate.
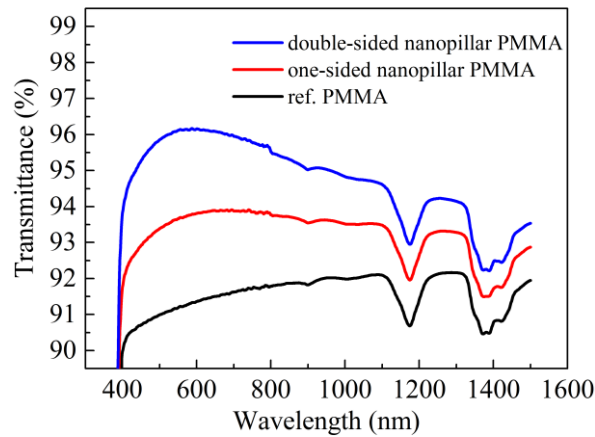
Figure 4-21: Transmittance measurement of the PMMA sheet with single-sided (red curve) and double-sided (blue curve) imprinted nanopillars, comparing with the plain PMMA as a reference (black curve). PMMA nanopillar height is approx. 300 nm in height.
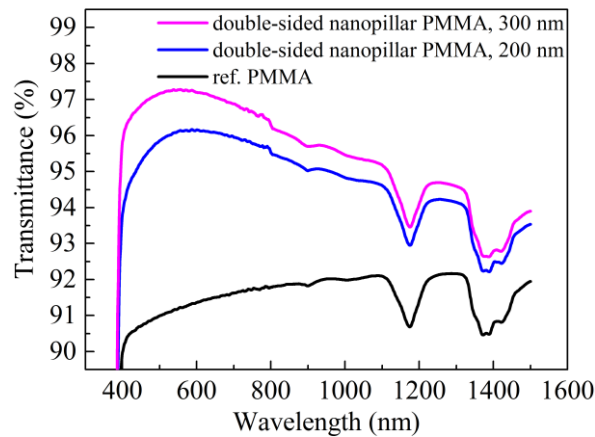
Figure 4-22: Transmittance measurements of the PMMA sheet with double-sided nanopillar arrays of increased pillar heights, *i.e.* 200 nm (blue curve) and 300 nm (purple curve) compared to an unstructured PMMA.

In principle, the transmittance of PMMA with nanopillar arrays should be further improved with longer nanopillars until it reaches hundred percent. A further nanoimprinting experiment was done with the Suprasil® mold covered by higher nanopillars of 300 nm. First, the IPS® sheets were imprinted, and then they were used as molds to imprint PMMA. This imprinted PMMA is compared with the PMMA prepared with relatively shorter length as shown in Figure 4-22. The transmittance can be increased to as high as 97%, and 96% on average rang-

ing from 400 nm to 1000 nm. This transmittance level is even higher than that of a bare silica substrate (93%) and comparable to Suprasil® with single-sided AR coating. Thus double-sided imprinted PMMA can lead to numerous optical applications. Figure 4-23 gives a picture showing the PMMA samples with and without nanopillar structures. It can be seen that the substrate with nanopillar arrays on both sides reveals a clear "Max Planck Society" logo with a lower reflection.
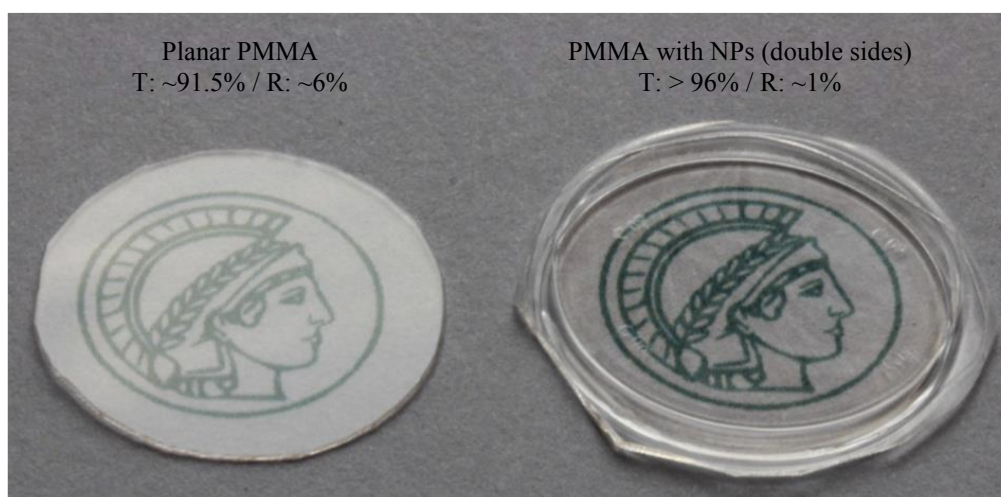
Figure 4-23: PMMA sheets with/without nanopillar array placed on a piece of paper printed with "Max Planck Society" logo. It can be easily seen by bare eyes that the reflection is remarkably reduced with the nanostructure array. Quantitatively, the planar PMMA has only a transmittance of 91.5% and reflectance of approx. 6% on average. The PMMA with nanopillar array on both surfaces has improved the transmittance to higher than 96% and the reflectance is reduced to 2.5% on average over the measured wavelengths (minimum of 1% at 400 nm). The diameter of the PMMA sheet is 20 mm.

Angle-dependent transmittance of double-sided imprinted PMMA

Measurement of angle-dependent transmittance was carried out with a Goniometer integrated on transmittance- and reflectance-measuring units. PMMA samples with double-sided nanopillars were prepared by a two-step nanoimprinting procedure using two sheets of imprinted-nanohole IPS®, as shown in Section 2.4.3. The nanoholes on IPS® were imprinted with a rigid Suprasil® mold that is covered by nanopillars with spacing of 100 nm and height of 300 nm.
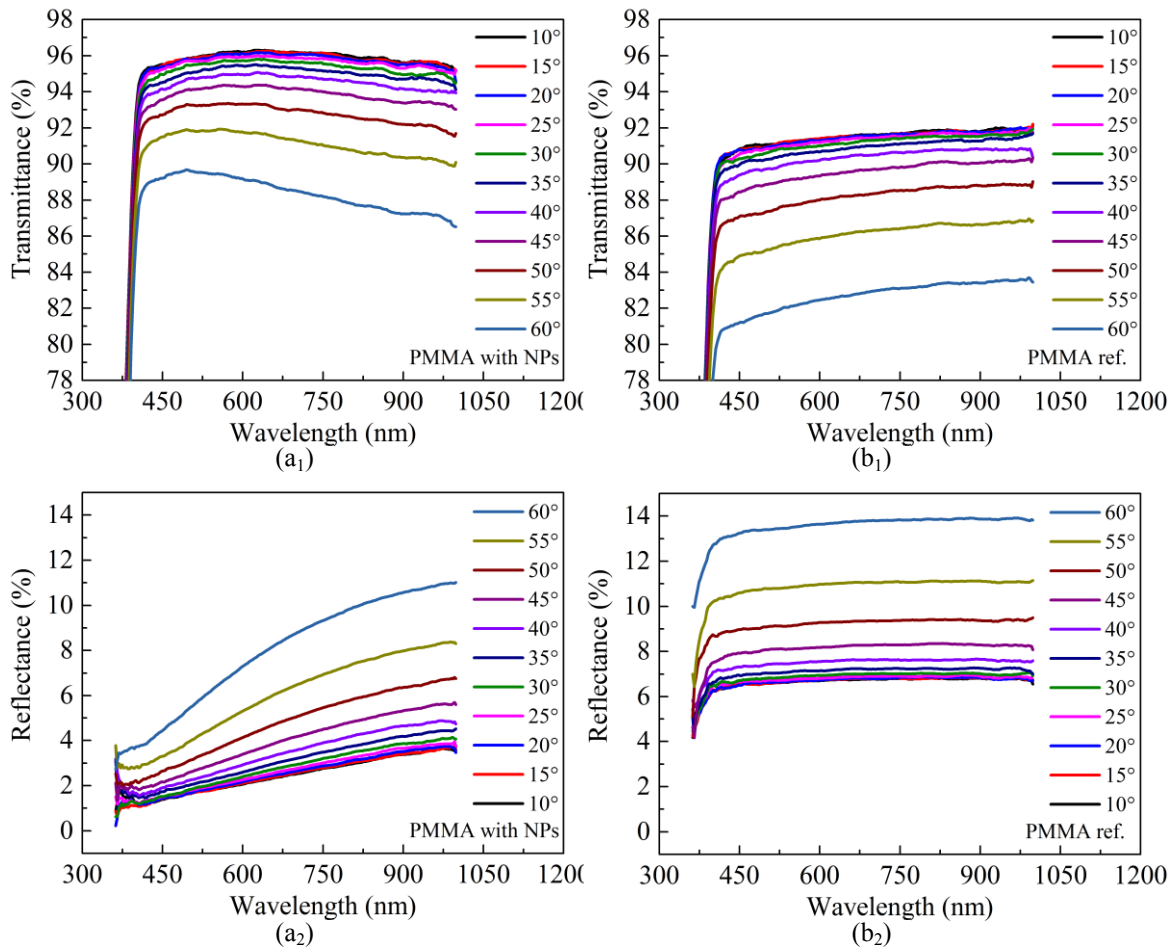
Figure 4-24: Angle-dependent transmittance and reflectance of the PMMA with/without nanopillars (NPs) measured with the incident angle from 10° to 60°. (a_1) and (a_2) are the spectra of transmittance and reflectance measured on a PMMA substrate with nanopillar prepared on both sides (b_1) and (b_2) are the spectrum measured on reference sample of the PMMA.

Figure 4-24 shows the transmittance and reflectance of nanostructured PMMA (a_1) (a_2) compared with the control sample (b_1) (b_2) at varied incident angles from 10° to 60°. At 10°, the PMMA reference sample has its highest transmittance of only 91%. However, with the nanopillar array, it reaches about 96%. Even at high incident angle of 55°, the average transmittance of the PMMA with nanopillars remains larger than 91%. When comparing the reflectance, an excellent AR effect over the whole measured wavelength range, from 400 nm to 1000 nm, is observed. At the smallest incident angle of 10°, the average reflectance of the PMMA is significantly reduced from 6% to 1%. The reflectance is better suppressed at smaller wavelengths because the size of the nanostructures, *i.e.* the inter-pillar spacing is 100 nm, which is the size for sub-wavelength range of UV light (100 nm-400 nm).

Figure 4-25 shows the angle-dependent transmittance at two typical wavelengths, 400 nm and 587 nm. At 400 nm, which is the lowest wavelength possible for PMMA without severe absorption originating from the material itself, the average reflectance of pillar-structured PMMA is 5% lower than the plain PMMA sheet. Additionally, the AR effect is more signifi-

cant at higher incident angle, *e.g.* 60°, in which the reflectance dramatically reduces from 13% to 3.5%. At 587 nm, which is an important wavelength for lasers in the visible light range, the average reflection also exhibits a more than 4% reduction. These results demonstrate that the AR effect of the imprinted nanostructures is largely incident angle independent. It yields excellent AR properties spanning from low to high incident angles. This property is essential for imaging optical systems, such as camera lenses and contact lenses, as well as for optical displays, such as screens for cell phones and televisions.
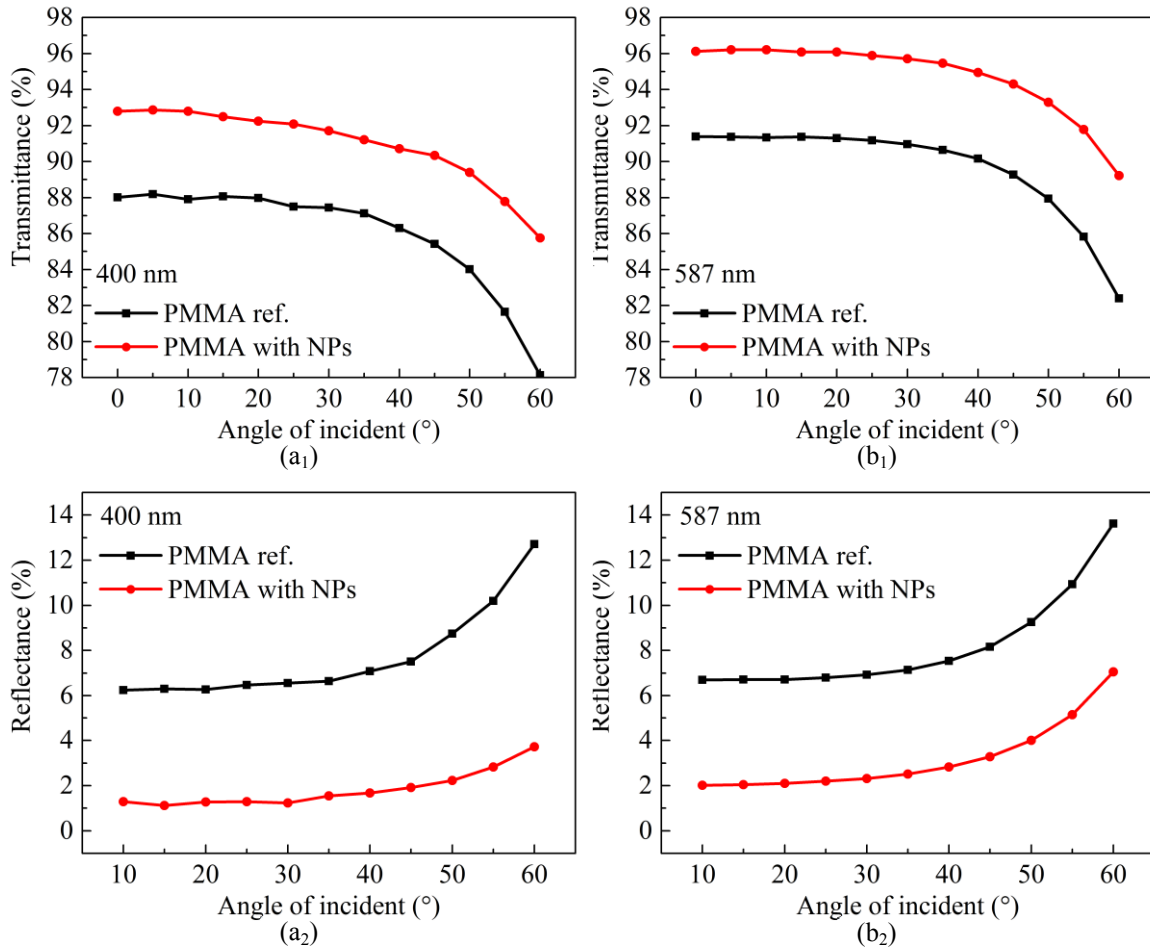
Figure 4-25: Angle-dependent transmittance and reflectance of the PMMA with nanopillars of 400 nm in height on both sides of the surfaces compared with a planar substrate as a reference at wavelengths of 400 nm and 587 nm.

4.5.2 Anti-reflection of PMMA with nanohole arrays on curved surfaces

Concave and convex lenses are commonly used in optical systems. For example, the surfaces of contact lenses and intraocular lenses have a certain curvature for light focusing and light path correction. One advantage of polymeric materials is their flexibility and thermoplastic properties, which enable the fabrication of a designed curvature. Based on the success of the previously mentioned nanoimprinting approaches on flat substrates, nanoimprinting on curved surfaces is discussed in this section. Imprinting the polymer sheet into designed curvature, as well as nanostructures on both surfaces, is completed in one step, as shown in Fi-

gure 4-26. These processes are combined into one step for two reasons: 1) if two imprinting steps for curvature and nanostructures are done in sequence, the latter step will always affect the structure formed in the previous step; and 2) combining the two steps simplifies the imprinting process, thus decreasing processing time and cost. However, combining processes also poses an extra challenge to fabricate the molds. Here, the method of imprinting a curved SiO_2 mold with nanostructures into polymers is studied.

The structure of PMMA with nanohole arrays on curved surface

As illustrated in Figure 4-26 (a), the molds are designed with two different curvatures. The convex one corresponds to the inner surface of the contact lens, which is in contact with and has similar curvature to that of the cornea of the human eye. The concave one is the outer surface of the contact lens, whose curvature leads to the magnification of the lens. The molds are made of Suprasil®, which allows for direct preparation of the nanopillar array by BCML and RIE techniques. Before preparing the nanostructures, the surfaces of the molds were finely ground to achieve low surface roughness.
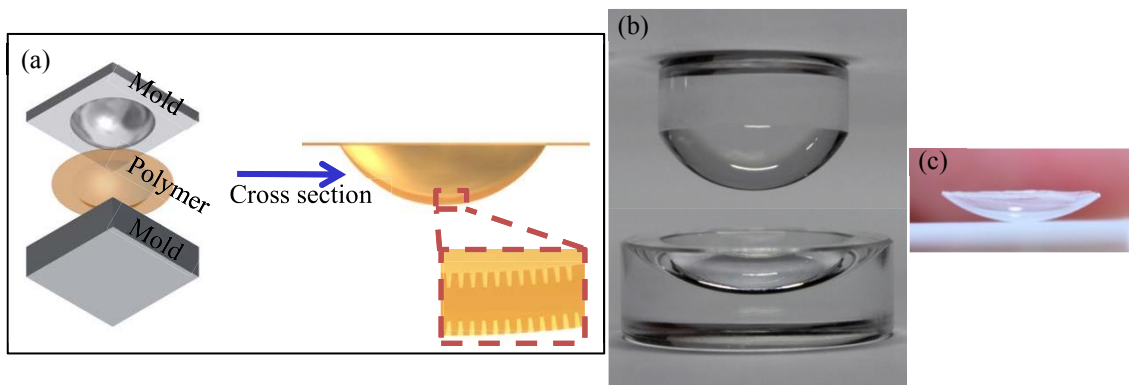
Figure 4-26: Curved surface nanoimprinting with concave and convex molds. (a) Illustration of the imprinting scheme. (b) Picture of the two molds. (c) Picture of the imprinted curved PMMA sheet with double-side nanohole array.

Nanopillar arrays with 400 nm height were prepared on the molds by using BCML and RIE techniques, and the obtained concave and convex molds were subsequently used for nanoimprinting with PMMA substrates. The SEM images in Figure 4-27 show that the convex surface has a relatively better nanohole array than the concave surface. However, several defects and distortion of the nanoholes can be observed. On the concave surface, the nanostructures are completely damaged and the expected nanohole array was not achieved. It is likely because the demolding of the concave surface is much more difficult than the convex surface. During the demolding process, the nanostructure is severely stretched and destroyed. However, as a proof-of-concept experiment, this study shows that it is possible to fabricate nanostructures on curved glass. Moreover, these structures, as well as the curvature, can be replicated with a polymer via this one-step nanoimprinting.
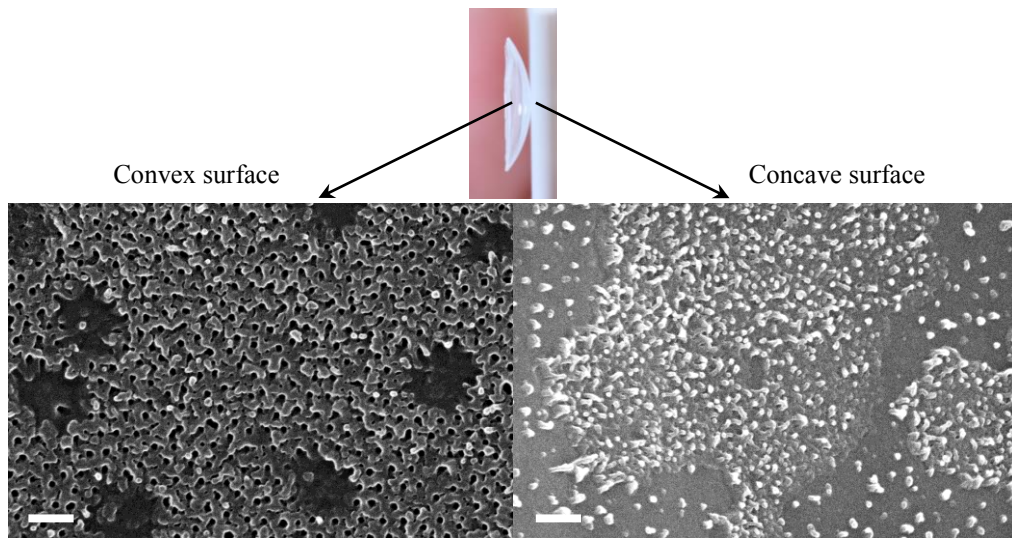
Figure 4-27: SEM images of the imprinted curved PMMA surfaces. (a) The convex surface is imprinted with homogenous nanoholes. Small areas of defects are probably caused by trapped air. (b) The nanohole structures on the concave surface are largely distorted. Master mold: Curved Suprasil® surfaces with 400 nm height nanopillar array. Scale bars: 200 nm.

The transmittance of PMMA with nanohole arrays on curved surface

Transmittance measurement was carried out on two samples, one is imprinted with an unstructured and curved Suprasil® mold; the other one is imprinted with a nanopillar-structured (400 nm pillar height) and curved Suprasil® mold. The measured spectra of the curved PMMA sheets are shown in Figure 4-28.
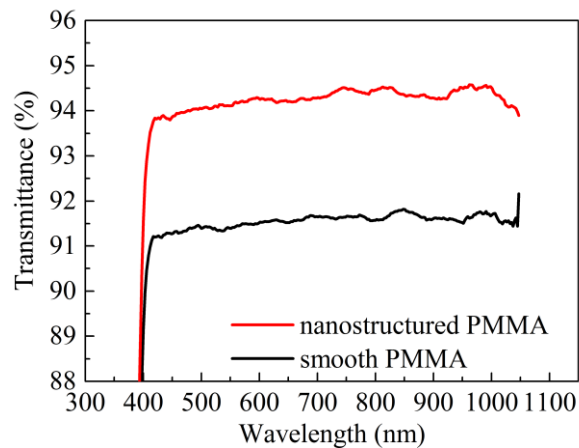
Figure 4-28: Transmittance of the imprinted curved PMMA. One is the sample imprinted with unstructured and curved Suprasil® molds (black curve) and the other sample is imprinted with nanopillar-structured and curved Suprasil® molds (red curve).

The transmittance of the nanopillar-imprinted curved surfaces was compared to surfaces imprinted with a smooth curved Suprasil® mold (Figure 4-28). The imprinted curved PMMA substrate shows a 3% improvement in transmittance over a wide range of wavelengths, from 400 to 1000 nm, compared to the smooth PMMA substrate (Figure 4-28). Compared with the planar surface of IPS® imprinted with the same depth of nanoholes on a single side whose

transmittance is improved by 4% (Figure 4-12 (d)) the transmittance of this curved PMMA with double-sided nanoholes is only improved by 3%. This is probably due to the defects of the imprinted nanostructures on the curved surface (as seen in the SEM image in Figure 4-27), where the optical properties could be further improved by a better replication of the nanohole structures.

4.6   Application of nanoimprinting on commercial intraocular lens material

Different types of polymers were studied for specific applications, including ETFE, PMP, PET, PP, CX72323 and CI26 as mentioned in Section 2.3.2. The polymer information and imprinted SEM images of the first five polymers are shown in Appendix Table 6-2 and Figure 6-3. Results of imprinted CI26 substrates are shown here.

CI26 is a copolymer of hydroxyethyl methacrylate (HEMA) and methyl methacrylate (MMA). Most importantly, this material is used in commercial applications for intraocular lenses due to its excellent mechanical and optical properties. CI26 is also resilient for easy insertion into the posterior chamber of the eye through a small incision. The material has a refractive index of 1.46 and is thermoplastic, which is important for anti-reflection and nanoimprinting. CI26 disks, which are used for imprinting in this experiment, have a diameter of 15 mm and thickness of 3 mm. Based on the previous results of imprinting IPS$^{®}$ and PMMA polymers, it is possible that the nanoimprinting approach can be extended to this commercial material. Different Suparsil$^{®}$ master molds were tested on the CI26 disk under hydraulic pressure and two different imprinting temperatures and demolding temperatures.

Figure 4-29 shows the CI26 surfaces after imprinting with nanopillar arrays on Suprasil$^{®}$ master molds. Sample (a) is imprinted with a dense nanopillar array of 50 nm inter-spacing and sample (b) is imprinted with a less dense array of 250 nm inter-spacing. While nanoholes can be detected under 25k magnification, it is clear that both samples also exhibit large areas with defects. Such defects are due to the difficulty in detachment during the demolding process in which residual polymer is left on the master mold surfaces. This strong attachment between the silanized master mold and the CI26 surface is due to the hydrophilic surface of the CI26 disk. However, comparing the two samples, sample (b) shows relatively better surface morphology than (a), with a relatively large, homogenous area of imprinted nanoholes due to the larger inter-pillar spacing and smaller surface area.
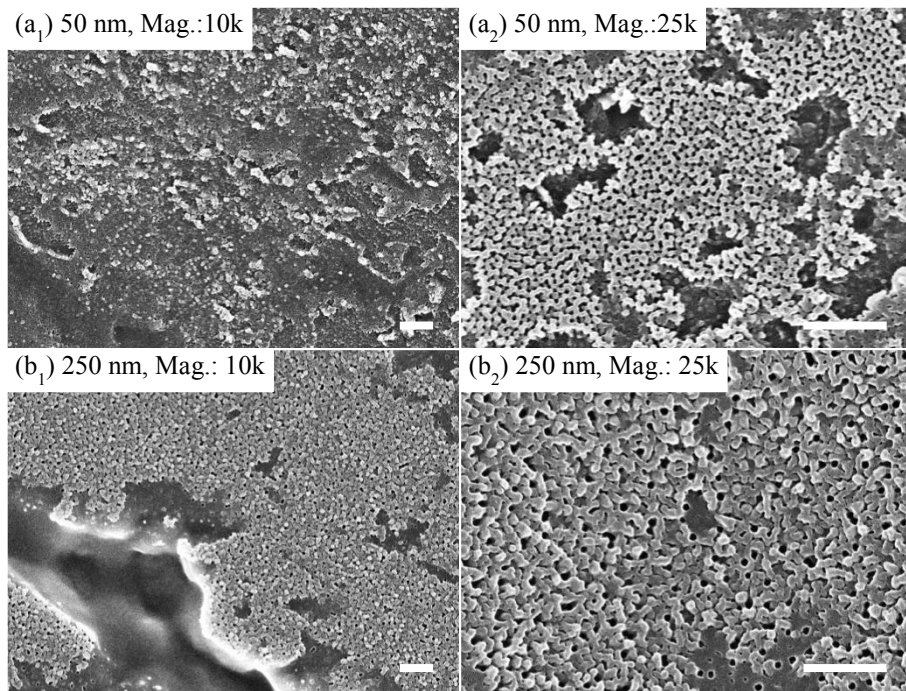
Figure 4-29: CI26 disk imprinted at 130°C and demolded at 25°C when the material is in plastic regime. Two molds with different nanopillar inter-spacing were used, *i.e.* 50 nm (a) and 250 nm (b), respectively. The pillar heights and diameters are both approx. 200 nm. Scale bars: 500 nm.
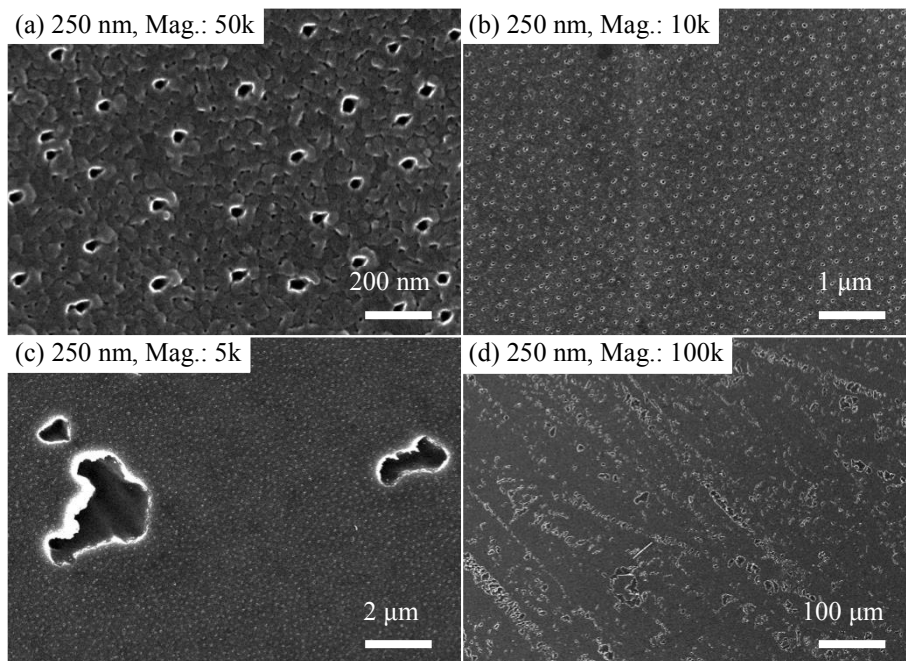
Figure 4-30: Nanohole array imprinted on CI26 disk. The sample was imprinted at 150°C and demolded at 65°C. The master mold is with nanopillar array of 70 nm in diameter, 250 nm in spacing and 100 nm in height. (a)-(d) are with decreased magnification under SEM, and micro-scale defects are observed with small magnifications.

Figure 4-30 shows the SEM morphology of imprinted CI26 surfaces at higher temperature, which is expected to improve the imprinted nanohole structure. The imprinting temperature is

raised to 150°C and the demolding temperature to 65°C. The master mold has a nanopillar array of 250 nm inter-spacing and 100 nm height. Figure 4-30 (a) and (b) show well-replicated nanohole arrays; however, under low magnification in (c) and (d), there are still some defects found on the surface. The defects are at the micro-scale, which are different from the nano-scale defects observed in Figure 4-29, and they are likely due to the surface roughness, which can be improved by fine grinding the CI26 disk surface before fabricating the nanostructures. This shows that it is in principle possible to transfer the imprinting method to CI26 disks, but further optimization is necessary.

4.7   Discussion

4.7.1   Comparison of nanoimprinting with molding techniques

Replica molding method is commonly used to fabricate micro- and nanostructures on soft polymeric substrates such as PDMS. By casting the liquid polymer solution of an elastomer on the master mold, the micro- and nano-scale surface features on the mold can be readily replicated. As developed by Whitesides and colleagues [47], a chromium master with 13 nm-in-width lines and a gold master with 50 nm-in-width lines can both be replicated onto PDMS [41]. Therefore, the first methods used in this thesis for the nanostructure replication are the "pressure molding" and "vacuum molding" (section 4.2.2), both of which are based on the same principle of the replica molding. As seen in Figure 4-4, the nanohole array with diameter of 30 nm on the PU substrate was successfully replicated by the vacuum casting method. Compared with the 2D line nanostructures discussed by Whitesides *et al.* [162], our 3D grating structure is more difficult to be made by the soft lithography technique, as the air trapped between the nanopillars are difficult to be substituted with polymer. Moreover, a gentle process of mold and polymer separation was also required to prevent the damage of nano-pillars inside the polymer.

However, there are two disadvantages of the replica molding methods: 1) large pressure is required to make the liquid polymer completely fill the space between nanopillars; 2) the area size and homogeneity of the nanostructure are limited as described in Section 4.2.2 (Figure 4-4). Chou *et al.* [18] reported a novel technique called hot embossing or nanoimprinting to replicate nanostructures down to 25 nm resolution. This method was specifically developed in this thesis in order to transfer the nanopillar arrays on Suprasil® substrate to polymeric materials. Both positive (pillar structure, section 4.4.2 and 4.5) and negative (hole structure, section 4.4.1 and 4.4.3) nanostructures were replicated on the polymer substrates. The size of the achieved nanohole diameter is ranging from 35 nm to 70 nm on substrates with 20 mm in diameter. Compared to the molding methods discussed above, nanoimprinting utilized thermoplastic polymers and took only about 10 min. to replicate a surface instead of several hours for the molding process. It also has advantages of higher resolution in both vertical and lateral dimensions. Additionally, for industrial applications, the reusable master mold and the large scalability are two important beneficial factors.

4.7.2 Nanostructures imprinted on PMMA substrate

Regarding the nanoimprinting, besides the commercially available IPS® sheet, PMMA is a well-known thermoplastic material that can be used for nanoimprinting. Its glass transition point is approx. 105°C, and it is reported that the thermal shrinkage and the pressure shrinkage are less than 0.8% and 0.07% under 140°C and 600 psi [18], which are also the same conditions used for nanoimprinting in this thesis. With the novel Suprasil® master molds with nanopillar arrays, versatile polymeric stamps can be prepared by appropriately setting the working temperature and pressure according to the specific glass transition point of each polymer. PMMA sheets can either be imprinted with nanoholes as same as the preparation of IPS® sheets (Figure 6-5 in appendix) or the nanopillars as shown in Figure 4-20.

Moreover, the nanostructures were realized on soft polymeric substrates, which means the structures can be readily fabricated onto a curved surface (shown as a proof-of-concept in Figure 4-27) and the polymeric material is intrinsically biocompatible. Both of these merits are essential properties for biomedical applications, such as the intraocular lens or the contact lens. Therefore, the method introduced here has the potential to be further developed as a general technique for nano-scale surface coatings for biomedical devices.

Comparing with other works, *e.g.* Kim *et al.* [176] prepared well-ordered PMMA nanocones (285 nm in diameter, 350 nm in spacing and 800 nm in height) using Si master mold patterned with e-beam lithography. The improved transmittance is only 94.2%. The PMMA nanopillars prepared in this thesis are 80-100 nm in diameter, 100 nm in spacing and 200-300 nm in height. With double-sided nanopillar structure, the transmittance of PMMA can be improved from 91% to 97%, which is much higher than a plain glass substrate (~93%). As the aspect ratio of the nanopillar is high, and the elasticity of PMMA material is low, the imprinted nanopillars appear in random orientations, as shown in the SEM image in Figure 4-20. It is not as straight pillars as those on the moth eye; however, its profile is very similar to the nanostructures on the glasswing butterfly studied by Siddique *et al.* [175] (80 nm in diameter, 140 nm in spacing and 200 nm in height). It was reported the random orientation of the pillars enhances the omnidirectional AR property of the nanostructures. The high transmittance of PMMA was also observed in the presented experiments (Figure 4-21, Figure 4-22, Figure 4-23). Additionally, the AR effect is effective from normal incidence to a high incident angle of 60° (Figure 4-24), which is an obvious advantage over the traditional thin-film coating method.

4.7.3 Thin-film coating vs Structural coating

In order to minimize the Fresnel reflection loss, conventional approach of thin-film coating was often adopted. The deconstructive interference principle was utilized by adding a single or multiple thin film layers with combined refractive index between the substrate and the air to reduce the reflectance [62]. However, the anti-reflection of the thin film is highly dependent on the incident angle and unstable under high power of the incident light. As seen in (Equation 1-2) and (Equation 1-4), the reflectance vanishes only when it meets the thickness

and refractive index conditions. Therefore, with a given angle of incidence, it only works at the specific wavelength or very narrow spectral wavelength range [177].

In comparison, nanopillar-structured Suprasil® substrates prepared in this thesis possessed a transmittance as high as 99.5% per interface at normal incident angle. Even with an incident angle of 60°, the transmittance can still be as high as 93.5% per interface. Another big advantage is that the AR nanostructure is more stable than optical thin film coatings that may degrade or delaminate [64]. As there are no additional intermediate layer(s) of a different material attaching to the to-be-coated materials, it is highly useful for devices that are exposed to chemicals, humidity or high temperature [64].

4.7.4 Comparison with classical nanostructure AR models

As discussed in Section 3.5.2, our BCML based RIE etching results in unique nanopillar structures with a small nanohole in the pillar center from the top view. To anlayze the optical properties, this hierachical struchture is converted to an equivalent profile with the same filling factor as shown in Figure 4-31.

(a) Etched profile   (b) Equivalent profile
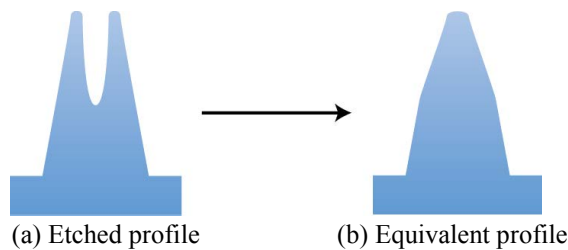
Figure 4-31: Equivalent profile of the nanopillar with the same filling factor for optical modeling.

The optical property of this nanostructured array can be modeled with the effective medium theory (EMT) [178], which is a method that calculates the effective refractive index of subwavelength structures based on the volume fill factor of multiple materials. EMT is only valid when the period of the structure is much smaller than the wavelength, which is true for the nanostructures in this thesis. As shown in Figure 4-33, the effective refractive index is a function of the refractive index of the substrate (n_s), the refractive index of air (n_0), and the structure profile. Several mathematical gradient index profiles have been previously reported [29,66,75], two of which are demonstrated in Figure 4-32 (a), (b) and the simulated response is shown in Figure 4-33. However, the simplified 2D surface relief grating model [29] shows some deviation from the experimental data and the quintic model [68] reported for an ideal model is nearly impossible to be fabricated. Instead of these models, a conical model is established, which calculates the refractive index according to the area fraction via (Equation 4-3). The major difference between the conical model and the other two models is that the gap between the pillars at the bottom layer is taken into account, as illustrated in Figure 4-32 (c). Therefore, the filling factor is lower than 1, and the refractive index exhibits a sudden change at the interface of the structure and the substrate, which can be visualized with the blue curve in Figure 4-33 (a).

(a) Linear profile (2D grating)   (b) Quintic profile   (c) Etched nanopillar profile
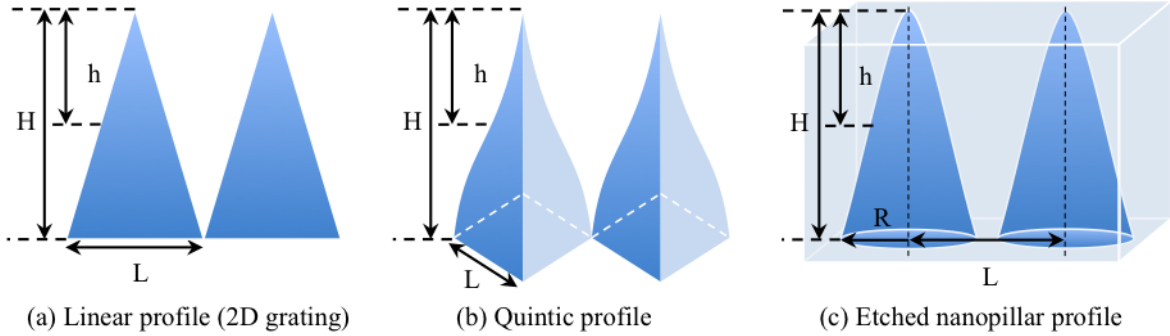
Figure 4-32: Illustrations of the simplified structure profiles for numerical simulation: (a) classic linear profile of a 2D grating, (b) ideal quintic profiles in 3D and (c) estimation of the etched nanopillar profile in 3D.

Linear index profile [29]:

$$n(d) = n_0 + (n_s - n_0)d \qquad \text{(Equation 4-1)}$$

Quinitc profile [68]:

$$n(d) = n_s - (n_s - n_0)(10d^3 - 15d^4 + 6d^5) \qquad \text{(Equation 4-2)}$$

Nanopillar profile:

$$n(d) = n_0 + (n_s - n_0)\frac{\pi(dR)^2}{L^2} \qquad \text{(Equation 4-3)}$$

where n_0 and n_s are refractive indices of the air and the substrate, d is the normalized height and $d = h/H$, h is the height, H is the total height, R is the radius of the conical bottom, L is the periodicity. In the simulation below, n_0 is set to be 1.0 (air), n_s is 1.46 (Suprasil®). R and L are determined from the nanopillar profile (Figure 3-2 (e)), where R is 85 nm and L is 100 nm. H is simulated with a value of 400 nm, which demonstrates the highest transmittance in Figure 4-6.

The calculated effective refractive index of the different profiles are shown in Figure 4-33 (a) based on the geometric filling factor. The calculated reflectance as a function of the depth-to-wavelength ratio is shown in Figure 4-33 (b) based on the optical thin film theory [29]. The simulation was carried out with a custom script in Matlab (R2014b, Mathworks) based on the open source thin film toolbox (TFTB) developed by Griesmann [179]. As shown in the reflectance, the quintic profile is the best geometry among the three, as it provides almost no reflection without any fluctuation as the height increasing. The theory using the 3D conical geometry fits the experimental data very well, which is mainly due to the introduction of a gap between the pillars. As shown in Figure 4-33 (b), within the wavelength range between 400 nm to 1300 nm, the experimental data of the 400 nm-height nanopillar array is consistent with the simulated data of the conical shape, and the reflectance goes to as low as 0.5%. However, in the short-wavelength range, the reflectance is largely increased. This is due to the fact that as the wavelength goes below 400 nm, the absorption and scattering dominates over the transmittance, which can be seen very clearly in the spectrum in Figure 4-6, as the

transmittance reduces dramatically starting from 400 nm. This absorption and scattering effects probably originate from the deviation of the pillar height and inter-pillar spacing during the fabrication process [66].

Comparing the conical shape to the other two models, there is a difference of 0.5% in reflectance. This is due to the discontinuity of the effective refractive index from 1.25 to 1.46 near the interface observed in Figure 4-33 (a). This sudden change is caused by the gap between neighbored cones. At this gap, the filling factor is clearly seen at the interface, although it is not as perfect as the quintic profile that equals 1. In principle, when the filling factor near the interface is close to 1, the reflectance is lower. As the pillar height is kept constant, with the periodicity decreasing, the filling factor approaches 1, causing an increase in transmittance. Therefore, it is clear that minimizing the gap between the bottoms of the pillars will further increase the transmittance.
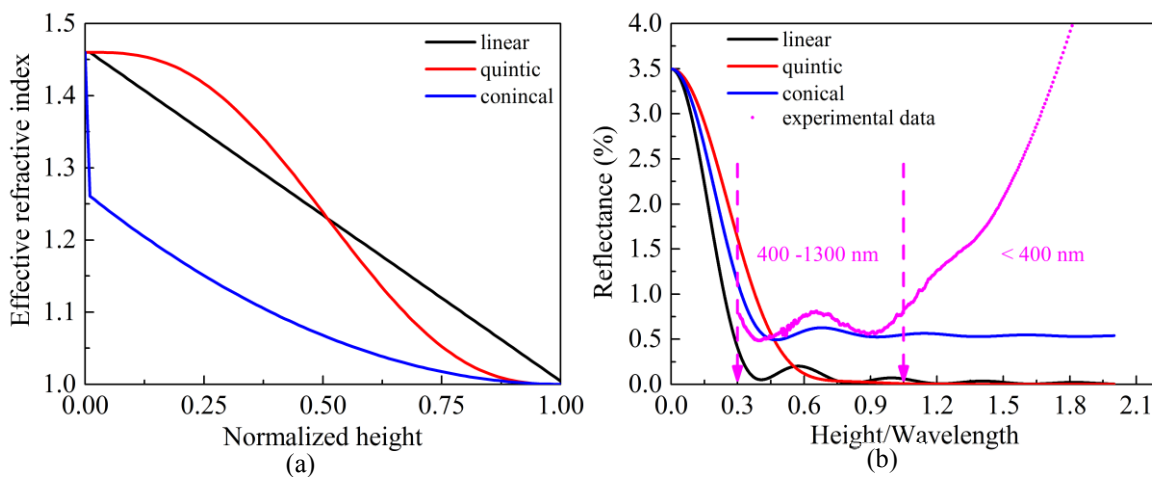
Figure 4-33: Optical property simulation of the nanopillar array by EMT theory. (a) the effective refractive index calculated based on the structure profiles. (b) The simulated reflectance based on thin film theory is plotted in solid lines, while the experimental results are plotted in dots. The x-axis is dimensionless height divided by the wavelength.

4.7.5   Interference occurs in nanohole array layer

The nanopillar/nanohole profile does not correspond perfectly to the model presented in Figure 4-32 (b), where the tip of the pillars and the intersection of the bottom of the pillars are not points in reality. The filling factors, *i.e.* refractive indices, at these two planes exhibit a discontinuity. Therefore, they behave like two parallel optical interfaces. This phenomenon can be observed for the imprinted nanohole structure (Figure 4-12 (b) and (d)) as well as the nanopillar structure (Figure 4-12 (a) and (c)). The imprinting process does not replicate the full pillar height, and the gap between the replicated nanoholes is larger. The nanohole arrays can be equivalent to an effective medium layer as shown in Figure 4-34. Due to the existence of the interfaces (top and bottom layer), the interference between them cannot be avoided. Such interference is also well-known as thin film interference [61,180]. The multiple reflections between the interfaces result in constructive and destructive interferences when the light

beams are in phase or out of phase. Whether it is constructive or destructive depends on the optical path difference, ΔL, defined as

$$\Delta L = 2n_{eff}d\cos\theta \qquad \text{(Equation 4-4)}$$

where n_{eff} is the refractive index of the effective medium layer, d is the thickness, and θ is the angle of incidence on the bottom interface as shown in Figure 4-34. Since the samples were measured with normal incident light beam, θ is zero. When the optical path difference equals to an integer multiple of the wavelength, constructive interference occurs; when it equals to an integer multiple of half of the wavelength, destructive interference occurs. As constructive interference occurs, it presents a strong reflection at the interface, thereby decreasing the transmittance. As destructive interference occurs, it reverses. In Figure 4-12 (b) and (d), constructive inference occurs first, showing a small valley in the spectrum at 400 nm wavelength (Figure 4-12 (b), pink curve) when the depth of nanohole is 200 nm. As the depth of the nanohole increases, the inference shifts to longer wavelengths of 550 nm (Figure 4-12 (d), green curve, 300 nm in depth) and 900 nm (Figure 4-12 (d), dark blue curve, 400 nm in depth). Each of the interferences occurs at the wavelength that is almost two times the depth, which is consistent with the theory mentioned above (Equation 4-4). The variation from exactly double the depth is due to the gradually changing effective refractive index, from 1.0 to 1.4 through the depth.

In theory, regardless of the interference, the deeper the nanohole, the higher the IPS® transmittance. However, in our case, there are always two optical interfaces existing that will produce the interference. At the desired wavelength, it will improve the AR effect if the destructive interference occurs. It will decrease the AR effect if the constructive interference occurs. By tuning the parameters, this effect can be well controlled.
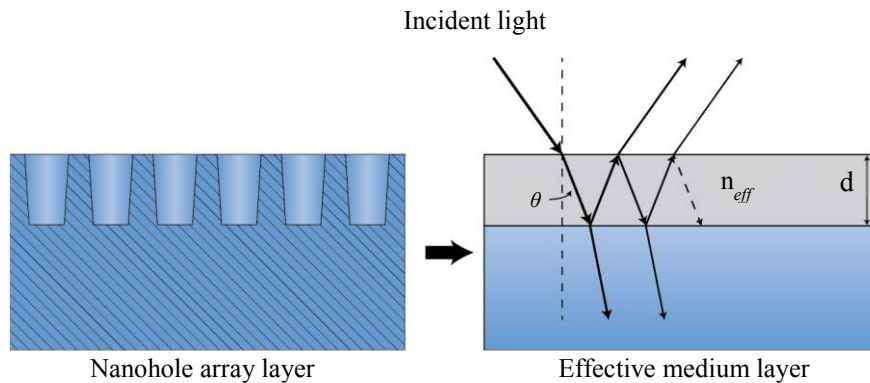
Figure 4-34: Nanohole array is equivalent to an effective medium layer. As the light beam goes through the medium layer, the light is reflected between the layer interfaces multiple times and the interference occurs.

4.7.6 Anti-reflection with single-sided and double-sided nanostructure

It is well-known that light is reflected twice at both sides of the substrate surfaces when it transmits through a transparent substrate. In this thesis, the boundaries between the surface

and the air will be referred to as either 'air/substrate interface' (top-side) or 'substrate/air interface' (bottom-side). In the experiments with one-sided nanopillar arrays (Section 4.2), the measured reflectance originated from both the nanopoillar interface and the interface without nanopillars. In other words, the reflection loss from the other interface without nanpillars still contributes in the measured spectrum. In order to exclude the non-nanopillar interfaces reflection loss, nanopillars on both sides of the substrate were prepared. Double-sided nanopillar surfaces on Suprasil® substrates have been successfully prepared by my colleague Dr. Zhaolu Diao, which I have extended onto polymeric substrates as was reported in the Section 4.4.3 and 4.5.1.

In order to determine the effect of the moth-eye nanopillar structure without the influence of the other interface, a mathematical approach was applied to exclude the reflection loss on the unstructured interface. It is assumed that the refractive index of the Suprasil® is homogenous over the measured wavelength (200 nm - 1500 nm) and equals to 1.46 (at 589.6 nm wavelength). The refractive index of the air is 1.0. Then, the reflection loss per interface is approx. 3.50% according to Fresnel's reflection (Equation 1-1) in the case of normal incident angle [181]. Since the incident light to the second boundary of the substrate/air interface is the transmitted light through the first air/substrate interface, there is some light reflected on the both sides, and the combined reflection loss is slightly different from 2R, *i.e.* $2R/(1+R)$. However, the difference is extremely small at 0.2%, thus it is assumed here that the reflection losses on both sides are the same. Therefore, out of a total 3.50% reflection per interface, 3.2% is transmitted by adding the nanostructured surface. In other words, with the 400 nm-height nanopillars, the transmittance of one single interface of the Suprasil® substrate (Figure 4-6, dark blue curve) can reach as high as 99.7%, and with 400 nm-height nanopillars on both sides of the substrate a total transmittance of 99.4% can be achieved. This was consistent with Dr. Diao's experimental results of double-sided nanostructured substrates and was also consistent with the simulation result in Figure 4-33 (dark blue curve).

Chapter 5   Bacterial attachment on nanostructured surfaces

5.1   Overview

Artificial nanopillar and nanohole arrays are inspired by nature, *e.g.* nanoprotuberance arrays were found on the surfaces of moth eyes [5] and insect wings [166,182]. In addition to the physical properties such as the anti-reflection property discussed in Chapter 4, the biological characteristics are of high interest. Anti-bacterial properties in particular are often studied. A study on cicada (*Psaltoda claripennis*) wings shows that the wings are covered by a hexagonal array of nanopillars with an average of 80 nm in diameter, 200 nm in height and 170 nm in interspacing distance having anti-bacterial properties, as the pillars are smaller than the bacteria and pierce and rupture the bacteria membrane, thereby killing them [116]. Anti-bacterial surfaces are in high demand in multiple applications, such as the surfaces of medical implants [78,183]. Sometimes both anti-reflective and anti-bacterial properties are needed simultaneously on the same surface, for example optical surgical instruments and electronic touch screens. Nanostructured arrays can provide the ability to combine these two properties. Moreover, the approach is physical and passive, which does not require the application of chemical drugs or any power input.

In this chapter, the fundamental behavior of bacterial adhesion to the nanopillar-structured surfaces of Suprasil® substrate is studied, providing further insights into developing a surface with anti-bacterial properties.

Selection of the bacterial species

Among the most common pathogens and organisms of foodborne illnesses identified by U.S. Food and Drug Administration (FDA) [184], *Escherichia coli* (*E. coli*) and *Staphylococcus aureus* (*S. aureus*) are two strains which were frequently studied by researchers. It is because they are the two typical types of bacteria representing the gram-negative (*E. coli*) and gram-positive bacteria (*S. aureus*). However, considering the limitations of our biological safety level 1 facilities at the MPI-IS, the *S. aureus* is not suitable for our studies; thus two similar bacteria from the same *Staphylococcus* genus but different species were selected, *i.e. Staphylococcus Sciuri subsp. sciuri* (*S. sciuri*) and *Staphylococcus Sciuri subsp. lentus* (*S. lentus*). Table 5-1 compares the main characteristic properties of *Staphylococcus aureus* and *Staphylococcus sciuri*. It is clear that the morphology, colony formation, catalase and metabolism are very similar.

Table 5-1: Comparison of the main characteristic properties of *S. aureus* and *S. sciuri*.

	S. aureus [185,186]	*S. sciuri* [187,188]
Morphology	Spherical or near spherical, 0.7-1.0 µm, in pairs and grape-like clusters, nonmotile, nonspore-forming, Gram-positive	Spherical, 0.8-1.2 µm, in pairs, singly and tetrads, nonmotile, nonspore-forming, Gram-positive
Colony form	Lemco agar, 37°C, 24 h, 0.5-1.0 mm, low convex elevation, smooth shining surface, entire edge, opaque; increase in size in diffused daylight at room temperature and be colored with rich cream or gold pigment.	P agar, 34°C, 5 days, 7.0-11.0 mm, moderately undulate edge, raised with slightly elevated center, smooth with glistening surface, opaque, gray-white with cream tint toward center
Catalase	Positive	Positive
Metabolism	Facultative anaerobe	Facultative anaerobe
Coagulase	Positive	Negative
Cell wall peptidoglycan	L-Lys-D-Glu-L-Lys-D-Ala-Gly5	L-Lys-L-Ala-Gly4
Cell wall teichoic acid	Polyribitol phosphate [189]	Glycerol and glucosamine
Biosafety level	S2	S1

All three bacteria species (*E. coli*, *S. sciuri* and *S. lentus*) were studied experimentally for their doubling time and morphology. One problem we discovered with the motile *E. coli* bacteria was that they did not attach to the surface when they were seeded on the Suprasil® surface (SiO$_2$, culture time: 20 min.). The other two bacteria, *S. sciuri* and *S. lentus,* belong to the same species, and were adherent. The doubling time of *S. lentus* was longer (60 min.) than *S. sciuri* (30 min.), and the former one often appeared in a tetrad morphology, which made the optical observation and coverage area statistics much more difficult than the single or pair form of *S. sciuri*. Therefore, *S. sciuri* was finally selected for the anti-bacterial experiments.

5.2   Bacterial growth assay and concentration measurement

For a quantitative evaluation of the adhesion results and reproducibility of the experiments, the bacterial concentration must be quantified and well-controlled. The pre-warmed bacterial culture (overnight in the shaker at 37°C with shaking speed of 220 rpm) was added to the autoclaved TSB medium at a 1:100 ratio. The optical density at a wavelength of 600 nm was recorded every 20 min. In parallel, 5 µL of the incubated bacterial culture was added to the hemocytometer to quantify the bacterial concentration. The recorded data is summarized in the curves shown in Figure 5-1, which reveals that the results obtained by the two methods are consistent, both showing the same exponential growth trend of the *S. sciuri* bacteria. In Figure 5-2, with the OD 600 data plotted on a logarithmic scale, the three well-known phases of bacterial growth are clearly shown. During the first 30 min, the growth of the bacteria was quite slow called the lag phase. Then, it was followed by an exponential phase that represents

fast exponential reproduction. Finally, the bacterial population reached to a stationary phase when the toxic metabolites accumulated and the medium was continuously consumed. The adhesion experiment was always carried out at OD600 = 0.2, which was the beginning point of the exponential phase and the bacterial concentration was approximately 0.2×10^9 mL^{-1}. The reverse of the slope of the exponential phase (red dotted line) in the log scale of OD600 (Figure 5-2) indicated that the doubling time of *S. sciuri* was around 30 min.
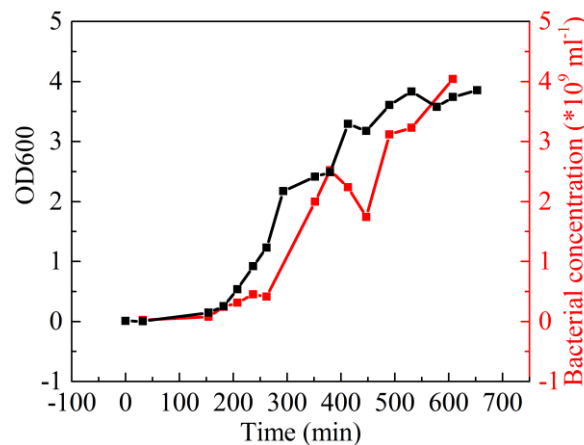
Figure 5-1: Growth curve of *S. sciuri*. The bacterial concentration was determined by two methods independently, *i.e.* optical density measurement and a hemocytometer, which showed a similar trend for the exponentially growth.
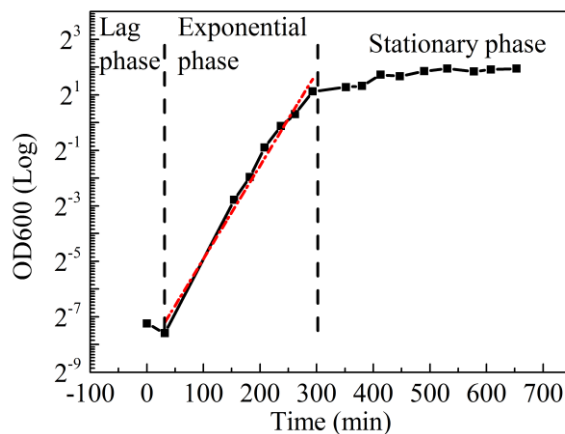
Figure 5-2: The growth curve of *S. sciuri* measured by OD600 and plotted on a logarithmic scale. The slope of the exponential phase is 0.03363±0.00181, thus the doubling time of the *S. sciuri,* which equals to the reverse of the slope, is approx. 30 min.

5.3   Influence of the surface chemistry on bacterial adhesion

5.3.1   Surface chemistry analysis via X-ray Photoelectron Spectroscopy (XPS)

As both nanostructure and chemical modification can significantly influence the bacterial behavior, XPS was utilized to analyze the surface elements and the chemical states of nano-

pillars after RIE treatment. Suprasil® samples were measured by Dr. Mitsuharu Konuma (Interface Analysis Group, Max Planck Institute for Solid State Research, Stuttgart, Germany).

A custom ultra high vaccum (UHV) system was utilized to measure our samples with a monochromatic Al Kα X-ray source (photon energy: 1486.65 eV). The basic principle behind XPS is the photoelectric effect [190], in which photoelectrons from the specific inner shell of the element are emitted due to the absorption of photons by electrons in the atoms when they are exposed to electromagnetic radiation of sufficiently short wavelength. Due to electron accumulation on the sample surface, charge compensation was performed on the insulated Suprasil® surfaces. The binding energy of collected photoelectrons is determined by measuring their kinetic energy according to:

$$BE = h\nu - KE - W \qquad \text{(Equation 5-1)}$$

where BE and KE are the binding energy and kinetic energy of emitted electrons, $h\nu$ stands for the energy of incoming photons and W means the work function of the solid. Elements were identified by examining their characteristic binding energies. After a determination of elements, the atomic concentrations of each single element was evaluated by CasaXPS software in order to quantitatively compare the samples before and after physical and chemical treatment.

To prepare the nanopillar array on the Suprasil® substrate, a RIE process is a necessary step to achieve a high aspect ratio of nanopillars. The etching gases used were Ar, SF_6 and CHF_3. Those chemicals could vary both the surface morphology of the nanopillar array and modify the surface chemical components of the Suprasil® substrate. It was also reported [87] that the surface chemistry variation could have a larger influence on the bacterial adhesion than the surface topography. Therefore, before studying the influence on nanopillar arrays, the surface chemical composition was investigated first.

Three Suprasil® samples were prepared using different methods and their surface compositions were compared. One sample was used as a reference, which was only thoroughly cleaned with CARO and named as "Ref.". The other two samples were both subjected to an RIE treatment of 6 cycles. One of these two samples was named as "RIE", while the other one was further treated with intensive H_2 plasma in order to remove the chemical layer formed during the RIE process and named as "RIE+clean". The chemical components of these three samples were analyzed by XPS measurement and summarized in Figure 5-3 (a). The atomic concentration was extracted to Table 5-2 from the scanning of each single element peak.

In Figure 5-3 (a), comparing the RIE sample (red curve) to the reference sample (black curve), it clearly shows the presence of Fluorine element (F 1s at BE: 687 eV) with relative atomic concentration of 26.0%, and very weak signal of both Magnesium (Mg 1s at BE: 1305.1 eV) and Aluminum (Al 2p at BE: 76.2 eV). After the cleaning process by plasma treatment (blue curve), both Mg and Al were completely removed and F was significantly decreased down to 2.91%. The Al element probably originated from the Al-made lid of the

etching chamber. The Mg was extremely low in content and it probably originated from the residual impurity of the chamber that was often used for etching different kinds of substrates. The F portion was zoomed in for a composition analysis as shown in Figure 5-3 (b). The F peak was split into two sub-peaks of 687.5 eV and 686.5 eV, which are the two binding energies for SiO_xF_y [191] and C_xF_y [192].
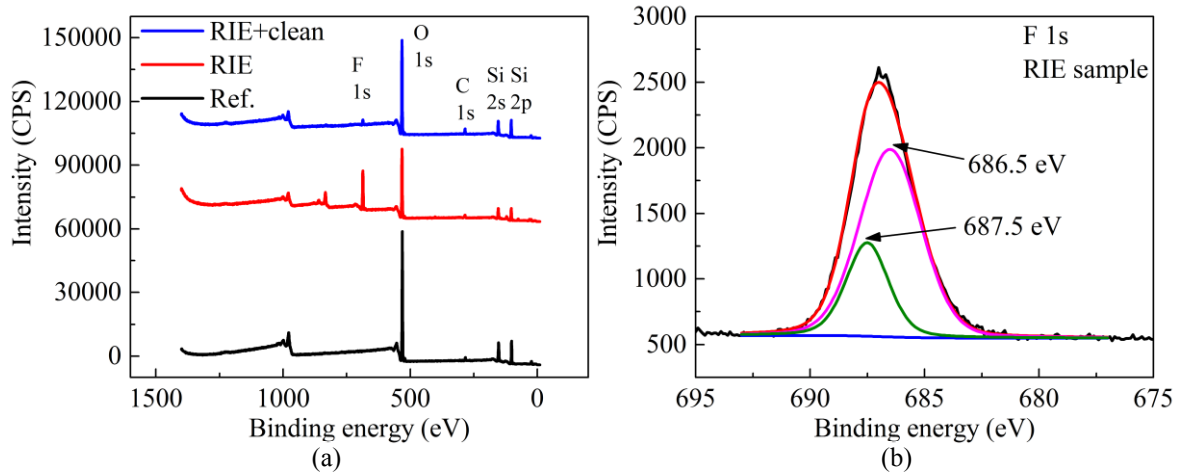
Figure 5-3: XPS measurement of the Suprasil® substrates: reference sample (Ref., black curve), RIE treated sample (RIE, red curve) and both RIE and H_2 plasma treated sample (RIE+clean, blue curve). (a) Whole spectrum (b) Splitting of the fluorine peak.

Table 5-2: Quantitative atomic concentrations for every measured element on the three substrates in the binding energy scanning from 1400 eV to 0 eV.

Samples	Mg	F	O	N	C	Si	Al
Ref.	-	-	69.1%	0.22%	4.22%	26.46%	-
RIE	0.14%	26.07%	42.85%	0.75%	8.95%	16.02%	5.23%
RIE+clean	-	2.91%	55.01%	0.31%	8.45%	23.81%	0.37%

5.3.2 Bacterial attachment on modified surfaces

With a comprehensive understanding of the surface chemistry, the bacterial experiment was begun by seeding *S. sciuri* on the three samples, *i.e.* "Ref.", "RIE" and "RIE+clean". For each group, the experiments were independently repeated three times with new samples. The pre-warmed *S. sciuri* culture was mixed with TSB medium at a ratio of 1:500 and shaken continuously in an incubator at 37°C. When the culture reached an OD600 = 0.2, 2 mL of the *S. sciuri* culture was added into each well of a 6-well plate where the samples were immersed. They were then measured by inverted microscope after the plate was put back into the incubator for 20 min.
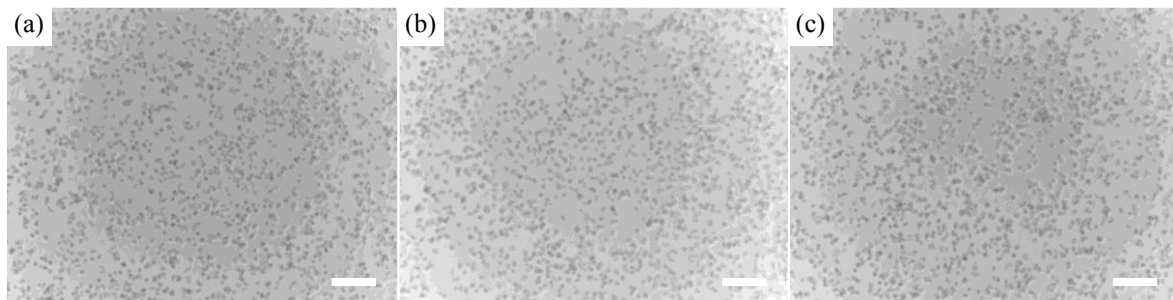
Figure 5-4: Phase contrast images of the *S. sciuri* bacteria on samples of a plain surface (a), RIE treated surface (b) and RIE+H_2 plasma treated surface (c). Scale bars: 25 µm.

Figure 5-4 presents the phase contrast images of the *S. sciuri* bacteria on each sample and Figure 5-5 shows the statistical analysis of the percentage of bacterial coverage area. Although the mean values of the two groups with RIE treatment are lower than that of the reference group, the error bar of each percentage is large; thus the one-way ANOVA test was carried out on the three groups. The *S. sciuri* coverage of these three samples showed no significant difference, given F<0.05 is considered significant. This result indicates that the residues of SiO_xF_y and C_xF_y generated during the RIE process do not significantly influence the adhesion of *S. sciuri*, and an additional plasma cleaning process would not be necessary for bacterial tests in the future.
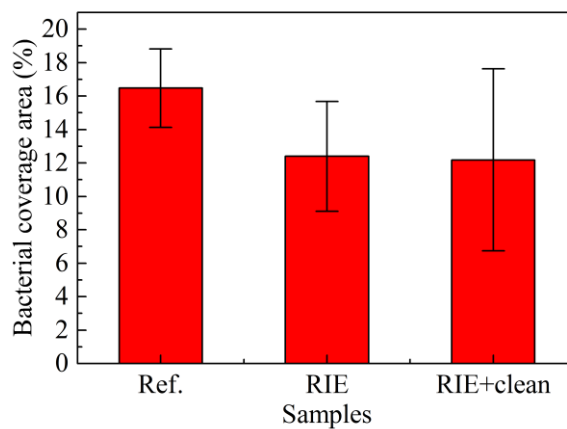
Figure 5-5: *S. Sciuri* coverage area in percentage. There is no significant difference (F>0.05) among the three samples, *i.e.* "Ref.", "RIE" and "RIE+clean", after a culture time of 20 min.

5.4   Influence of nanopillars on bacterial adhesion

In this section, *S. sciuri* adhesion tests were carried out on the surfaces with and without nanopillar structures. Two samples were used, with one being the "Ref." sample as the control group and the other one being the nanostructured sample with nanopillars of 70 nm in diameter, 90 nm in inter-pillar spacing and 300 nm in pillar height. The bacterial adhesion tests were carried out in the same manner as the last experiment discussed in the section above.

Figure 5-6 shows the summarized coverage percentage of *S. sciuri* on these two substrates. By the application of a statistical *t*-test, there is no significant difference between the two groups (P>0.05).
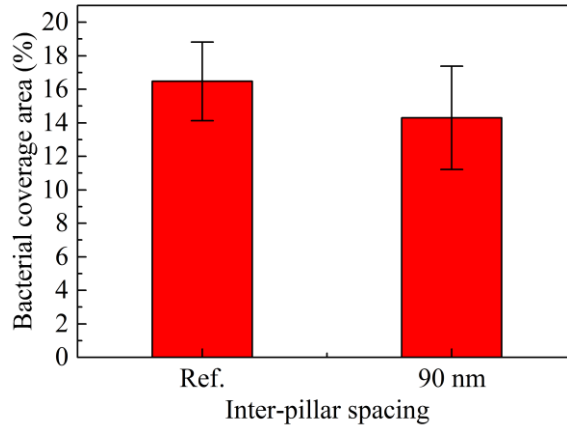
Figure 5-6: *S. Sciuri* coverage area on samples with/without nanostructures. No significant difference (P>0.05) is observed for the bacteria attachment on the surface with nanopillars (70 nm-diameter, 90 nm-spacing and 300 nm-height) compared to the plain Suprasil® substrate as a reference group (Ref.) after 20 min culturing time.

5.5 Influence of varied inter-pillar spacings on bacterial adhesion

In the last section, a negative result was observed for a potential anti-adhesion behavior of *S. sciuri* on the nanopillar-structured surface. However, to confirm this result and to check whether this would change when the period of the pillar array was varied, a parametric sweep of the inter-pillar spacing was carried out in this section. This group contained four samples, one was the control sample (Ref.) and the other three samples were covered with nanopillars of different inter-pillar spacings, *i.e.* 50 nm, 90 nm and 130 nm., and a fixed height of 300 nm. *S. sciuri* was brought in contact with the substrate surfaces and kept in the incubator for 40 min, which was longer than the former experiment. The bacterial coverage percentage on the top surface of the substrate was recorded by choosing three random positions under the microscope. Before analyzing the bacterial attachment, the surface energies of these four samples were studied and evaluated on another batch of samples prepared by the same procedure.

5.5.1 Surface energy measurement of the Suprasil® substrate surfaces

The surface energy was calculated based on contact angle measurements. The relationship between contact angle and surface energy is governed by Young's equation [132]:

$$\gamma_{lv} \cos\theta = \gamma_{sv} - \gamma_{sl} \qquad \text{(Equation 5-2)}$$

where γ_{lv}, γ_{sv} and γ_{sl} are surface energy of the liquid-vapor, substrate-vapor and substrate-liquid. θ is the measured contact angle. θ and γ_{lv} can be readily measured, and the values of γ_{lv} are documented in the literature [137]. The other two parameters γ_{sv} and γ_{sl} are still unknown and need to be related. Two different approaches were reported to determine the γ_{sv}

[193]. The first method called "equation of state" was empirical and did not show a good consistency with the experimental results. Therefore, the second method called "surface tension components" was adopted here. An equation was used here describing the relationship of the surface tensions when only the dispersive action is included [193]:

$$\gamma_{sl} = \gamma_{lv} + \gamma_{sv} - 2\Phi(\gamma_{lv}\gamma_{sv})^{1/2} \qquad \text{(Equation 5-3)}$$

where the constant Φ is normally determined experimentally and it is often close to 1 [193]. Hence, combing (Equation 5-2) and (Equation 5-3) yields (Equation 5-4).

$$\cos\theta = 2\Phi\sqrt{\gamma_{sv}}\frac{1}{\sqrt{\gamma_{lv}}} - 1 \qquad \text{(Equation 5-4)}$$

By plotting $\cos\theta$ versus $1/\gamma_{lv}^{1/2}$, the slope should be equal to $2(\gamma_{sv})^{1/2}$. Then, the value of γ_{sv} can be calculated.

There were four Suprasil® samples prepared for surface energy measurements. One is the referenced planar sample cleaned by CARO, and the other three were samples with nanopillar arrays on their surfaces giving varied inter-pillar spacing, *i.e.* 50 nm, 90 nm and 130 nm. The pillar height of 300 nm was kept the same between samples, *i.e.* the same RIE etching cycles were applied. Samples were prepared a week before the measurement was performed, therefore the unstable –OH group generated by CARO solution on the reference sample was considered negligible. Only dispersive action was considered during the measurement. Contact angle measurements were performed with three liquids with different liquid-vapor surface tension γ_{lv}, *i.e.* 72.8 mN/m of water (distilled water), 47.7 mN/m of ethylene glycol (EG) and 22.1 mN/m of ethanol [137]. The measured contact angles are summarized in Table 5-3.

Table 5-3: Contact angle measurement on Suprasil® substrate with/without nanopillars. The pillar height was kept constant at 300 nm and the inter-pillar spacing varied, *i.e.* 50 nm, 90 nm and 130 nm.

Liquid	Reference	50 nm-spacing	90 nm-spacing	130 nm-spacing
Water	51.9°±1.2°	<5°	<5°	<5°
EG	31.7°±0.8°	<5°	<5°	<5°
Ethanol	<5°	<5°	<5°	<5°

The contact angle of the reference sample decreased gradually as the surface tension of the liquids decreased, however, the nanostructured samples all showed a complete wetting phenomenon with contact angles smaller than 5° wtihout significant differences. In order to identify the surface energy of the reference sample, the $\cos\theta$ was plotted versus $(1/\gamma_{lv})^{1/2}$ (Figure 5-7). The surface tension of the Suprasil® substrate was about 43.5 mN/m, which was consistent with the value reported by Bartle *et al.* [194]. The contact angle of the substrate with nanopillars was much less than 5° and by this technique it was difficult to evaluate the specific value. However, it provided a quantitative understanding that the surfaces were superhydrophilic and the surface tension should be much larger than that of the planar Suprasil® substrate (43.5 mN/m).
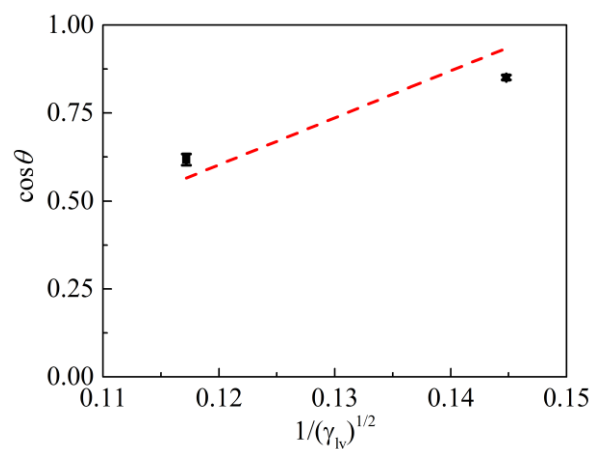
Figure 5-7: Surface energy calculations of the planar Suprasil® substrate. The dotted line was fitted according to (Equation 5-4), and its slope equals the $2(\gamma_{sv})^{1/2}$, thus the surface energy of the planar Suprasil® is derived as 43.5 mN/m.

5.5.2 Bacterial attachment on nanopillars with varied spacings

Samples seeded with *S. sciuri* were incubated for 40 min. Figure 5-8 shows the statistical results. Although both the incubation time and coverage were increased two-fold (16%-30%) from the last experiment, the adhesion of *S. sciuri* did not show any statistical significant difference compared with the control group by an one-way ANOVA (F>0.05).

The coverage area of the bacteria on the surface after 20 min. culture time was already high, and after 40 min., the surface was observed to be full of bacteria under the microscope. Although the bacterial test revealed a negative result on the influence of the adhesive property of the nanostructure, it was only restricted to this one strain of gram-positive bacteria. They consist of a thick peptidoglycan layer on the outside [195], which might be the reason that the nanopillar structures did not affect the adhesive property of this kind of bacteria. Another possible reason was that the geometry of the nanostructures was not appropriate for killing the bacteria compared to the bactericidal black silicon nanopillars prepared by Ivanova *et al.* [116].
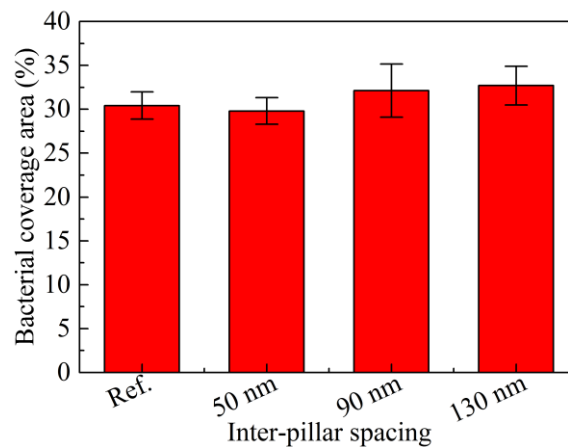
Figure 5-8: *S. sciuri* coverage area on samples with different inter-pillar spacing. The plain Suprasil®
substrate cleaned by CARO was taken as a control group (Ref.) and the other samples were prepared
with nanopillars of 50 nm-, 90 nm- and 130 nm-spacing. All nanopillars were 300 nm in height. No
significant difference (one-way ANOVA, F>0.05) was observed for the bacteria adhesion on the sur-
face among the groups after 40 min culturing time.

5.6   SEM Observation of *S. sciuri* adhesion on sample surfaces

In order to better understand the local interaction and adhesion of *S. sciuri* with the substrate
surface, SEM combined with the critical point drying method was applied to gain a direct
visualization of the adhesion sites.

Samples were prepared in the same manner as above mentioned with *S. sciuri* bacteria, *i.e.*
pre-warmed, cultured and seeded for 20 min. After that, a PFA fixation method was applied
to kill the bacteria and maintain the morphology of the bacteria and the adhesion sites to the
surface. After fixation, samples were rinsed with PBS thoroughly and followed by graded
ethanol dehydration. By using the critical point drying, the morphology of the bacteria was
retained. After coating with a carbon layer, it could be readily mounted for observation under
SEM.

SEM images in Figure 5-9, Figure 5-10 and Figure 5-11 clearly show the contact area be-
tween *S. sciuri* and the substrate surface. The order of the samples in each of the figures cor-
responds to the statistical analysis result in Figure 5-5, Figure 5-6 and Figure 5-8 as discussed
above.

In the SEM the substrates treated with RIE showed a nano-scale roughness (Figure 5-9 (b)
(c)) and the substrates with nanopillars presented a varied inter-pillar spacing as designed
(Figure 5-11 (b) (c) (d)). *S. sciuri* appeared spherical with a diameter of approx. 1 μm. They
preferentially arranged mainly in pairs and sometimes in tetrads or as individual cells. It was
observed that there was some polymer matrix between the bacteria and the surface, which
extended to cover the bacteria, as shown clearly in Figure 5-11 (b). The film in Figure 5-11
(b) was accidently torn probably due to the sample preparation before SEM in either the de-
hydration or the drying process. Such polymer matrix could be likely the basis of a beginning
of the biofilm formation [101]. In Figure 5-11 (c) and (d), some nano-fibers were also ob-

served connecting the bacteria and the nanopillars (circled by red squares in Figure 5-11 (c) and (d) and zoomed in (i)-(iv)). These fibers were never detected in control samples and could be nano-fimbriae, which were also described by Schmidt *et al.* for *S. saprophyticus* [122]. Additionally, these fibers were clearly observed with the increasing spacing of the nanopillars, and they tend to attach to the tip of the nanopillars instead of to the bottom or the space in between. Thus, it is a reasonable assumption that these fibers are fimbriae being probably used for the surface sensing and attachment. Because the contact area is much smaller for the bacteria on the nanopillar surface compared to that of a plain surface, these nano-fibers most likely assist in the formation of a firm adhesion of the bacteria to the surface, similar to ropes that are used for fixing a tent.
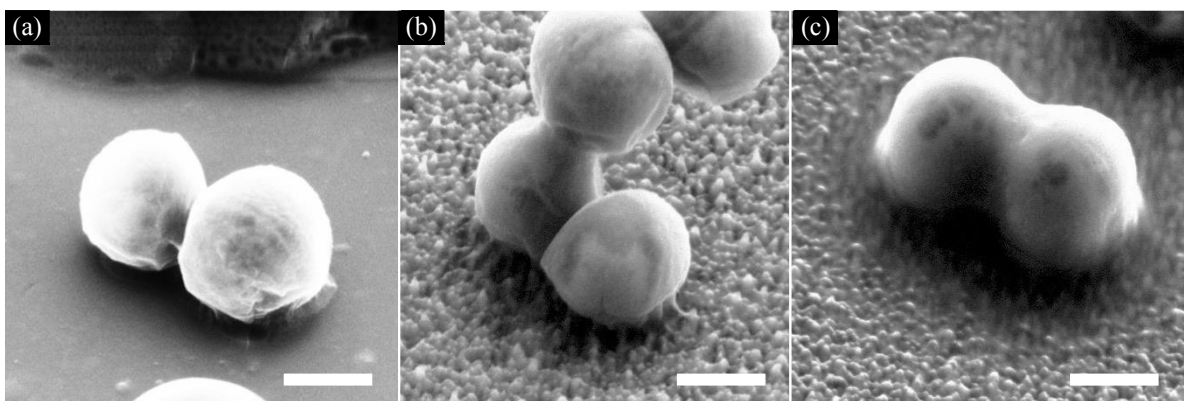
Figure 5-9: SEM images of *S. sciuri* attached to different Suprasil® surfaces. The plain Suprasil® substrate is taken as the control group (a). Both (b) and (c) are plain Suprasil® substrates (without Au nanoparticles), treated with RIE. (c) was additionally exposed to H_2 plasma treatment. Shallow nanostructures are observed on the surfaces in (b) and (c). The surface chemical composition corresponds to the surfaces shown in Figure 5-5. Culture time of the bacteria: 20 min. Scale bars: 600 nm.
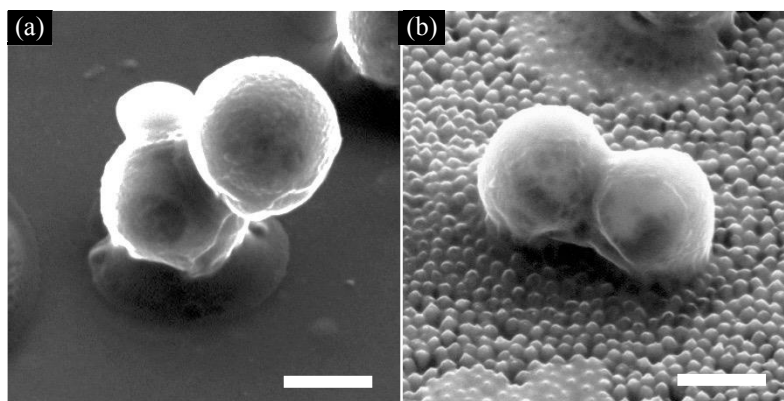
Figure 5-10: SEM images of *S. sciuri* attached to different Suprasil® surfaces. (a) The plain Suprasil® substrate is taken as the control group. (b) The substrate with nanopillars of 90 nm-spacing and 300 nm-height. The two pictures are two examples corresponding to the statistical results in Figure 5-6. Culture time of the bacteria: 20 min. Scale bars: 600 nm.
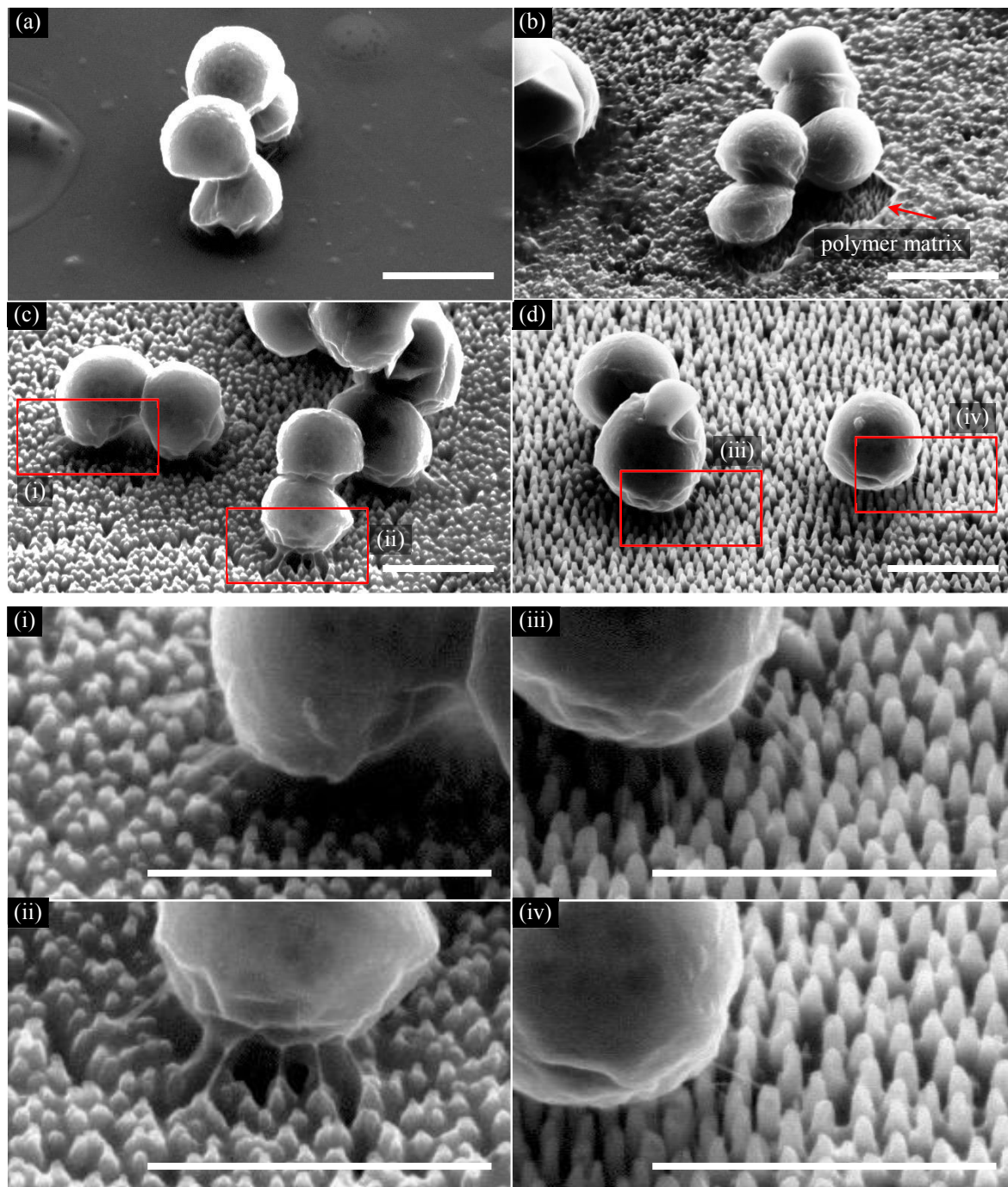
Figure 5-11: SEM images of *S. sciuri* attached to nanopillar surfaces with different inter-pillar spacing of 50 nm (b), 90 nm (c) and 130 nm (d), respectively. The heights of the pillars were kept the same around 300 nm. (a) The plain Suprasil® substrate was taken as the control group. The pictures are examples corresponding to the statistical results as shown in Figure 5-8, but with 20 min culture time. Four positions circled by red squares in images (c) (d) are zoomed in and shown in (i) (ii) (iii) and (iv). Scale bars: 1 μm.

More SEM images are provided in the appendix (Figure 6-6). As the morphology change in terms of nano-fibers most likely fimbriae of the bacteria was observed in SEM, the adhesion

mechanism is probably different for nanopillar surfaces compared to plain surfaces. The biological mechanism behind this process is still unclear and has to be investigated further; however, the methods for preparing nanostructured surfaces developed in this thesis provide an approach to alter the bacteria adhesion mechanism, thereby allowing for further studies of the adhesive biological mechanism on nano-topological surfaces. This may ultimately lead to the creation of an effective anti-adhesive surface.

5.7   Discussion

5.7.1   Comparison of the non-structural and structural anti-bacterial methods

The approaches of preventing a bacterial attachment to surfaces can be categorized into two kinds: non-structural and structural methods. The former method has been extensively studied and applied. For example, researchers develop locally-released antibiotic therapies [196], drug delivery approaches [197] and surface coating methods [198]. However, two common problems of these methods are: 1) the anti-bacterial effect is transient and only has short durability until the drug is fully released; 2) the bacteria may develop a resistance to the drug, which can cause severer problems for the medical therapies.

Another popular non-structural approach is the use of silver. It was known for a long time, that silver can be used as an anti-microbial agent for burns and chronic wounds [199]. Due to the emergence of penicillin [200], the use of silver was minimized. However, as mentioned above, it was recognized soon that the extensive use of antibiotics had a big problem of inducing bacteria resistance. Recently, silver nanoparticles have emerged with diverse medical applications [98,100,199], *e.g.* silver ion solutions [84] were studied by culturing the *S. aureus* and *E. coli*. The reduction of both bacteria was confirmed by conventional plate counting. Ag-doped SiO_2 thin films were also found to have an efficient anti-bacterial effect by reducing the attachment of *S. aureus* and *E. coli* [201]. However, the silver toxicity is still unclear. Silver nanoparticles are normally suggested to be non-toxic, but it still shows a toxic effect when the wound is in a large area and a large volume of the silver dressing is used [199]. Hussain *et al.* [202] studied the side effect of silver nanoparticles with varied sizes on a rat liver cell line. The cells were found to change in size and shape.

All these disadvantage of non-structural methods have resulted in a more intensive development of structures with anti-bacterial properties. Compared to the non-structural methods, the structural (topological) methods do not require any special chemicals, instead they utilize the designed micro/nano-structures on the surface to prevent bacterial attachment. These methods are non-toxic, have a long durability and do not result in a drug resistance; moreover, only the surface topology is modified and the bulk material properties (*e.g.* tensile strength, elasticity) remain unchanged [87,203]. The AB structures can be divided into three categories according to their feature size comparing with the size of the bacteria: 1) When the distance between the features is much larger than the bacteria dimensions, there will be little cell-structure interactions and the cells will only encounter the smooth surface in-between the features [107]. 2) When the feature size is similar to the scale of an individual bacterium, the

cell will sense the topological structure. If the gap between the structures is smaller than a bacterium can fit in, it provides steric resistance to the bacterial attachment thus it can serve as an anti-fouling structure, *e.g.* Sharklet[TM] structure [204,205]. 3) When the structure dimension further decreases, it becomes much smaller than the size of the bacteria that is in the nanometer regime. Due to the difficulty and limitation in fabrication and observation methods, few studies were carried out in this regime, and contradictory results were reported [206,207].

The *S. sciuri* in this thesis showed no significant difference in the adhesion to flat or nanopillar-structured surfaces statistically (Figure 5-5, Figure 5-6 and Figure 5-8). In order to explain the reasons of this phenomenon, nanostructures with AB properties reported in the literature are compared. For example, Xu *et al.* [206] reported an anti-bacterial adhesion surface made of poly(urethane urea) material. Two kinds of pillars, *i.e.* the diameter, diagonal distance and height were 420 nm, 715 nm, 700 nm and 530 nm, 870 nm, 650 nm, respectively. Both kinds of structures lead to significant reductions in adhesion of both bacterial strains (*S. epidermidis* and *S. aureus*) under low shear stress conditions [206]. The other example is the nanopillar array on cicada (*P. claripennis*) wings [112], *D. bipunctata* wings and artificial black silicon materials [116] that were reported with bactericidal properties for a wide range of Gram-positive (*S. aureus*), Gram-negative (*P. aeruginosa*) bacteria and endospores (*Bacillus subtilis*). Different from the anti-adhesion mechanism, which has the goal of minimizing the contact area of the bacteria and the substrate, this bactericidal approach used the physical interaction forces to rupture the cell membrane and lead to cell deformation and subsequent cell death. The pillars on black silicon are mainly composed of Si, have a diameter of 20-80 nm (mostly below 30 nm) and a height of 500 nm. Noticeably, both the shapes and the positions of these pillars are randomly distributed and the tips of the pillars are pretty sharp, even sharper than the natural ones on the dragonfly wings [116].

The chemical composition of the nanostructured surface in this chapter was measured and controlled to be as similar as possible to the planar surface, since it is known that bacterial adhesion is also influenced by the chemical composition [87]. However, in the above-mentioned papers [116,206,207], the specific chemical composition of the surfaces was not reported and the information was unavailable for comparison between the nanostructured and the planar surfaces. Previous work suggest that nanofabrication process can readily induce differences in surface chemistry and surface energy [87]. For example, the surface energy and wettability significantly change when the glass surface was prepared with nanostructures [208]. Extra chemical elements and substances appeared on the surface, which originated from the reaction with etching gases during the RIE process [209,210]. Moreover, during the nanoimprinting or hot embossing, the anti-adhesive layer, *e.g.* PTFE, was observed to be transferred from the mold surface to the polymer surface under pressure and high temperature [211]. Therefore, it is unclear in the above-mentioned studies whether the surface nanostructure or the surface chemistry is the main reason that leads to the AB properties.

The nanopillar array used in this chapter is made of SiO_2 material, had a tunable spacing range from 50 nm to 130 nm (Figure 3-10) and a tunable height from 50 nm to 400 nm (Figure 3-2). Compared to the above-mentioned structures, it was far away from the poly(urethane urea) pillars [206], but similar to the size of the cicada wings and black silicon protuberances [112,116]. However, there are two significant differences of our nanopillars from the black silicon nanostructure: 1) The array was arranged in a hexagonal order, while the black silicon pillars were randomly positioned; 2) The pillar had a rounded tip with a hole in the center (Figure 3-2, Figure 3-10 and Figure 3-16) but not a sharp tip as the pillars of the black silicon. These can be the possible reasons for our contradictory findings. Moreover, independent from the parameters of the nanostructures (*e.g.* feature size, regularity and shape), the bacterial behavior differs largely depending on the strain of bacteria (*e.g.* Gram-positive or Gram-negative) [212] as reported in the literature. Although the *S. sciuri* bacteria we used is from the same genus as the *S. areus* strain used by Ivanova *et al.* [116], they are still different species. This could also be an explanation for our contradictory results. As microorganisms vary a lot in their shape, size, surface composition and appendages, it will not be possible to develop a single kind of structured surface that is resistant to all kinds of bacterial attachment. The anti-bacterial adhesion and bactericidal effects need to be studied individually according to the specific bacterial strain on the given nanostructured surfaces.

5.7.2   Discussion on the experimental procedures

Sample preparation is a critical step for SEM observations. In the previous papers studying the morphology of bacteria on the etched glass with nano-roughness [213], cicada wings with nanopillars, and black silicon substrate with high aspect-ratio nanoprotrusions [116], the bacteria attached to the nanosurface were observed by SEM. The SEM images showed that the cell membranes were severely disrupted by the nanofeatures [116]. However, the samples were prepared with the following step "after incubation all of the slides were washed with deionized water and left to dry" [213]. This is a controversial step as washing with DI water and leaving the bacteria to dry in air may severely alter the cell morphology. Especially when they are in contact with nanostructures on the surface, the consequences are even more unpredictable. Therefore, in the experiments reported in this chapter, special attention was paid to the sample preparation process.

The bacteria samples used in this thesis went through three subsequent steps before SEM imaging: fixation by PFA, graded ethanol dehydration and finally critical point drying, in order to keep the bacteria cell morphology as natural as possible for the observation in SEM. The SEM images Figure 5-9 showed that *S. Sciuri* is in a spherical shape and preferably organized in paired or tetrahedral formations, which is consistent with the observations by microscopy (Figure 5-4). Thus it is confirmed that the cell morphology is unchanged. Detailed structures, such as the thin nano-fimbriae (smaller than 5 nm in diameter) are clearly visible (red squares in Figure 5-11), which also suggests that the morphology of the bacteria attached to the surface is well preserved. Hence, the method established in this chapter provides a

general method to study the bacterial response on nanopillar-structured surface, and may lead to some insight of the bacterial adhesion mechanisms at nanometer scales.

5.7.3 Discussion on the structures of the cell wall interacting with nanopillars

The bacteria used in this thesis, *S. sciuri*, is a Gram-positive bacteria, which has a thick peptidoglycan layer in the cell wall [195] and it makes the cell very rigid to be deformed. These kind of bacteria often rely on the structures on their cell wall (fimbriae, pilli, flagella) to sense and interact with the nano-scale features [117,214,215]. This phenomenon was experimentally confirmed in this thesis. Under SEM observation Figure 5-11 (b, c, d), it was clear that the shape of the *S. sciuri* was spherical and showed no significant deformation of the cell either on a flat or on a nanopatterned surface. However, thin and long fibers most likely fimbriae were observed connecting the bacteria and the top of the nanopillars as depicted in Figure 5-12. This cellular structure was only observed when they were attached to the nanopillar structures but not on the flat surface. This was probably due to the contact area being dramatically reduced for the bacteria from a flat surface to the nanopillar array, and additional fibers/fimbriae were formed to fix the bacteria to the pillar top for a firmer attachment between the surfaces. Similar phenomena were also reported by other researchers. For example, Svensson *et al.* [216] observed the cross-sections of *S. epidermidis* attached to the nanostructured and smooth gold surface using the focused ion beam (FIB) slice and SEM. The bacteria was only attached by a few discrete points on the nanostructured surfaces, which had a far lower contact area compared to a flat surface. Najafinobar *et al.* [217] fabricated gold nanoparticles with a diameter of 20-30 nm on the surface and, similar to the results reported here, nano-fimbriae structures were observed only on the nanoparticle surface, but not on the flat surface.
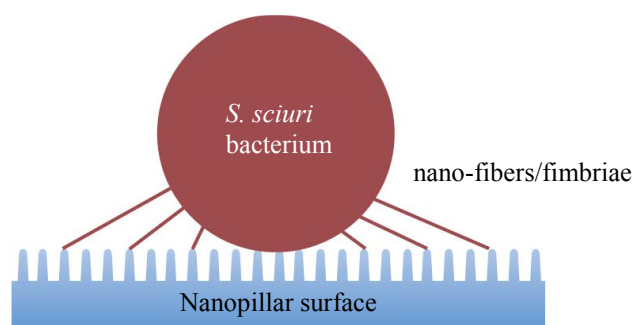
Figure 5-12: Sketch of bacteria-substrate interaction.

In summary it was shown, that the nano-scale topography of the surfaces created in this thesis had an influence on the morphology in terms of emerging nano-fibers, but there was no anti-bacterial properties detected as reported before for similar structures. This might be due to difference in the exact dimensions and shapes of the used nanostructures, but also to experimental set-ups (including bacterial strains and sample preparation). Moreover, based on the surface chemistry discussion in Section 5.7.1, the chemical composition was not compared before and after nanofabrication in listed works [116,206,207], so it is not clear yet whether the nanostructures or the surface chemistry is responsible for the reported anti-

bacterial properties. However, the created surfaces herein are tunable and also the shape of the nanopillars can be changed, so that future work can be carried out to explore the bacteria attachment mechanism to the nano-topological surfaces leading to a deeper understanding of the bacterial mechanotransduction mechanism. There is also room to improve the surfaces and to finally gain a surface with antibacterial and excellent anti-reflective propertie as shown in Chapter 4. This would improve the performance of a wide range of devices and to reduce their fabrication costs.

Chapter 6　　Summary and outlook

6.1　　Summary

6.1.1　Summary of nanostructure fabrication

In this thesis, the semi-hexagonal nanopillar arrays were successfully prepared on fused silica substrates (Suprasil$^®$) combining the bottom-up BCML technique and the top-down RIE process. Various dimensions of the nanopillars were realized, specifically the height and the inter-pillar spacing were adjustable in the range of 50-400 nm and 50-130 nm, respectively. It was experimentally verified that the height depended on both the polymer chain length and RIE cycle; while the spacing was a function of polymer chain length, concentration and spin coating speed. As the polymer chain length was a variable for both parameters, if the height and the spacing need to be adjusted independently, then the polymer chain length should always be kept constant.

The nanopillar arrays were also successfully fabricated on other kinds of inorganic materials, such as borosilicate, sapphire, stainless steel and SF10, by depositing an extra intermediate layer of SiO_2 on the surfaces of the other substrates. Thus, without changing the preparation recipe for the nanopillars, nanopillar structures could be fabricated on different kinds of materials and their material properties could be exploited. Since the hierarchical nanopillar formation was based on the build-up of the passivation layer, the thickness of the deposited SiO_2 layer should always be thicker than that of the expected nanopillar array. Experimentally a SiO_2 layer sputtered with a one-third larger thickness resulted in the expected nanopillar height after the RIE process.

The replication of the nanostructures into polymeric substrates was carried out by two methods, *i.e.* replica molding and nanoimprinting. The nanoimprinting outperformed the replica molding, as it resulted in nanostructures with better fidelity, more homogeneous overlarge areas and a faster process. Nanohole arrays were successfully replicated from the mold with the nanoimprinting technology on IPS$^®$ polymer sheets. The tendency of the optical transmittance showed a good consistency with that measured from the fused silica molds as the nanopillar dimensions (height and inter-spacing) change. Thus, the results suggest that the nanoimprinting technique replicates the nanostructures from the mold with good fidelity.

Due to the optical transparency and high biocompatibility of PMMA, it is often used as material for contact lens and other biomedical applications. Therefore, a second step of the nanoimprinting procedure was conducted on PMMA substrates. Due to the difference in the

glass transition temperature between IPS® and PMMA, the imprinted IPS® with a nanohole array was used as the mold for the second imprinting step of PMMA. The nanopillar structures were successfully replicated homogenously with a large surface area on either single side or double sides of the PMMA. This imprinting method is a fast and a cost-effective approach, as the prepared nanostructured mold could be repeatedly used for at least eight times for imprinting processes under high pressure and high temperature. Furthermore, a designed curvature and the nanopillar-structured surface could be imprinted into the polymeric material through a single-step nanoimprinting process, which will be beneficial for the fabrication of high-performance contact lenses and intraocular lens.

6.1.2   Summary of the anti-reflective (AR) properties

Excellent AR properties on both organic and inorganic substrates were realized by the nanostructured surfaces, *i.e.* pillar and hole arrays. The AR performance of the Suprasil® substrate was effective in a wide wavelength range of 200-1000 nm and reached a maximum of 99.5% per interface when the pillar height was 400 nm and the inter-spacing was 100 nm. The AR properties were tunable by changing the nanostructure dimensions. As expected, the increment in pillar height or the decrement in inter-spacing leads to higher transmittance, and the increment in pillar height also resulted in the shift of the transmittance peak towards larger wavelengths. By modeling the hierarchical nanopillar structures into a semi-conical shape, the simulated transmittance of the Suprasil® substrate according to the EMT theory matched the experimental results well.

Nanostructured surfaces also significantly improved the transmittance of polymeric substrates. The imprinted nanohole arrays successfully increased the transmittance of IPS® substrates from 91.5% to 95% with 300 nm in depth and 50 nm in diameter at the wavelength of 1000 nm. The measured transmittance of the double-sided imprinted PMMA with nanopillars reached as high as 97.5%, which was approximately a 6% increment compared to the original PMMA substrate, and even 4% higher than a fused silica grade Suprasil® substrate. The transmittance measured on the PMMA also exhibited excellent AR properties even at large incident angles (a transmittance of 91% at 60°).

In summary, the nanostructured surface provided an effective way for AR covering a wide range of wavelengths from UV to infrared. The major advantages of this approach over the traditional thin-film coating included a large range of incident angle, high thermal stability and a wide choice of materials. Nanoimprinting is a fast, reliable and cost-effective method to replicate nanostructures in polymeric materials that are light, flexible and biocompatible, thus it could lead to a lot of promising applications of the nanostructured surface, especially in the biomedical field.

6.1.3   Summary of the anti-bacterial (AB) properties

The AB properties were investigated on the nanopillar array of the fused silica material by culturing *S. sciuri* bacteria on the surface. Statistically, the bacterial coverage rate showed no significant difference between the surfaces with or without nanopillar array. However, it was

observed under SEM that the bacteria produced nano-fibers most likely fimbriae connecting to the tips of the nanopillars, while similar cellular structures were not observed on the planar-surface sample. The cellular morphology changes verified that bacteria were able to sense and also respond to the nano-scale surface features. However, the bacterial attachment mechanism to the nanopillars requires further studies.

General methods to study the bacterial attachment were set up in this thesis. The calibration curves of the bacterial concentrations versus the growth time were measured and the bacterial culture, fixation, dehydration and drying process were validated for a clear SEM observation. The experimental workflow provided a general scheme to investigate the bacteria-surface interaction and may be easily extended to other bacterial strains and other substrates, which may shed light on the underlying mechanism of bacteria attachment and lead to an improved nanostructured surface for better AB properties in future.

6.2   Outlook

6.2.1   Nanostructures on curved surfaces

For optical applications, surfaces of the optical components are often not planar, but have a curved surface with a specifically designed radius. The experiment of nanoimprinting for a curved surface in Section 4.4.3 shows preliminary results. The process can be optimized to further improve the nanostructure profile on both inner and outer surfaces. For example, the nanoimprinting and demolding temperatures need to be fine adjusted, as the mold is much thicker than the planar mold causing longer time for the heat transfer. The centers of the top and bottom molds should be exactly aligned during the imprinting process to achieve perfect nanostructures. However, this alignment is much more difficult on curved molds compared to planar-surface molds. Therefore, a special mechanical jig should be designed to solve this problem.

6.2.2   Nanostructures for anti-reflective (AR) properties

On the inorganic substrates, there is not a high need of room to further improve the transmittance, as it is already 99.5% per interface. However, there is still plenty of room to improve the AR performance of nanostructure arrays on organic substrates. The optical model based on EMT theory indicates two possible ways to further improve the AR performance by optimizing the shape of the nanostructures. The first way is to reduce the inter-pillar spacing without changing the pillar diameter or height, thereby increasing the filling factor at the bottom layer. The second way is to optimize the shape of the nanopillars, *i.e.* by sharpening the tip of the pillars, thereby decreasing the filling factor at the top. Both ways would smooth the transition of the refractive index from air to the substrate, thus providing a better AR performance.

The nanoimprinting process developed and refined in this thesis offers a fast and large-area method that truly replicates the nanostructures. To accomplish the desired geometry discussed above, the key is to prepare the master mold with the right nanostructure geometry,

thus the fabrication procedures should be adjusted correspondingly in the following two ways. The first approach would be to decrease the spin coating speed for the micelles, while keeping the polymer chain length and concentration the same, thus a shorter inter-pillar spacing can be obtained. The second way would be to optimize the RIE process, or specifically to reduce the etching power but use more repeating etching cycles. In this way, the etching of the Au nanoparticle would be slower and it could serve as the etching mask for longer time. Therefore, the nanopillars can be accomplished with higher aspect ratio and shaper tips.

6.2.3   Nanostructures for anti-bacterial (AB) properties

It has been reported that recessed nanostructures exhibit better AB property compared to raised structures [88], thus one future work to improve the AB property of the nanopillar surface would be to use the reversed nanostructures, *i.e.* nanohole arrays. From the material aspect, it was also shown in literature that the bacterial attachment might depend on the material stiffness. Therefore, the organic substrates prepared in this thesis, *e.g.* PMMA, with nanopillars or nanoholes should be examined further. Finally, different bacterial strains behave very differently during the attachment process. For example, bacteria can be various in size and shape [218], some of them with flagella can actively propel [219] and sense the environment [220], and other bacteria may have specific molecular recognition mechanism to the surface [203]. Thus using the same workflow, but switching to other bacteria strains, such as gram-negative bacteria (*E. coli*) or other gram-positive bacteria other than *S. sciuri*, may lead to new observations of bacteria response to the nanostructured surface.

References

[1]   Feynman, R. P., 1960, "There's plenty of room at the bottom," Engineering and science, **23**, pp. 22–36.

[2]   Vukusic, P., and Sambles, J. R., 2003, "Photonic structures in biology," Nature, **424**, pp. 852–855.

[3]   Vukusic, P., Sambles, J. R., Lawrence, C. R., and Wootton, R. J., 1999, "Quantified interference and diffraction in single *Morpho* butterfly scales," Proceedings of the Royal Society B: Biological Sciences, **266**, pp. 1403–1411.

[4]   Siddique, R. H., Diewald, S., Leuthold, J., and Hölscher, H., 2013, "Theoretical and experimental analysis of the structural pattern repsonsible for the iridescence of *Morpho* butterflies," Optics Express, **21**, pp. 14351–14361.

[5]   Bernhard, C. G., 1967, "Strukturelle und funktionelle adaptation in einem visuellen system," Endeavour, **26**, pp. 79–84.

[6]   Clapham, P. B., and Hutley, M. C., 1973, "Reduction of lens reflexion by the 'moth eye' principle," Nature, **244**, pp. 281–282.

[7]   Koch, K., and Barthlott, W., 2009, "Superhydrophobic and superhydrophilic plant surfaces: an inspiration for biomimetic materials," Philosophical Transactions of the Royal Society A, **367**, pp. 1487–1509.

[8]   Koch, K., Bhushan, B., Jung, Y. C., and Barthlott, W., 2009, "Fabrication of artificial Lotus leaves and significance of hierarchical structure for superhydrophobicity and low adhesion," Soft Matter, **5**, pp. 1386–1393.

[9]   Gombert, A., Glaubitt, W., Rose, K., Dreibholz, J., Zanke, C., Bläsi, B., Heinzel, A., Horbelt, W., Sporn, D., Döll, W., Wittwer, V., and Luther, J., 1998, "Glazing with very high solar transmittance," Solar Energy, **62**, pp. 177–188.

[10]   Gombert, A., Rose, K., Heinzel, A., Horbelt, W., Zanke, C., Bläsi, B., and Wittwer, V., 1998, "Antireflective submicrometer surface-relief gratings for solar applications," Solar Energy Materials and Solar Cells, **54**, pp. 333–342.

[11]   Potyrailo, R. A., Ghiradella, H., Vertiatchikh, A., Dovidenko, K., Cournoyer, J. R., and Olson, E., 2007, "*Morpho* butterfly wing scales demonstrate highly selective vapour response," Nature Photonics, **1**, pp. 123–128.

[12]   Lin, V. S., Motesharei, K., Dancil, K. P., Sailor, M. J., and Ghadiri, M. R., 1997, "A porous silicon-based optical interferometric biosensor.," Science, **278**, pp. 840–843.

[13]   Sharp Corporation, 2012, "Sharp at CEATEC Japan 2012", http://www.sharp-world.com/corporate/news/120925.html. [Accessed: 12-Nov-2015].

[14]   Prucker, O., Schimmel, M., Tovar, G., Knoll, W., and Rühe, J., 1998, "Microstructuring of molecularly thin polymer layers by photolithography," Advanced Materials, **10**, pp. 1073–1077.

[15]   Ahn, S. J., Kaholek, M., Lee, W.-K., LaMattina, B., LaBean, T. H., and Zauscher, S., 2004, "Surface-initiated polymerization on nanopatterns fabricated by electron-beam lithography," Advanced Materials, **16**, pp. 2141–2145.

[16]   Taniguchi, J., Koga, K., Kogo, Y., and Miyamoto, I., 2006, "Rapid and three-dimensional nanoimprint template fabrication technology using focused ion beam lithography," Microelectronic Engineering, **83**, pp. 940–943.

[17]   Lan, H., and Ding, Y., 2010, "Nanoimprint Lithography," Nanoimprint Lithography, InTech, pp. 457–494.

[18]   Chou, S. Y., Krauss, P. R., and Renstrom, P. J., 1996, "25-nanometer resolution," Science, **272**, pp. 85–87.

[19]   Xia, Y., and Whitesides, G. M., 1998, "Replica molding with a polysiloxane mold provides this patterned microstructure," Angewandte Chemie International Edition, **37**, pp. 550–575.

[20]   Rosa, A. L., Yan, M., Fernandez, R., Wang, X., and Zegarra, E., 2012, "An overview of proton-fountain electric-field-assisted nanolithography (PEN) in the context of top-down and bottom-up approaches to nanotechnology," REVCIUNI, **15**, pp. 87–129.

[21]   Edler, K. J., 2004, "Soap and sand: construction tools for nanotechnology.," Philosophical Transactions of the Royal Society A, **362**, pp. 2635–2651.

[22]   Groves, T. R., Pickard, D., Rafferty, B., Crosland, N., Adam, D., and Schubert, G., 2002, "Maskless electron beam lithography: prospects, progress, and challenges," Microelectronic Engineering, **61-62**, pp. 285–293.

[23]   Tseng, A. A., and Notargiacomo, A., 2005, "Nanofabrication by scanning probe microscope lithography:

References

A review," Journal of Vacuum Science & Technology B: Microelectronics and Nanometer Structures, **23**, pp. 877–894.

[24] Parikh, D., Craver, B., Nounu, H. N., Fong, F.-O., and Wolfe, J. C., 2008, "Nanoscale pattern definition on nonplanar surfaces using ion beam proximity lithography and conformal plasma-deposited resist," Journal of Microelectromechanical Systems, **17**, pp. 735–740.

[25] Seo, J.-H., Park, J. H., Ma, Z., Choi, J., and Ju, B.-K., 2014, "Nanopatterning by laser interference lithography: applications to optical devices," Journal of nanoscience and nanotechnology, **14**, pp. 1521–1532.

[26] Hauser, H., Berger, P., Michl, B., Müller, C., Schwarzkopf, S., Hermle, M., and Bläsi, B., 2010, "Nanoimprint lithography for solar cell texturisation," Proceedings of SPIE, **7716**, pp. 77160X–1–77160X–9.

[27] Hauser, H., Michl, B., Kübler, V., Schwarzkopf, S., Müller, C., Hermle, M., and Bläsi, B., 2011, "Nanoimprint lithography for honeycomb texturing of multicrystalline silicon," Energy Procedia, **8**, pp. 648–653.

[28] de A Mello, B., da Costa, I. F., Lima, C. R. A., and Cescato, L., 1995, "Developed profile of holographically exposed photoresist gratings," Applied Optics, **34**, pp. 597–603.

[29] Favret, E. A., and Fuentes, N. O., 2009, "The moth-eye effect: from fundamentals to commercial exploitation," Functional properties of bio-inspired surfaces, World Scientific Publishing Co. Pte. Ltd., pp. 79–102.

[30] Dammel, R. R., 1993, Diazonaphtochinone-based resists, SPIE press.

[31] Yang, S.-M., Jang, S. G., Choi, D.-G., Kim, S., and Yu, H. K., 2006, "Nanomachining by colloidal lithography," Small, **2**, pp. 458–475.

[32] Li, F., Josephson, D. P., and Stein, A., 2011, "Colloidal assembly: the road from particles to colloidal molecules and crystals," Angewandte Chemie International Edition, **50**, pp. 360–388.

[33] Rahman, I. A., and Padavettan, V., 2012, "Synthesis of silica nanoparticles by sol-gel: size-dependent properties, surface modification, and applications in silica-polymer nanocomposites-a review," Journal of Nanomaterials, **2012**, pp. 1–15.

[34] Langmuir, I., and Blodgett, K. B., 1935, "Über einige neue Methoden zur Untersuchung von monomolekularen Filmen," Kolloid-Zeitschrift, **73**, pp. 257–263.

[35] Denkov, N. D., Velev, O. D., Kralchevski, P. A., Ivanov, I. B., Yoshimura, H., and Nagayama, K., 1992, "Mechanism of formation of two-dimensional crystals from latex particles on substrates," Langmuir, **8**, pp. 3183–3190.

[36] Dimitrov, A. S., and Nagayama, K., 1996, "Continuous convective assembling of fine particles into two-dimensional arrays on solid surfaces," Langmuir, **12**, pp. 1303–1311.

[37] Iovan, A., Fischer, M., Conte, Lo, R., and Korenivski, V., 2012, "Sub-10 nm colloidal lithography for circuit-integrated spin-photo-electronic devices," Beilstein Journal of Nanotechnology, **3**, pp. 884–892.

[38] Glass, R., Möller, M., and Spatz, J. P., 2003, "Block copolymer micelle nanolithography," Nanotechnology, **14**, pp. 1153–1160.

[39] Spatz, J. P., Mössmer, S., Hartmann, C., Möller, M., Herzog, T., Krieger, M., Boyen, H.-G., Ziemann, P., and Kabius, B., 2000, "Ordered deposition of inorganic clusters from micellar block copolymer films," Langmuir, **16**, pp. 407–415.

[40] Lohmüller, T., Helgert, M., Sundermann, M., Brunner, R., and Spatz, J. P., 2008, "Biomimetic interfaces for high-performance optics in the deep-UV light range," Nano Letters, **8**, pp. 1429–1433.

[41] Xia, Y., McClelland, J. J., Gupta, R., Qin, D., Zhao, X.-M., Sohn, L. L., Celotta, R. J., and Whitesides, G. M., 1997, "Replica molding using polymeric materials: a practical step toward nanomanufacturing," Advanced Materials, **9**, pp. 147–149.

[42] Kane, R. S., Takayama, S., Ostuni, E., Ingber, D. E., and Whitesides, G. M., 1999, "Patterning proteins and cells using soft lithography," Biomaterials, **20**, pp. 2363–2376.

[43] Kim, P., Kwon, K. W., Park, M. C., Lee, S. H., Kim, S. M., and Suh, K. Y., 2008, "Soft lithography for microfluidics: a review," Biochip Journal, **2**, pp. 1–11.

[44] Jin, H.-C., Abelson, J. R., Erhardt, M. K., and Nuzzo, R. G., 2004, "Soft lithographic fabrication of an image sensor array on a curved substrate," Journal of Vacuum Science & Technology B: Microelectronics and Nanometer Structures, **22**, pp. 2548–2551.

[45] Mujahid, A., Iqbal, N., and Afzal, A., 2013, "Bioimprinting strategies: from soft lithography to biomimetic sensors and beyond," Biotechnology Advances, **31**, pp. 1435–1447.

[46] Axel Buguin, Min-Hui Li, Pascal Silberzan, Benoit Ladoux, A., Patrick Keller, 2006, "Micro-actuators: when artificial muscles made of nematic liquid crystal elastomers meet soft lithography," Journal of American Chemical Society, **128**, pp. 1088–1089.

[47] Whitesides, G. M., Ostuni, E., Takayama, S., Jiang, X., and Ingber, D. E., 2001, "Soft lithography in biology and biochemistry," Annual Review of Biomedical Engineering, **3**, pp. 353–373.

[48] Guo, L. J., 2007, "Nanoimprint lithography: methods and material requirements," Advanced Materials, **19**, pp. 495–513.

[49] Chou, S. Y., Krauss, P. R., and Renstrom, P. J., 1995, "Imprint of sub- 25 nm vias and trenches in polymers," Applied Physics Letters, **67**, pp. 3114–3116.

[50] Grellmann, W., and Seidler, S., 2001, Deformation and Fracture Behaviour of Polymers, Springer-Verlag Berlin Heidelberg.

[51] Schift, H., and Kristensen, A., 2010, "Nanoimprint lithography-patterning of resist using molding," Handbook of nanotechnology, Springer-Verlag Berlin Heidelberg.

[52] Gates, B. D., Xu, Q., Stewart, M., Ryan, D., Willson, C. G., and Whitesides, G. M., 2005, "New approaches to nanofabrication: molding, printing, and other techniques," Chemical Reviews, **105**, pp. 1171–1196.

[53] Xie, G., Zhang, G., Lin, F., Zhang, J., Liu, Z., and Mu, S., 2008, "The fabrication of subwavelength anti-reflective nanostructures using a bio-template," Nanotechnology, **19**, pp. 095605–095609.

[54] Ting, C.-J., Chang, F.-Y., Chen, C.-F., and Chou, C. P., 2008, "Fabrication of an antireflective polymer optical film with subwavelength structures using a roll-to-roll micro-replication process," Journal of Micromechanics and Microengineering, **18**, pp. 075001–075009.

[55] Choi, K., Park, S. H., Song, Y. M., Lee, Y. T., Hwangbo, C. K., Yang, H., and Lee, H. S., 2010, "Nano-tailoring the surface structure for the monolithic high- performance antireflection polymer film," Advanced Materials, **22**, pp. 3713–3718.

[56] Kang, Y. H., Oh, S. S., Kim, Y.-S., and Choi, C.-G., 2010, "Fabrication of antireflection nanostructures by hybrid nano-patterning lithography," Microelectronic Engineering, **87**, pp. 125–128.

[57] Chen, J. Y., Chang, W. L., Huang, C. K., and Sun, K. W., 2011, "Biomimetic nanostructured antireflection coating and its application on crystalline silicon solar cells," Optics Express, **19**, pp. 14411–14419.

[58] Obducat AB, "SINDRE®-Nano imprint lithography system for production", http://www.obducat.com/SINDRE®-489.aspx. [Accessed: Dec-2015].

[59] SUSS MicroTec AG, "A new method for large area nanoimprint lithography", http://www.suss.com/en/products-solutions/technologies/imprint-lithography/scil/. [Accessed: Dec-2015].

[60] Lan, H., and Ding, Y., 2010, "Nanoimprint Lithography," Lithography, InTech, pp. 457–494.

[61] Steck, D. A., 2015, "Thin films," Thin Films, pp. 171–198.

[62] Lee, S. E., Choi, S. W., and Yi, J., 2000, "Double-layer anti-reflection coating using MgF_2 and CeO_2 films on a crystalline silicon substrate," Thin Solid Films, **376**, pp. 208–213.

[63] Raut, H. K., Ganesh, V. A., Nair, A. S., and Ramakrishna, S., 2011, "Anti-reflective coatings: a critical, in-depth review," Energy & Environmental Science, **4**, pp. 3779–3804.

[64] Liddell, H. P. H., Mehrotra, K., Lambropoulos, J. C., and Jacobs, S. D., 2013, "Fracture mechanics of delamination defects in multilayer dielectric coatings," Applied Optics, **52**, pp. 7689–7698.

[65] Lohmüller, T., Brunner, R., and Spatz, J. P., 2010, "Improved properties of optical surfaces by following the example of the 'moth eye'," Biomimetics learning from nature, InTech, pp. 451-466.

[66] Brunner, R., Sandfuchs, O., Pacholski, C., Morhard, C., and Spatz, J., 2011, "Lessons from nature: biomimetic subwavelength structures for high-performance optics," Laser & Photon Rev, **6**, pp. 641–659.

[67] Wilson, S. J., and Hutley, M. C., 2010, "The optical properties of 'moth eye' antireflection surfaces," Optica Acta: International Journal of Optics, **29**, pp. 993–1009.

[68] Southwell, W. H., 1991, "Pyramid-array surface-relief structures producing antireflection index matching on optical surfaces," Journal of the Optical Society of America A, **8**, pp. 549–553.

[69] Ko, D.-H., Tumbleston, J. R., Henderson, K. J., Euliss, L. E., DeSimone, J. M., Lopez, R., and Samulski, E. T., 2011, "Biomimetic microlens array with antireflective 'moth-eye' surface," Soft Matter, **7**, pp. 6404–6407.

[70] Auzelyte, V., Flauraud, V., Cadarso, V. J., Kiefer, T., and Brugger, J., 2012, "Biomimetic soft lithography on curved nanostructured surfaces," Microelectronic Engineering, **97**, pp. 269–271.

[71] Rao, J., Winfield, R., and Keeney, L., 2010, "Moth-eye-structured light-emitting diodes," Optics Communications, **283**, pp. 2446–2450.

[72] Lohmüller, T., 2008, "Nanostructured functional materials," PhD thesis, Universität Heidelberg.

[73] Lohmüller, T., Aydin, D., Schwieder, M., Morhard, C., Louban, I., Pacholski, C., and Spatz, J. P., 2011, "Nanopatterning by block copolymer micelle nanolithography and bioinspired applications," Biointerphases, **6**, pp. MR1–MR12.

[74] Morhard, C., 2010, "Herstellung effektiver Medien mittels mizellarer Blockcopolymer Nanolithogra-

phie," PhD thesis, Universität Heidelberg.

[75] Morhard, C., Pacholski, C., Lehr, D., Brunner, R., Helgert, M., Sundermann, M., and Spatz, J. P., 2010, "Tailored antireflective biomimetic nanostructures for UV applications," Nanotechnology, **21**, pp. 425301–425306.

[76] Tilley, R. J. D., 2011, Colour and the Optical Properties of Materials, Wiley & Sons, Ltd.

[77] Rayleigh, L., 1879, "On reflection of vibrations at the confines of two media between which the transition is gradual," Proceedings of the London Mathematical Society, **s1-11**, pp. 51–56.

[78] Kohnen, W., 2003, "Development of a long-lasting ventricular catheter impregnated with a combination of antibiotics," Biomaterials, **24**, pp. 4865–4869.

[79] Donlan, R. M., 2001, "Biofilms and device-associated infections.," Emerging Infectious Diseases, **7**, pp. 277–281.

[80] B. Braun Melsungen AG, "Microbiological contamination," http://www.safeinfusiontherapy.com/documents/french/ac_microbiologicalcontamination.pdf. [Accessed: Dec-2015].

[81] Dayyoub, E., Belz, E., Dassinger, N., Keusgen, M., and Bakowsky, U., 2011, "A novel method for designing nanostructured polymer surfaces for reduced bacteria adhesion," Physica Status Solidi (A), **208**, pp. 1279–1283.

[82] Timofeeva, L., and Kleshcheva, N., 2011, "Antimicrobial polymers: mechanism of action, factors of activity, and applications," Applied Microbiology and Biotechnology, **89**, pp. 475–492.

[83] McBain, A. J., Ledder, R. G., Moore, L. E., Catrenich, C. E., and Gilbert, P., 2004, "Effects of Quaternary-Ammonium-Based Formulations on Bacterial Community Dynamics and Antimicrobial Susceptibility," Applied and Environmental Microbiology, **70**, pp. 3449–3456.

[84] Jung, W. K., Koo, H. C., Kim, K. W., Shin, S., Kim, S. H., and Park, Y. H., 2008, "Antibacterial activity and mechanism of action of the silver ion in *Staphylococcus aureus* and *Escherichia coli*," Applied and Environmental Microbiology, **74**, pp. 2171–2178.

[85] Hu, C. M., 2013, Touch screen with bacteria inhibition layer and manufacturing method thereof, Patent US 8524314 B2.

[86] Glinel, K., Thebault, P., Humblot, V., Pradier, C. M., and Jouenne, T., 2012, "Antibacterial surfaces developed from bio-inspired approaches," Acta Biomaterialia, **8**, pp. 1670–1684.

[87] Anselme, K., Davidson, P., Popa, A. M., Giazzon, M., Liley, M., and Ploux, L., 2010, "The interaction of cells and bacteria with surfaces structured at the nanometre scale," Acta Biomaterialia, **6**, pp. 3824–3846.

[88] Graham, M. V., and Cady, N. C., 2014, "Nano and microscale topographies for the prevention of bacterial surface fouling," Coatings, **4**, pp. 37–59.

[89] Chiappetta, D. A., Degrossi, J., Teves, S., D'Aquino, M., Bregni, C., and Sosnik, A., 2008, "Triclosan-loaded poloxamine micelles for enhanced topical antibacterial activity against biofilm," European Journal of Pharmaceutics and Biopharmaceutics, **69**, pp. 535–545.

[90] Epstein, A. K., Hochbaum, A. I., Kim, P., and Aizenberg, J., 2011, "Control of bacterial biofilm growth on surfaces by nanostructural mechanics and geometry," Nanotechnology, **22**, pp. 494007–494014.

[91] Liu, Y., and Zhao, Q., 2005, "Influence of surface energy of modified surfaces on bacterial adhesion," Biophysical Chemistry, **117**, pp. 39–45.

[92] Quirynen, M., Marechal, M., Busscher, H. J., Weerkamp, A. H., Arends, J., Darius, P. L., and van Steenberghe, D., 1989, "The influence of surface free-energy on planimetric plaque growth in man," Journal of Dental Research, **68**, pp. 796–799.

[93] Tegoulia, V. A., and Cooper, S. L., 2002, "*Staphylococcus aureus* adhesion to self-assembled monolayers: effect of surface chemistry and fibrinogen presence," Colloids and Surfaces B: Biointerfaces, **24**, pp. 217–228.

[94] Vacheethasanee, K., and Marchant, R. E., 2000, "Nonspecific *Staphylococcus epidermidis* adhesion," Handbook of Bacterial Adhesion, Springer Science+Business Media, LLC, pp. 73–90.

[95] Hasan, J., Crawford, R. J., and Ivanova, E. P., 2013, "Antibacterial surfaces: the quest for a new generation of biomaterials," Trends in Biotechnology, **31**, pp. 295–304.

[96] Campoccia, D., Montanaro, L., and Arciola, C. R., 2013, "A review of the biomaterials technologies for infection-resistant surfaces," Biomaterials, **34**, pp. 8533–8554.

[97] Isquith, A. J., Abbott, E. A., and Walters, P. A., 1972, "Surface-Bonded Antimicrobial Activity of an Organosilicon Quaternary Ammonium Chloride," Applied and Environmental Microbiology, **24**, pp. 859–863.

[98] Chernousova, S., and Epple, M., 2013, "Silver as antibacterial agent: ion, nanoparticle, and metal," Angewandte Chemie International Edition, **52**, pp. 1636–1653.

[99]   Daeyeon Lee, Robert E Cohen, A., Michael F Rubner, 2005, "Antibacterial Properties of Ag Nanoparticle Loaded Multilayers and Formation of Magnetically Directed Antibacterial Microparticles," Langmuir, **21**, pp. 9651–9659.

[100] Bazaka, K., Jacob, M. V., Chrzanowski, W., and Ostrikov, K., 2015, "Anti-bacterial surfaces: natural agents, mechanisms of action, and plasma surface modification," Royal Society of Chemistry Advances, **5**, pp. 48739–48759.

[101] Katsikogianni, M., and Missirlis, Y. F., 2004, "Concise review of mechanisms of bacterial adhesion to biomaterials and of techniques used in estimating bacteria-material interactions," European Cells and Materials, **8**, pp. 37–57.

[102] Kiremitçi-Gümü, M., 1996, "Microbial adhesion to ionogenic PHEMA, PU and PP implants," Biomaterials, **17**, pp. 443–449.

[103] Park, K. D., Kim, Y. S., Han, D. K., Kim, Y. H., Lee, E. H. B., Suh, H., and Choi, K. S., 1998, "Bacterial adhesion on PEG modified polyurethane surfaces," Biomaterials, **19**, pp. 851–859.

[104] Shi, L., Ardehali, R., Caldwell, K. D., and Valint, P., 2000, "Mucin coating on polymeric material surfaces to suppress bacterial adhesion," Colloids and Surfaces B: Biointerfaces, **17**, pp. 229–239.

[105] Balazs, D. J., Triandafillu, K., Chevolot, Y., Aronsson, B. O., Harms, H., Descouts, P., and Mathieu, H. J., 2003, "Surface modification of PVC endotracheal tubes by oxygen glow discharge to reduce bacterial adhesion," Surface and Interface Analysis, **35**, pp. 301–309.

[106] Song, F., Koo, H., and Ren, D., 2015, "Effects of material properties on bacterial adhesion and biofilm formation," Journal of Dental Research, **94**, pp. 1027–1034.

[107] Whitehead, K. A., and Verran, J., 2006, "The effect of surface topography on the retention of microorganisms," Food and Bioproducts Processing, **84**, pp. 253–259.

[108] Characklis, W. G., 2009, "Bioengineering report: fouling biofilm development: a process analysis," Biotechnology and Bioengineering, **102**, pp. 309–347.

[109] Ionescu, A., Wutscher, E., Brambilla, E., Schneider Feyrer, S., Giessibl, F. J., and Hahnel, S., 2012, "Influence of surface properties of resin- based composites on in vitro *Streptococcus mutans* biofilm development," European Journal of Oral Sciences, **120**, pp. 458–465.

[110] Boyd, R. D., Verran, J., Jones, M. V., and Bhakoo, M., 2002, "Use of the atomic force microscope to determine the effect of substratum surface topography on bacterial adhesion," Langmuir, **18**, pp. 2343–2346.

[111] Oh, J. K., Lu, X., Min, Y., Cisneros-Zevallos, L., and Akbulut, M., 2015, "Bacterially antiadhesive, optically transparent surfaces inspired from rice leaves," ACS Applied Materials & Interfaces, **7**, pp. 19274–19281.

[112] Pogodin, S., Hasan, J., Baulin, V. A., Webb, H. K., Truong, V. K., Nguyen, T. H. P., Boshkovikj, V., Fluke, C. J., Watson, G. S., Watson, J. A., Crawford, R. J., and Ivanova, E. P., 2013, "Biophysical model of bacterial cell interactions with nanopatterned cicada wing surfaces," Biophysical Journal, **104**(4), pp. 835–840.

[113] Scardino, A. J., and de Nys, R., 2011, "Mini review: biomimetic models and bioinspired surfaces for fouling control," Biofouling, **27**, pp. 73–86.

[114] Perni, S., and Prokopovich, P., 2013, "Micropatterning with conical features can control bacterial adhesion on silicone," Soft Matter, **9**, pp. 1844–1851.

[115] Jansson, T., Clare-Salzler, Z. J., Zaveri, T. D., Mehta, S., Dolgova, N. V., Chu, B.-H., Ren, F., and Keselowsky, B. G., 2012, "Antibacterial effects of zinc oxide nanorod surfaces," Journal of Nanoscience and Nanotechnology, **12**, pp. 7132–7138.

[116] Ivanova, E. P., Hasan, J., Webb, H. K., Gervinskas, G., Juodkazis, S., Truong, V. K., Wu, A. H. F., Lamb, R. N., Baulin, V. A., Watson, G. S., Watson, J. A., Mainwaring, D. E., and Crawford, R. J., 2013, "Bactericidal activity of black silicon," Nature Communications, **4**, pp. 2838–2844.

[117] Díaz, C., Schilardi, P. L., Salvarezza, R. C., Fernández Lorenzo de Mele, M., 2007, "Nano/Microscale order affects the early stages of biofilm formation on metal surfaces," Langmuir, **23**, pp. 11206–11210.

[118] Ling, J. F., III, Graham, M. V., and Cady, N. C., 2012, "Effect of topographically patterned poly(dimethylsiloxane) surfaces on *Pseudomonas aeruginosa* adhesion and biofilm formation," Nano LIFE, **4**, pp. 1242004–1242015.

[119] Jeong, H. E., Kim, I., Karam, P., Choi, H.-J., and Yang, P., 2013, "Bacterial recognition of silicon nanowire arrays," Nano Letters, **13**, pp. 2864–2869.

[120] Sakamoto, A., Terui, Y., Horie, C., Fukui, T., Masuzawa, T., Sugawara, S., Shigeta, K., Shigeta, T., Igarashi, K., and Kashiwagi, K., 2014, "Antibacterial effects of protruding and recessed shark skin micropatterned surfaces of polyacrylate plate with a shallow groove," FEMS Microbiology Letters, **361**, pp. 10–16.

References

[121] Proft, T., and Baker, E. N., 2009, "Pili in gram-negative and gram-positive bacteria - structure, assembly and their role in disease," Cellular and Molecular Life Sciences, **66**, pp. 613–635.

[122] Schmidt, H., Naumann, G., and Putzke, H.-P., 1988, "Detection of different fimbriae-like structures on the surface of Staphylococcus saprophyticus," Zentralblatt für Bakteriologie, Mikrobiologie und Hygiene. Series A, **268**, pp. 228–237.

[123] Hall-Stoodley, L., Costerton, J. W., and Stoodley, P., 2004, "Bacterial biofilms: from the natural environment to infectious diseases," Nature Reviews Microbiology, **2**, pp. 95–108.

[124] Kim, S., Jung, U. T., Kim, S.-K., Lee, J.-H., Choi, H. S., Kim, C.-S., and Jeong, M. Y., 2015, "Nanostructured multifunctional surface with antireflective and antimicrobial characteristics," ACS Applied Materials & Interfaces, **7**, pp. 326–331.

[125] Flemming, H.-C., and Wingender, J., 2010, "The biofilm matrix," Nature Reviews Microbiology, **8**, pp. 623–633.

[126] Ploux, L., Ponche, A., and Anselme, K., 2010, "Bacteria/material interfaces: role of the material and cell wall properties," Journal of Adhesion Science and Technology, **24**, pp. 2165–2201.

[127] Kästle, G., Boyen, H. G., Weigl, F., Lengl, G., Herzog, T., Ziemann, P., Riethmüller, S., Mayer, O., Hartmann, C., Spatz, J. P., Möller, M., Ozawa, M., Banhart, F., Garnier, M. G., and Oelhafen, P., 2003, "Micellar nanoreactors - preparation and characterization of hexagonally ordered arrays of metallic nanodots," Advanced Functional Materials, **13**, pp. 853–861.

[128] Bansmann, J., Kielbassa, S., Hoster, H., Weigl, F., Boyen, H. G., Wiedwald, U., Ziemann, P., Behm, R. J., 2007, "Controlling the interparticle spacing of Au−salt loaded micelles and Au nanoparticles on flat surfaces," Langmuir, **23**, pp. 10150–10155.

[129] Wiedwald, U., Han, L., Biskupek, J., Kaiser, U., and Ziemann, P., 2010, "Preparation and characterization of supported magnetic nanoparticles prepared by reverse micelles," Beilstein Journal of Nanotechnology, **1**, pp. 24–47.

[130] Lawrence, C. J., 1988, "The mechanics of spin coating of polymer films," Physics of Fluids (1958-1988), **31**, pp. 2786–2795.

[131] Segalman, R. A., 2005, "Patterning with block copolymer thin films," Materials Science and Engineering: R: Reports, **48**, pp. 191–226.

[132] Gennes, P.-G. de, Brochard-Wyart, F., and Quéré, D., 2004, Capillarity and Wetting Phenomena, Springer-Verlag New York.

[133] Jansen, H., Gardeniers, H., de Boer, M., Elwenspoek, M., and Fluitman, J., 1996, "A survey on the reactive ion etching of silicon in microtechnology," Journal of Micromechanics and Microengineering, **6**, pp. 14–28.

[134] Leech, P. W., 1999, "Reactive ion etching of quartz and silica-based glasses in CF_4/CHF_3 plasmas," Vacuum, **55**, pp. 191–196.

[135] Sharpe, R. B. A., Burdinski, D., Huskens, J., Zandvliet, H. J. W., Reinhoudt, D. N., and Poelsema, B., 2005, "Chemically patterned flat stamps for microcontact printing," Journal of the American Chemical Society, **127**, pp. 10344–10349.

[136] Srinivasan, U., Houston, M. R., Howe, R. T., and Maboudian, R., 1998, "Alkyltrichlorosilane-based self-assembled monolayer films for stiction reduction in silicon micromachines," Journal of Microelectromechanical Systems, **7**, pp. 252–260.

[137] "Surface tension values of some common test liquids for surface energy analysis", http://www.surface-tension.de. [Accessed: 15-Nov-2015].

[138] Lee, D., Mekaru, H., Hiroshima, H., Matsumoto, S., Itoh, T., Takahashi, M., and Maeda, R., 2009, "3D replication using PDMS mold for microcoil," Microelectronic Engineering, **86**, pp. 920–924.

[139] González-Cavada, J., Corral, O., Niño, A., Estrella, M. A., Fuentes, J. A., and Madrid-Costa, D., 2009, "Base curve influence on the fitting and comfort of the senofilcon a contact lens," Journal of Optometry, **2**, pp. 90–93.

[140] Goodhew, P. J., Humphreys, J., and Beanland, R., 2001, Electron microscopy and analysis, Taylor & Fancis.

[141] Wang, S. H., Hsiao, Y. J., Hua Fang, Te, Ji, L. W., Lin, M. H., Kang, S. H., and Lee, Y. C., 2014, "A textured SiO_2 antireflection layer for efficient organic solar cells," Surface Topography: Metrology and Properties, **2**, pp. 035005–035009.

[142] Nelson, D. R., and Halperin, B. I., 1979, "Dislocation-mediated melting in two dimensions," Physical Review B, **19**, pp. 2457–2484.

[143] Williges, C., Chen, W., Morhard, C., Spatz, J. P., and Brunner, R., 2013, "Increasing the order parameter of quasi-hexagonal micellar nanostructures by ultrasound annealing," Langmuir, **29**, pp. 989–993.

[144] Hawkes, P. W., and Spence, 2007, Science of Microscopy, Springer-Verlag New York.

[145] Budisa, N., and Schulze-Makuch, D., 2014, "Supercritical carbon dioxide and its potential as a life-sustaining solvent in a planetary environment," Life, **4**, pp. 331–340.

[146] Förster, S., Zisenis, M., Wenz, E., and Antonietti, M., 1996, "Micellization of strongly segregated block copolymers," The Journal of Chemical Physics, **104**, pp. 9956–9970.

[147] Yoo, S., Sohn, B. H., Zin, W. C., Jung, J. C., and Park, C., 2007, "Mixtures of diblock copolymer micelles by different mixing protocols," Macromolecules, **40**, pp. 8323–8328.

[148] Voulgaris, D., Tsitsilianis, C., Grayer, V., Esselink, F. J., and Hadziioannou, G., 1999, "Amphiphile micelles formed by polystyrene/poly(2-vinyl pyridine) heteroarm star copolymers in toluene," Polymer, **40**, pp. 5879–5889.

[149] Davey, W. P., 1925, "Precision measurements of the lattice constants of twelve common metals," Physical Review, **25**, pp. 753–761.

[150] Combs, C. A., 2010, Fluorescence Microscopy: A Concise Guide to Current Imaging Methods, Current Protocols in Neuroscience, Hoboken, NJ, USA.

[151] Kim, B.-J., Mastro, M. A., Jung, H., Kim, H.-Y., Kim, S. H., Holm, R. T., Hite, J., Eddy, C. R., Jr., Bang, J., and Kim, J., 2008, "Inductively coupled plasma etching of nano-patterned sapphire for flip-chip GaN light emitting diode applications," Thin Solid Films, **516**, pp. 7744–7747.

[152] Dobrovinskaya, E. R., Lytvynov, L. A., and Pishchik, V., 2009, Sapphire, Springer Science & Business Media.

[153] Hsu, Y. P., Chang, S. J., Su, Y. K., Sheu, J. K., Kuo, C. H., Chang, C. S., and Shei, S. C., 2005, "ICP etching of sapphire substrates," Optical Materials, **27**, pp. 1171–1174.

[154] Mugele, F., and Baret, J.-C., 2005, "Electrowetting: from basics to applications," Journal of Physics: Condensed Matter, **17**, pp. R705–R774.

[155] Träger, F., 2007, Springer Handbook of Lasers and Optics, Springer-Verlag New York.

[156] Melles Griot, "Optical components: finding your way through the maze", http://www.photonics.com/EDU/Handbook.aspx?AID=25455. [Accessed: 15-Nov-2015].

[157] Kim, J. K., Cho, H. S., Jung, H.-S., Lim, K., Kim, K.-B., Choi, D.-G., Jeong, J.-H., and Suh, K. Y., 2012, "Effect of surface tension and coefficient of thermal expansion in 30 nm scale nanoimprinting with two flexible polymer molds," Nanotechnology, **23**, pp. 235303–235311.

[158] Cattoni, A., Anne-Marie, H., Decanini, D., Shi, J., and Chen, J., 2011, "Soft UV nanoimprint lithography: a versatile tool for nanostructuration at the 20 nm scale," Recent Advances in Nanofabrication Techniques and Applications, InTech.

[159] Hsiao, R., and Carr, J., 1998, "Si/SiO$_2$ etching in high density SF$_6$/CHF$_3$/O$_2$ plasma," Materials Science & Engineering B, **52**, pp. 63–77.

[160] Pereira, J., Pichon, L. E., Dussart, R., Cardinaud, C., Duluard, C. Y., Oubensaid, E. H., Lefaucheux, P., Boufnichel, M., and Ranson, P., 2009, "In situ x-ray photoelectron spectroscopy analysis of SiO$_x$F$_y$ passivation layer obtained in a SF$_6$/ O$_2$ cryoetching process," Applied Physics Letters, **94**, pp. 071501–1–071501–3.

[161] del Campo, A., and Arzt, E., 2008, "Fabrication approaches for generating complex micro- and nanopatterns on polymeric surfaces," Chemical Reviews, **108**, pp. 911–945.

[162] Xia, Y., and Whitesides, G. M., 1998, "Soft lithography," Annual Review of Materials Science, **28**, pp. 153–184.

[163] Lane, S. S., Morris, M., Nordan, L., Packer, M., Tarantino, N., and Wallace, R. B., III, 2006, "Multifocal intraocular lenses," Ophthalmology Clinics of North America, **19**, pp. 89–105.

[164] Zidan, H. M., and Abu-Elnader, M., 2005, "Structural and optical properties of pure PMMA and metal chloride-doped PMMA films," Physica B: Condensed Matter, **355**, pp. 308–317.

[165] Auzelyte, V., Flauraud, V., Cadarso, V. J., Kiefer, T., and Brugger, J., 2012, "Biomimetic soft lithography on curved nanostructured surfaces," Microelectronic Engineering, **97**, pp. 269–271.

[166] Zhang, G., Zhang, J., Xie, G., Liu, Z., and Shao, H., 2006, "Cicada wings: a stamp from nature for nanoimprint lithography," Small, **2**, pp. 1440–1443.

[167] Kanamori, Y., Sasaki, M., and Hane, K., 1999, "Broadband antireflection gratings fabricated upon silicon substrates," Optics Letters, **24**, pp. 1422–1424.

[168] DeRosa, R. L., Schader, P. A., and Shelby, J. E., 2003, "Hydrophilic nature of silicate glass surfaces as a function of exposure condition," Journal of Non-Crystalline Solids, **331**, pp. 32–40.

[169] Yoshimaru, M., Koizumi, S., and Shimokawa, K., 1997, "Interaction between water and fluorine-doped silicon oxide films deposited by plasma-enhanced chemical vapor deposition," Journal of Vacuum Science & Technology A, **15**, pp. 2915–2922.

[170] Yokomachi, Y., Tohmon, R., Nagasawa, K., and Ohki, Y., 1987, "Hydrogen bond of OH-groups in silica glass and its relation to the 1.39 μm absorption," Journal of Non-Crystalline Solids, **95-96**, pp. 663–670.

References

[171] Heraeus, "Standard optics information",
http://www.sydor.com/wp-content/uploads/Heraeus-SUPRASIL-1-2-Grade-A-B-Fused-Silica.pdf. [Accessd: Dec-2015]

[172] Melles Griot, "Material properties overview",
http://ltlw3.iams.sinica.edu.tw/support/OpticsGuide/chap04_Material_Properties.pdf. [Accessed: Dec-2015].

[173] Mark, A. G., Gibbs, J. G., Lee, T. C., and Fischer, P., 2013, "Hybrid nanocolloids with programmed three-dimensional shape and material composition," Nature Materials, **12**, pp. 802–807.

[174] Jeong, H. H., Mark, A. G., Lee, T. C., Son, K., Chen, W., Alarcón Correa, M., Kim, I., Schütz, G., and Fischer, P., 2015, "Selectable Nanopattern Arrays for Nanolithographic Imprint and Etch- Mask Applications," Advanced Science, **2**, pp. 1500016–1500022.

[175] Siddique, R. H., Gomard, G., and Hölscher, H., 2015, "The role of random nanostructures for the omnidirectional anti-reflection properties of the glasswing butterfly," Nature Communications, **6**, pp. 6909–6916.

[176] Kim, D.-S., Kim, D.-H., and Jang, J.-H., 2013, "A nanoscale conical polymethyl methacrylate (PMMA) sub-wavelength structure with a high aspect ratio realized by a stamping method.," Optics Express, **21**, pp. 8450–8459.

[177] Li, X., Yu, X., and Han, Y., 2013, "Polymer thin films for antireflection coatings," Journal of Materials Chemistry C, **1**, pp. 2266–2285.

[178] Han, K., and Chang, C.-H., 2014, "Numerical modeling of sub-wavelength anti-reflective structures for solar module applications," Nanomaterials, **4**, pp. 87–128.

[179] Griesmann, U., "Thin film tool box-Ulf's Cyber Attic",
https://sites.google.com/site/ulfgri/numerical/thin-films. [Accessed: Nov-2015].

[180] Chigrin, D. N., and Torres, C. M. S., 2001, "Periodic thin-film interference filters as one-dimensional photonic crystals," Optics and Spectroscopy, **91**, pp. 484–489.

[181] Hecht, E., 2002, Optics, Pearson Education, Inc.

[182] Ivanova, E. P., Hasan, J., Webb, H. K., Truong, V. K., Watson, G. S., Watson, J. A., Baulin, V. A., Pogodin, S., Wang, J. Y., Tobin, M. J., Löbbe, C., and Crawford, R. J., 2012, "Natural bactericidal surfaces: mechanical rupture of *Pseudomonas aeruginosa* cells by cicada wings," Small, **8**, pp. 2489–2494.

[183] Krishnan, S., 2015, "Biofilm Formation on Medical Devices and Infection: Preventive Approaches," Biofilm and Materials Science, Springer International Publishing, pp. 93–108.

[184] FDA, 2015, "Foodborne illness-causing organisms in the U.S.",
http://www.fda.gov/downloads/Food/FoodborneIllnessContaminants/UCM187482.pdf. [Accessed: Nov-2015].

[185] Shaw, C., Stitt, J. M., and Cowan, S. T., 1951, "Staphylococci and their classification," Microbiology, **5**, pp. 1010–1023.

[186] Cowan, S. T., Shaw, C., and Williams, R. E. O., 1954, "Type Strain for *Staphylococcus aureus* Rosenbach," Microbiology, **10**, pp. 174–176.

[187] Kloos, W. E., Tornabene, T. G., and Schleifer, K. H., 1974, "Isolation and characterization of micrococci from human skin, including two new species: *Micrococcus lylae* and *Micrococcus kristinae*," International Journal of Systematic Bacteriology, **24**, pp. 79–101.

[188] Kloos, W. E., Schleifer, K. H., and Smith, R. F., 1976, "Characterization of *Staphylococcus sciuri* sp.nov. and its Subspecies," International Journal of Systematic Bacteriology, **26**, pp. 22–37.

[189] Baddiley, J., Buchanan, J. G., Rajbhandary, U. L., and Sanderson, A. R., 1962, "Teichoic acid from the walls of *Staphylococcus aureus* H," Biochemical Journal, **82**, pp. 439–448.

[190] Einstein, A., 1905, "Über die von der molekularkinetischen Theorie der Wärme geforderte Bewegung von in ruhenden Flüssigkeiten suspendierten Teilchen," Annalen der Physik, **322**, pp. 549–560.

[191] Bosman, H. J. M., Pijpers, A. P., and Jaspers, A. W. M. A., 1996, "An x-ray photoelectron spectroscopy study of the acidity of SIO_2–ZrO_2 mixed oxides," Journal of Catalysis, **161**, pp. 551–559.

[192] Beamson, G., and Briggs, D., 1992, High resolution XPS of organic polymers: the scienta ESCA300 database, John Wiley & Sons Ltd.

[193] Balkenende, A. R., van de Boogaard, H. J. A. P., Scholten, M., and Willard, N. P., 1998, "Evaluation of different approaches to assess the surface tension of low-energy solids by means of contact angle measurements," Langmuir, **14**, pp. 5907–5912.

[194] Bartle, K. D., Wright, B. W., and Lee, M. L., 1981, "Characterization of glass, quartz, and fused silica capillary column surfaces from contact-angle measurements," Chromatographia, **14**, pp. 387–397.

[195] Madigan, M. T., Martinko, J. M., Stahl, D., and Clark, D. P., 2005, Brock biology of mcroorganisms, Pearson Prentice Hall.

[196] Wu, P., and Grainger, D. W., 2006, "Drug/device combinations for local drug therapies and infection prophylaxis," Biomaterials, **27**, pp. 2450–2467.

[197] Smith, A. W., 2005, "Biofilms and antibiotic therapy: Is there a role for combating bacterial resistance by the use of novel drug delivery systems?," Advanced Drug Delivery Reviews, **57**, pp. 1539–1550.

[198] Cai, W., Wu, J., Xi, C., and Meyerhoff, M. E., 2012, "Diazeniumdiolate-doped poly(lactic-co-glycolic acid)-based nitric oxide releasing films as antibiofilm coatings," Biomaterials, **33**, pp. 7933–7944.

[199] Rai, M., Yadav, A., and Gade, A., 2009, "Silver nanoparticles as a new generation of antimicrobials," Biotechnology Advances, **27**, pp. 76–83.

[200] Fleming, S. A., "Nobel Lecture: Penicillin", http://www.nobelprize.org/nobel_prizes/medicine/laureates/1945/fleming-lecture.pdf. [Accessed: Nov-2015].

[201] Jeon, H.-J., Yi, S.-C., and Oh, S.-G., 2003, "Preparation and antibacterial effects of Ag–SiO$_2$ thin films by sol-gel method," Biomaterials, **24**, pp. 4921–4928.

[202] Hussain, S. M., Hess, K. L., Gearhart, J. M., Geiss, K. T., and Schlager, J. J., 2005, "In vitro toxicity of nanoparticles in BRL 3A rat liver cells," Toxicology in Vitro, **19**, pp. 975–983.

[203] Hori, K., and Matsumoto, S., 2010, "Bacterial adhesion: from mechanism to control," Biochemical Engineering Journal, **48**, pp. 424–434.

[204] Schumacher, J. F., Carman, M. L., Estes, T. G., Feinberg, A. W., Wilson, L. H., Callow, M. E., Callow, J. A., Finlay, J. A., and Brennan, A. B., 2007, "Engineered antifouling microtopographies – effect of feature size, geometry, and roughness on settlement of zoospores of the green alga Ulva," Biofouling, **23**, pp. 55–62.

[205] Schumacher, J. F., Aldred, N., Callow, M. E., Finlay, J. A., Callow, J. A., Clare, A. S., and Brennan, A. B., 2007, "Species-specific engineered antifouling topographies: correlations between the settlement of algal zoospores and barnacle cyprids," Biofouling, **23**, pp. 307–317.

[206] Xu, L.-C., and Siedlecki, C. A., 2012, "Submicron-textured biomaterial surface reduces staphylococcal bacterial adhesion and biofilm formation," Acta Biomaterialia, **8**, pp. 72–81.

[207] Park, M. R., Banks, M. K., Applegate, B., and Webster, T. J., 2008, "Influence of nanophase titania topography on bacterial attachment and metabolism," International Journal of Nanomedicine, **3**, pp. 497–504.

[208] Yu, E., Kim, S.-C., Lee, H. J., Oh, K. H., and Moon, M.-W., 2015, "Extreme wettability of nanostructured glass fabricated by non-lithographic, anisotropic etching," Scientific Reports, **5**, pp. 9362–9367.

[209] Sakikawa, N., Shishida, Y., Miyazaki, S., and Hirose, M., 1998, " In situ monitoring of silicon surfaces during reactive ion etching," Japanese Journal of Applied Physics, **37**, pp. L409–L412.

[210] Li, X., Hua, X., Ling, L., Oehrlein, G. S., and Barela, M., 2002, "Fluorocarbon-based plasma etching of SiO$_2$: Comparison of C$_4$F$_6$/Ar and C$_4$F$_8$/Ar discharges," Journal of Vacuum Science & Technology A, **20**, pp. 2052–2061.

[211] Jaszewski, R. W., Schift, H., Schnyder, B., Schneuwly, A., and Gröning, P., 1999, "The deposition of anti-adhesive ultra-thin teflon-like films and their interaction with polymers during hot embossing," Applied Surface Science, **143**, pp. 301–308.

[212] Hsu, L. C., Fang, J., Borca-Tasciuc, D. A., Worobo, R. W., and Moraru, C. I., 2013, "Effect of micro- and nanoscale topography on the adhesion of bacterial cells to solid surfaces," Applied and Environmental Microbiology, **79**, pp. 2703–2712.

[213] Mitik Dineva, N., Wang, J., Mocanasu, R. C., Stoddart, P. R., Crawford, R. J., and Ivanova, E. P., 2008, "Impact of nano- topography on bacterial attachment," Biotechnology Journal, **3**, pp. 536–544.

[214] Rizzello, L., Sorce, B., Sabella, S., Vecchio, G., Galeone, A., Brunetti, V., Cingolani, R., and Pompa, P. P., 2011, "Impact of nanoscale topography on genomics and proteomics of adherent bacteria," ASC Nano, **5**, pp. 1865–1876.

[215] Rizzello, L., Galeone, A., Vecchio, G., Brunetti, V., Sabella, S., and Pompa, P. P., 2012, "Molecular response of *Escherichia coli* adhering onto nanoscale topography," Nanoscale Research Letters, **7**, pp. 575–582.

[216] Svensson, S., Forsberg, M., Hulander, M., Vazirisani, F., Palmquist, A., Lausmaa, J., Thomsen, P., and Trobos, M., 2014, "Role of nanostructured gold surfaces on monocyte activation and *Staphylococcus epidermidis* biofilm formation.," International Journal of Nanomedicine, **9**, pp. 775–794.

[217] Najafinobar, N., 2011, "Effect of nanotopography on bacterial adhesion and EPS production," Master thesis, Chalmers University of Technology.

[218] Cabeen, M. T., and Jacobs-Wagner, C., 2005, "Bacterial cell shape," Nature Reviews Microbiology, **3**, pp. 601–610.

[219] Bardy, S. L., Ng, S. Y. M., and Jarrell, K. F., 2003, "Prokaryotic motility structures," Microbiology, **149**,

pp. 295–304.

[220] Wang, Q., Suzuki, A., Mariconda, S., Porwollik, S., and Harshey, R. M., 2005, "Sensing wetness: a new role for the bacterial flagellum," The EMBO Journal, **24**, pp. 2034–2042.

Appendix
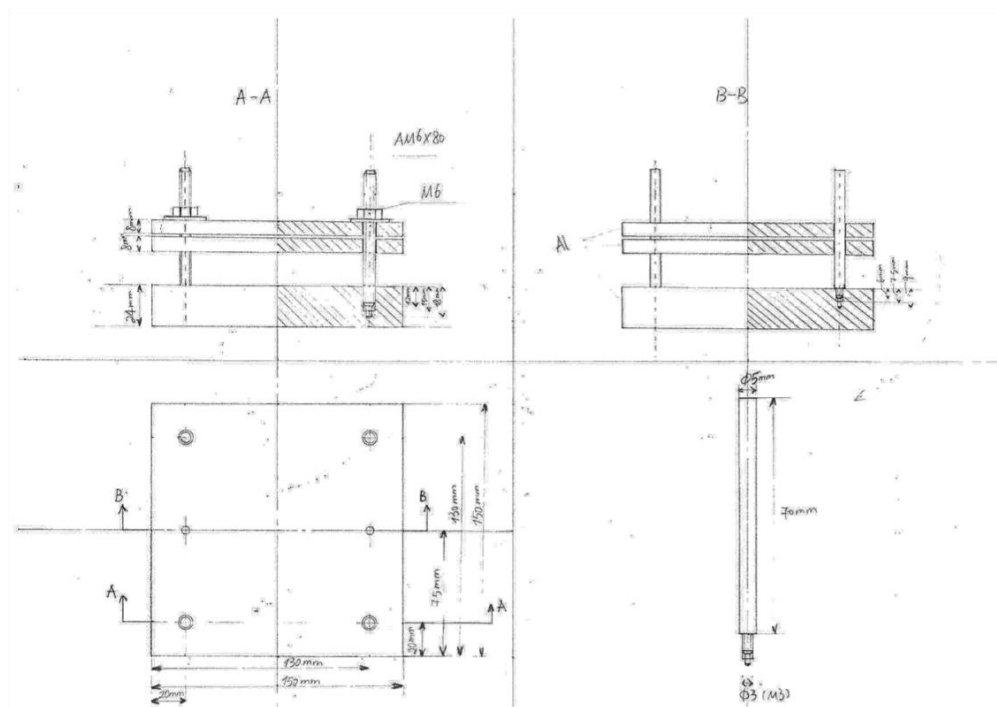
Figure 6-1: Sketch of the pressure molding set-up.
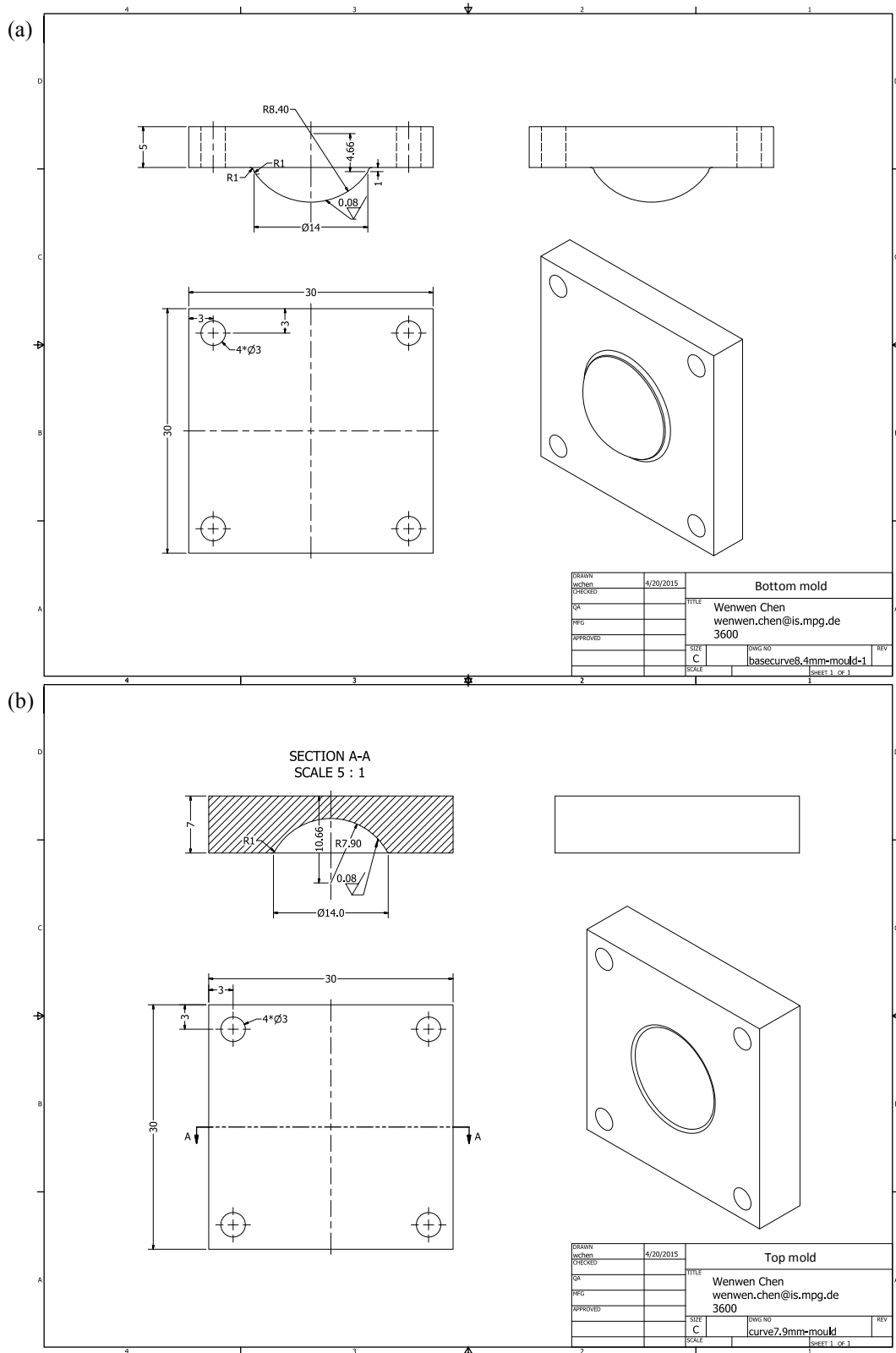
Figure 6-2: Sketch of the nanoimprinting molds with curved surfaces. The curvature designed is according to the contact angle lens with diopter of -3.75D. (a) The bottom mold has a curvature of 8.4 mm^{-1} and (b) the top mold has a curvature of 7.9 mm^{-1}.

Table 6-1: Summary of different substrates used for nanopillar preparation

Name	Thickness	Supplier	Application
Suprasil®2	0.17 mm	Heraeus	Transmittance measurement and AR property
Suprasil®2	0.5 mm/1 mm	Heraeus	Master stamp for nanoimprinting, bacterial attachment and growth study
Sapphire	1 mm	GWI Sapphire	Transmittance measurement and AR property
SF10 with GRIN layer	5 mm	Collaboration partner (Jena)	Transmittance measurement and AR property
Stainless steel	1 mm	Collaboration partner (Jena)	Self cleaning, electrowetting

Table 6-2: Nanoimprinting parameters used for preparing nanohole arrays on different polymers. The achieved structures are shown in Figure 6-3.

Polymer name	$T_{imprint}$ (°C)	T_{demold} (°C)	Potential applications
IPS®	165	80	Nanoimprinting
PMMA	130	70	Optics, implantable devices
ETFE	190	100	Bioinert
PMP	190	80	Bioinert
PET	190	80	Screen protection film
PP	130	65	Screen protection film
CX7323	190	80	Implantable devices
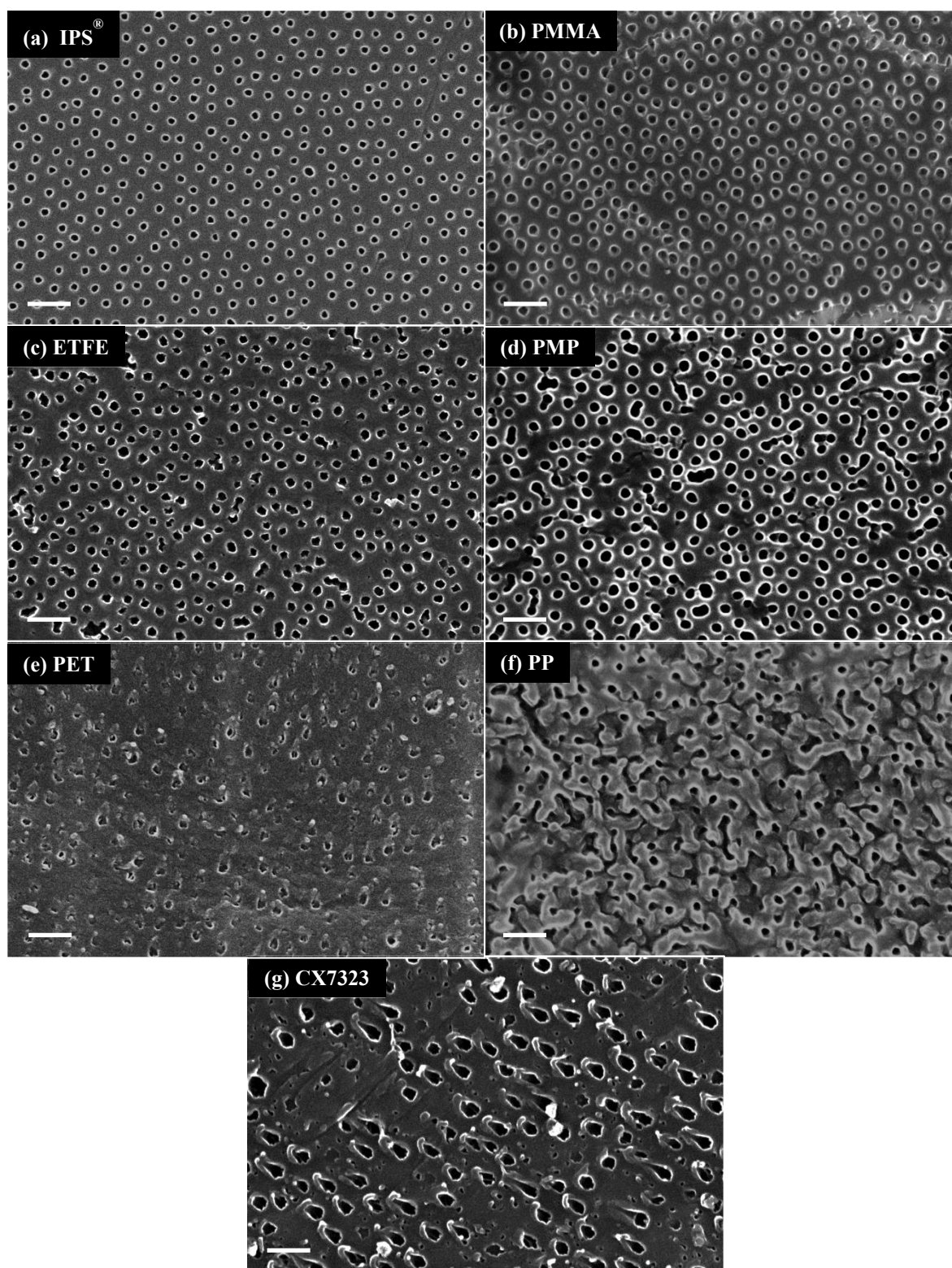
Figure 6-3: Nanoholes imprinted on different polymeric substrates. (a) IPS® substrate, mold: 100 nm in interspacing, 165 nm in height. (b) PMMA, mold: 100 nm interspacing, 165 nm in height. (c) ET-FE, mold: 100 nm interspacing, 165 nm in height. (d) PMP, mold: 100 nm interspacing, 165 nm in height. (e) PET, mold: 100 nm interspacing, 165 nm in height. (f) PP, mold: 100 nm interspacing, 165 nm in height. (g) CX7323, mold: 165 nm in interspacing, 300 nm in height. Scale bars: 200 nm.
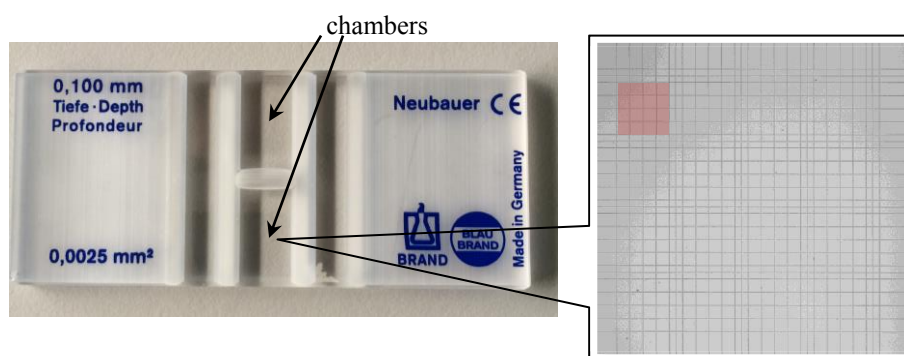
Figure 6-4: Hemocytometer.

Table 6-3: Polymers with varied block molecular lengths used for gold micelles preparation in this thesis.

Number of PS unit	Number of P2VP unit	Mn (PS) (g/mol)	Mn (P2VP) (g/mol)	Mw/Mn
1056	671	110000	70500	1.09
5358	713	55700	75000	1.07
501	323	52200	34000	1.05
154	33	16000	3500	1.05
240	143	25000	15000	1.05
1200	556	125000	58500	1.05
1824	523	190000	55000	1.1
1776	694	185000	73000	1.17
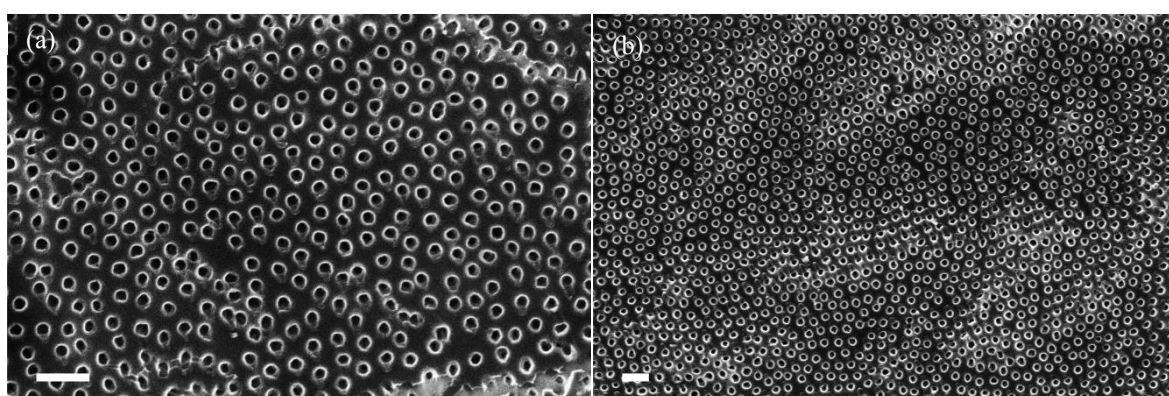
Figure 6-5: SEM images of PMMA sheet imprinted with nanohole structures. The mold was prepared with nanopillar structure (200 nm in height and 100 nm in inter-spacing). Scale bars: 200 nm.
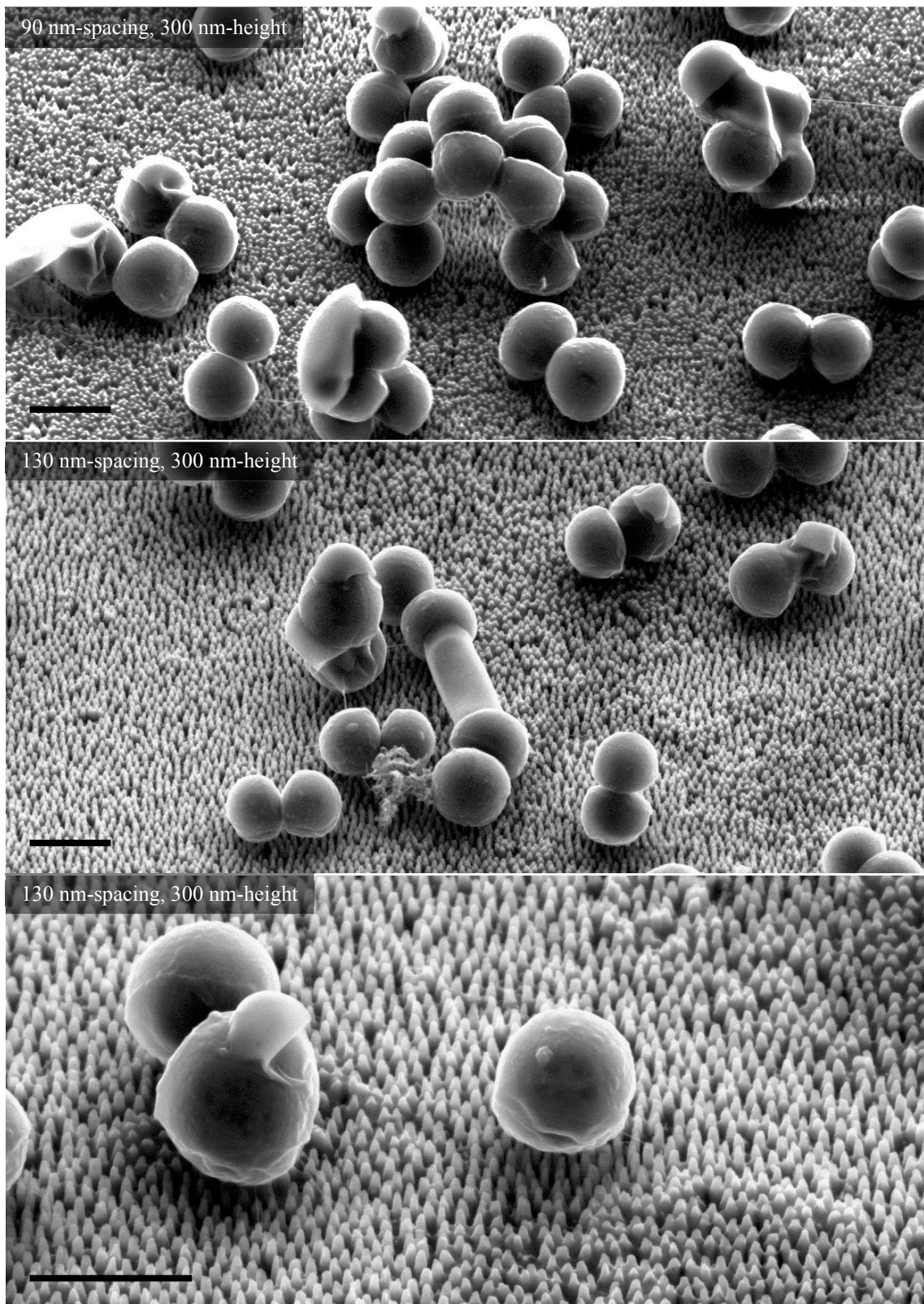
Figure 6-6: SEM images of *S. sciuri* sitting on nanopillar-structured surfaces. Aggregation of bacteria and nano-fibers most likely fimbriae connecting to the pillar top were observed. Scale bars: 1 μm.

List of Figures

133

List of Tables

Acknowledgements

The process of this dissertation is a very precious and memorable experience to me. It would not have been possible without the generous help and support from kind people around me. I would like to express my deepest gratitude to all of them:

First and foremost, I am heartily thankful to Prof. Joachim Spatz, who provided me this opportunity to develop my potential in scientific research with a good topic. He not only guided me to conduct scientific research in a right way, but also gave me the largest trust and support during the work.

My deep gratitude also goes to Prof. Dr. Reiner Dahint for being the referee to evaluate this work.

Very special thank goes to Priv.-Doz. Dr. Günter Majer for fruitful discussions, comments and suggestions.

Sincerely gratitude goes to Dr. Jan-Henning Dirks and Dr. Fania Geiger, for their patient discussions, scientific guidance and powerful support on my experiments and dissertation. They also encourage and help me a lot to build up my self-confidence in the expression of scientific ideas. Thanks for their tolerance and patience for me. Of course I would like to thank Dr. Christoph Morhard as he helped me in the beginning of my PhD.

I am deeply grateful to Dr. Zhaolu Diao for the fruitful discussions about my experimental results, explanations of the scientific principles and kind support for overcoming the difficulties.

Greatest thanks to Dr. Jennifer Young, for her continuous huge help in suggestions and corrections of scientific writing. This is extremely a cumbersome and time-consuming work, without her kind help, my dissertation could not proceed so smoothly.

Many thanks go to our "BioSurf" and "NanoAR" project partners: Dr. Christian Lingenfelder ("BioSurf"), Dr. Martin Udart ("BioSurf"), Mr. Friedrich Offenhäuser ("BioSurf"), Prof. Robert Brunner ("NanoAR"), Mr. Christian Williges ("NanoAR"), Mr. Matthias Kraus ("NanoAR") for the fruitful collaborations.

Sincere appreciation also goes to Dr. Gunther Richter and his group member Mr. Reinhart Völker for their high-quality SiO_2 layer deposition and the useful discussions about the thin film theory; Dr. Mitsuharu Konuma for the XPS measurements and data discussions; Mr.

Eidesstattliche Versicherung

gemäß § 8 der Promotionsordnung der Universität Heidelberg für die Naturwissenschaftlich-Mathematischen Gesamtfakultät

1. Bei der eingereichten Dissertation zu dem Thema „**Anti-Reflective and Anti-Bacterial Properties of Biomimetic Nanostructures**" handelt es sich um meine eigenständig erbrachte Leistung.

2. Ich habe nur die angegebenen Quellen und Hilfsmittel benutzt und mich keiner unzulässigen Hilfe Dritter bedient. Insbesondere habe ich wörtlich oder sinngemäß aus anderen Werken übernommene Inhalte als solche kenntlich gemacht.

3. Die Arbeit oder Teile davon habe ich bislang nicht an einer Hochschule des In- oder Auslands als Bestandteil einer Prüfungs- oder Qualifikationsleistung vorgelegt.

4. Die Richtigkeit der vorstehenden Erklärungen bestätige ich.

5. Die Bedeutung der eidesstattlichen Versicherung und die strafrechtlichen Folgen einer unrichtigen oder unvollständigen eidesstattlichen Versicherung sind mir bekannt.

Ich versichere an Eides statt, dass ich nach bestem Wissen die reine Wahrheit erklärt und nichts verschwiegen habe.

_____   _____
Ort und Datum   Unterschrift